Experimental Sensitivity Analysis and Control of Thermoacoustic Systems in the Linear Regime

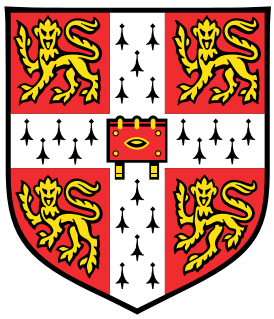

Nicholas Peter Jamieson

Department of Engineering

University of Cambridge

A dissertation submitted for the degree of

Doctor of Philosophy

Selwyn College

November 2017

Abstract

Experimental sensitivity analysis and control of thermoacoustic systems in the linear regime

By Nicholas Peter Jamieson

Thermoacoustic instability is one of the most significant problems faced in the design of some combustion systems. Thermoacoustic oscillations arise due to feedback between acoustic waves and unsteady heat release rate when the fluctuating heat release rate is sufficiently in phase with the unsteady pressure. The primary aim of designers is to design linearly stable thermoacoustic systems in which these dangerous oscillations do not arise. In thermoacoustics, adjoint-based sensitivity analysis has shown promise at predicting the parameters which have the most influence on the linear growth and decay rates as well as oscillation frequency observed during periods of linear growth and decay. Therefore, adjoint-based methods could prove to be a valuable tool for developing optimal passive control solutions. This thesis aims to develop novel experimental sensitivity analysis techniques and provide a first comparison with the predictions of adjoint-based sensitivity analysis.

In this thesis experimental sensitivity analysis is performed on (i) a vertical electrically-driven Rijke tube, and (ii) a vertical flame-driven Rijke tube. On the electrically-driven Rijke tube, the feedback sensitivity is studied by investigating the shift in linear growth and decay rates and oscillation frequency observed

during periods of linear growth and decay due to the introduction of a variety of passive control devices. On the flame-driven Rijke tube, the base-state sensitivity is studied by investigating how the linear growth and decay rates as well as oscillation frequency during periods of linear growth and decay change as the convective time delay of the flame is modified.

Adjoint-based sensitivity analysis gives the shift in linear growth and decay rate and the oscillation frequency when parameters are changed. This thesis provides experimental measurements of the same quantities, for comparison with the numerical sensitivity analysis, opening up new avenues for the development, implementation and validation of optimal passive control strategies for more complex thermoacoustic systems.

"You can't ever reach perfection, but you can believe in an asymptote toward which you are ceaselessly striving" - a sentiment that is unequivocally true for experimental research.

Paul Kalanithi, Neurosurgeon.

This thesis is dedicated to the memory of my mother, Anne-Maree Jamieson. Without her love of science and curiosity of the world around her, I would not be doing what I am doing.

Declaration

I hereby declare that except where specific reference is made to the work of others, the contents of this report are original and have not been submitted in whole or in part for consideration for any other degree or qualification in this, or any other university. This report is my own work and contains nothing which is the outcome of work done in collaboration with others, except as specified in the text and Acknowledgements. This report contains fewer than 65,000 words including appendices, bibliography, footnotes, tables and equations and has fewer than 150 figures.

Nicholas Peter Jamieson

November 2017

Acknowledgements

I would first and foremost like to extend my sincere gratitude to my supervisor, Professor Matthew Juniper. His expertise, encouragement, and patience has made this PhD one of the best experiences of my life. The opportunity to come to Cambridge and work in his group has been one of the best decisions I have ever made.

I would like to thank Dr Georgios Rigas for his assistance (and extreme patience) throughout my first year. Without his guidance and deep knowledge of experiments, fluid dynamics and everything in-between, I would most likely not be here. The sections of this thesis that were performed in collaboration with Dr Georgios Rigas are noted in each chapter overview. Thank you George.

I would like to extend a huge thank you to A/Prof Larry Li. Even though we were on other sides of the planet, Larry gave up so much of his time to make me feel at ease with the laboratory, the experimental set up and anything and everything to do with the undertaking of a PhD. Particularly in the latter stages, Larry has been a great friend and mentor.

The workshop technicians, Roy, John, Rob, Ken, Mark, Mick and Alistair have been nothing short of brilliant. I have been extremely fortunate to have the opportunity to work with such great people.

I would like to thank Dr Anurag Agarwal and Mr John Hazlewood from the acoustics laboratory for providing the pressure transducers used throughout the experiments in chapters 3 and 4. John Hazlewood was particularly helpful

by lending and assisting in the set up of the feedback control system used in chapters 6 and 7.

I would like to thank Ass. Prof. Patton Allison for helping me whenever I needed it. His expertise in combustion and experimental work made me a better experimentalist. Also, outside of the lab, his cooking and friendship kept me sane.

My time at Cambridge would not have been as great if it wasn't for the awesome people in the office. In no particular order: Lee, James, Luca, Alessandro, Guilio, Christophe, Pedro, Jose, Jack, Juan, Richard, Anh-Khoa, Francesca, Felix, Christian, Robert, Erwan, Steve, Aaron, Denis, Joce, Brian, Hans and Petr.

My time outside the lab would not have been the same if not for my college family. Particularly Will Gee, Paul Clarkson, Sam Cole, Beth Turk, George Severs and Katie Myerscough.

I would like to thank my Family, particularly my Father, Mother, Aunt Christine and Uncle Gordon, without whom none of this would be possible. I cannot explain the amount of gratitude I have for them.

Last but certainly not least I would like to thank my fiancé Becky, for always being there. She has kept me focused, kept me sane, and has been a stellar PhD psychiatrist. She knows more about the Rijke tube and thermoacoustics than she ever wanted to, and for that I apologise.

Preface

Peer-Reviewed Publications

1. Rigas, G., Jamieson, N. P., Li, L. K., Juniper, M. P. (2016). *Experimental sensitivity analysis and control of thermoacoustic systems.* Journal of Fluid Mechanics, 787, R1.

2. Jamieson, N. P., Rigas, G., Juniper, M. P. (2017). *Experimental sensitivity analysis via a secondary heat source in an oscillating thermoacoustic system.* International Journal of Spray and Combustion Dynamics. Special Edition. https://doi.org/10.1177/1756827717696325.

3. Jamieson, N.P., Juniper, M. P. (2017). *Experimental sensitivity analysis of a linearly stable thermoacoustic system via a pulsed forcing technique.* Experiments in Fluids. (58):123. https://doi.org/10.1007/s00348-017-2402-2.

4. Jamieson, N.P., Juniper, M. P. (2017). *Experimental sensitivity analysis and the equivalence of pulsed forcing and feedback control in thermoacoustic systems.* Proceedings of the ASME Turbo Expo 2017, Volume 4A: Combustion Fuels and Emissions. doi:10.1115/GT2017-63441.

Conference Papers

1. Jamieson, N. P., Rigas, G., Juniper, M. P. (2016). *Experimental sensitivity analysis as a validation for adjoint-based methods in the control of thermoacoustic oscillations.* Proceedings of the International Symposium on Thermoacoustic Instabilities in Gas Turbines and Rocket Engines: Industry meets Academia. 30 May - 3 June, 2016. Munich, Germany.

Conference Presentations

1. Jamieson, N. P. and Juniper, M. P. (2016). *Experimental sensitivity analysis of thermoacoustic systems via a pulsed forcing technique.* 1st UK Fluids Conference, Imperial College London. 7 - 9 September 2016, London, United Kingdom.

2. Jamieson, N. P. (2016) *Experimental sensitivity analysis and control of thermoacoustic systems.* 13th ERCOFTAC Osborne Reynolds Research Student Award, University of Manchester.

3. Jamieson, N. P., Rigas, G. Li, L. K. B., Juniper, M. P., *Experimental sensitivity analysis and control of thermoacoustic systems*, 68th Annual Meeting of the American Physical Society's Division of Fluid Dynamics (DFD), Boston, Massachusetts. November, 2015.

Table of contents

List of figures **xxi**

List of tables **xxxiii**

1 Introduction **1**

1.1 Thermoacoustic oscillations 2

1.1.1 Historical perspective 2

1.1.2 Basic theory 4

1.1.3 Driving mechanisms 5

1.2 Rijke tube 7

1.2.1 Basic theory 7

1.2.2 Literature survey 8

1.3 Control of thermoacoustic oscillations 13

1.3.1 Passive control 13

1.3.2 Active feedback control 15

1.4 Sensitivity analysis and adjoint-methods in thermoacoustics . . 16

1.4.1 Sensitivity analysis of thermoacoustic oscillations 16

1.4.2 Adjoint-based sensitivity analysis 17

1.4.2.1 Historical perspective 17

1.4.2.2 Application to thermoacoustic systems 18

1.5 Determination of experimental growth and decay rates 19

1.6 Thesis scope 21
1.7 Thesis structure 23

2 Details of the adjoint-based model 27
2.1 Introduction 28
2.2 The model 28
2.2.1 Governing equations and main assumptions 28
2.2.2 Adjoint-based equations and sensitivity analysis 31
2.3 Main results 34
2.3.1 Sensitivity to a passive drag device 34
2.3.2 Sensitivity to a secondary heat source 36
2.4 Concluding remarks 39

3 Sensitivity analysis and passive control via a drag device 41
3.1 Introduction 42
3.2 Experimental set-up 42
3.3 Baseline 44
3.3.1 Linear growth rates, linear decay rates and oscillation frequencies 45
3.4 Passive control via a drag device 49
3.4.1 Effect on critical power 50
3.4.2 Shift in linear growth rate 50
3.4.3 Shift in oscillation frequency 56
3.5 Concluding remarks 60

4 Sensitivity analysis and control via a secondary heat source 61
4.1 Introduction 62
4.2 Experimental set-up 62
4.3 Control via a secondary heat source 63

4.3.1 Methodology 63
4.3.2 Measurement of linear growth and decay rates 66
4.3.3 Measurement of frequency during linear growth and decay of oscillations 69
4.4 Sensitivity analysis 73
4.4.1 Shift in linear growth and decay rate 73
4.4.2 Shift in frequency during linear growth and decay of oscillations 79
4.5 Concluding remarks 84

5 Sensitivity analysis of a linearly stable thermoacoustic system via a pulsed forcing technique 85

5.1 Introduction 86
5.2 Experimental set-up and data processing 87
5.2.1 Apparatus 87
5.2.2 Data acquisition and processing 89
5.3 Control via a passive drag device 91
5.3.1 Methodology 91
5.3.2 Shift in linear decay rate and oscillation frequency 92
5.4 Control via a secondary heat source 99
5.4.1 Methodology 99
5.4.2 Shift in linear decay rate and oscillation frequency 102
5.5 Control via a variable cross-sectional area outlet 107
5.5.1 Methodology 107
5.5.2 Shift in linear decay rate and oscillation frequency 107
5.5.3 Effect of outlet diameter on flow and wall temperature . . 111
5.6 Concluding remarks 113

6 The determination of zero growth rates via pulsed forcing and feedback control in thermoacoustic systems 115

6.1 Introduction 116

6.2 Experimental set-up and data processing 117

6.2.1 Apparatus 117

6.2.2 Data acquisition and processing 119

6.3 Results 120

6.4 Concluding remarks 125

7 Sensitivity of a ducted premixed conical laminar flame to changes in convective time delay 127

7.1 Introduction 128

7.2 Main assumptions 129

7.3 Experimental set-up and data processing 132

7.3.1 Apparatus 132

7.3.2 Data acquisition and processing 133

7.4 Laminar flame speed changes due to fuel composition 138

7.4.1 Cantera calculations 138

7.4.2 Validation of laminar flame speed predictions 139

7.4.3 Results 141

7.5 Determining the convective time delay 144

7.5.1 Determining the flame length 145

7.5.2 Determining the convective time delay 147

7.5.3 Results 148

7.6 Sensitivity analysis 149

7.6.1 Sensitivity of linear growth and decay rates to changes in convective time delay 149

7.6.2 Sensitivity of frequencies during periods of linear decay to changes in convective time delay 152
7.6.3 Sensitivity of flame length to changes in fuel composition 154
7.7 Concluding remarks 155

8 Conclusions **157**
8.1 Summary of main findings 158
8.2 Future work 160

References **163**

Appendix A Images of primary heater and passive control devices **173**

Appendix B Uncertainty Analysis **175**
B.1 Uncertainties in $\delta\sigma$ measurement 176
B.2 Uncertainties in $\delta\sigma/\delta P_2$ measurement 176

Appendix C Operating Points for Chapter 7 **179**

List of figures

1.1 Feedback mechanism illustrating how thermoacoustic instability can lead to a combustion system becoming unstable 2

2.1 (a) Shift in linear growth rate due to the introduction of a passive drag device. (b) Shift in frequency during periods of linear growth dur to the introduction of a passive drag device. The model parameters used were $\tau = 0.01$, $\beta = 0.5$, $c_1 = 0.01$, and $c_2 = 0.004$. These figures were adapted from Magri and Juniper (2013c) . . 35

2.2 (a) Shift in linear growth rate due to the introduction of a secondary heat source. (b) Shift in frequency during periods of linear growth dur to the introduction of a secondary heat source. The model parameters used were $\tau = \tau_c = 0.01$, $\beta = 0.5$, $\beta_c = \beta/10$ $c_1 = 0.01$, and $c_2 = 0.004$. These figures were adapted from Magri and Juniper (2013c) 37

3.1 Experimental set-up. Where L is the length of the Rijke tube; x_c/L is the position of the passive drag device; and x_p/L is the position of the primary heater. 43

3.2 Bifurcation diagram obtained experimentally on the Rijke tube. The system becomes unstable through a subcritical Hopf bifurcation. The forward path (right-pointing triangles) shows the position of the Hopf point, and the backward path (left-pointing triangles) shows the position of the fold point. 44

3.3 Top: transient pressure signals obtained by applying step changes to the heater power input. (a) Growth, from $P_H - \epsilon$ to $P = 223$ W. (b) Decay, from $P_f + \epsilon$ to $P = 140$ W. Bottom: logarithm of the amplitude of the filtered pressure signals obtained by using the Hilbert transform. The linear growth (c) and linear decay (d) regions are represented by the red lines fitted between the noise floor and the point where nonlinear effects become important. . 45

3.4 Linear stability characteristics for baseline case as a function of the primary heater power: (a) Linear growth and decay rate, σ_r; (b) oscillation frequency, σ_i. Experimental data (symbols) and linear fit (red line). 48

3.5 Stability regions as a function of the passive drag device position. Forward path critical powers: Hopf points (squares); backward path critical powers: fold points (circles). A bistable region exists between the two lines. 49

3.6 (a) Linear growth rates and (b) linear decay rates, $\sigma_{r,c}$, obtained with the passive drag device positioned at $x_c/L = 0.4$. Each curve represents the amplitude response for a different step size above or below the Hopf or fold point. 52

3.7 (a) Linear growth rate and (b) shift in linear growth rate, experimentally obtained, as a function of power supplied to the heater and position of the passive drag device. Forward path critical powers (squares) and backward path critical powers (circles). The primary heater was located at $x_c/L = 0.25$. 53

3.8 Sensitivity of the linear growth rate to a passive drag device. (a) Experimental results and (b) theoretical predictions by Magri and Juniper (2013c) in arbitrary units. The legend for (a) shows the different primary heater powers which were examined. The units for all legend entries are Watts. The average sensitivity is also given as a visual aid to show the general qualitative behaviour. . 55

3.9 (a) Oscillation frequency and (b) shift in oscillation frequency, experimentally obtained, as a function of power supplied to the heater and position of the passive drag device. Forward path critical powers (squares) and backward path critical powers (circles). 58

3.10 (a) Sensitivity of the oscillation frequency to a passive drag device. The legend for (a) shows the different primary heater powers which were examined. The units for all legend entries, except for "Temp", are Watts. The average sensitivity is also given as a visual aid to show the general qualitative behaviour. An estimate of the oscillation frequency change due to variations in the outlet temperature shown in (b). 59

4.1 Schematic of experimental set-up. 63

4.2 Experimental operating range. "×" mark a point where a linear growth rate, linear decay rate and oscillation frequency measurement was acquired. Dashed lines at $x_c/L = 0.25$ indicate the location of the primary heater. The experiment was repeated five times at each data point. 64

4.3 (a) $x_c/L = 0.35$: Linear growth rates (blue) and linear decay rates (red) obtained for a range of secondary heat source powers. All baseline runs are shown in green; (b) $x_c/L = 0.35$: difference between growth rate with the secondary heat source and the baseline linear growth rate, $\delta\sigma_{r,g}$; (c) $x_c/L = 0.35$: difference between linear decay rate with the secondary heat source and the baseline decay rate, $\delta\sigma_{r,d}$. 67

4.4 (a) $x_c/L = 0.55$: Linear growth rates (blue) and linear decay rates (red) obtained for a range of secondary heat source powers. All baseline run is shown in green; (b) $x_c/L = 0.55$: difference between linear growth rate with the secondary heat source and the baseline linear growth rate, $\delta\sigma_{r,g}$; (c) $x_c/L = 0.55$: difference between linear decay rate with the secondary heat source and the baseline linear decay rate, $\delta\sigma_{r,d}$. 68

4.5 (a) $x_c/L = 0.35$: Frequency during period of growth (blue) and decay (red) of oscillations obtained for a range of secondary heat source powers. All baseline runs are shown in the green; (b) $x_c/L = 0.35$: oscillation frequency during period of linear growth with and without the secondary heat source, $\delta\sigma_{i,g}$; (c) $x_c/L = 0.35$: oscillation frequency during period of linear decay with and without the secondary heat source, $\delta\sigma_{i,d}$. 71

4.6 (a) $x_c/L = 0.55$: Frequency during period of growth (blue) and decay (red) of oscillations obtained for a range of secondary heat source powers. All baseline runs are shown in the green; (b) $x_c/L = 0.55$: oscillation frequency during period of linear growth with and without the secondary heat source, $\delta\sigma_{ri,g}$; (c) $x_c/L = 0.55$: oscillation frequency during period of linear decay with and without the secondary heat source, $\delta\sigma_{i,d}$. 72

4.7 Rayleigh index showing at which locations the heater encourages and discourages thermoacoustic oscillations. $A = 0.5$, $a = 1$, $K = 1$, $L = 1$ m, $c = 343$ m/s, $\bar{u} = 0.1$ m/s, and $\tau = 0.001$ s. 75

4.8 (a) Range of $\delta\sigma_{r,g}$ with the color patch outlining the uncertainty; (b) Range of $\delta\sigma_{r,d}$ with the color patch outlining the uncertainty. . 77

4.9 (a) The shift in linear growth rate (blue) and linear decay rate (red) due to a secondary heat source; (b) The adjoint-based predicted shift in linear growth rate due to a secondary heat source (Magri and Juniper, 2013c). 78

4.10 (a) Range of $\delta\sigma_{i,g}$ with the color patch outlining the uncertainty; (b) Range of $\delta\sigma_{i,d}$ with the color patch outlining the uncertainty. . 81

4.11 (a) The shift in oscillation frequency during linear growth (blue) and linear decay (red) due to a secondary heat source; (b) The adjoint-based predicted shift in oscillation frequency during periods of linear growth due to a secondary heat source (Magri and Juniper, 2013c). 82

5.1 Experimental set-up. Experiment 1: passive drag device and two open ends; Experiment 2: secondary heat source and two open ends; Experiment 3: variable area at the outlet of the tube. 87

5.2 (a) Raw pressure signal of single data point. (b) Filtered analytical signal obtained using the Hilbert transform. Red dashed line denotes the region of linear decay from which data was extracted. 90

5.3 Mean wall temperature, measured at position x/L, with the passive device placed at position x_c/L. 91

5.4 (a) Baseline linear decay rate ($\sigma_{r,0}$), and controlled linear decay rate ($\sigma_{r,c}$) for a range of passive drag device locations (x_c/L). (b) The shift in linear decay rate ($\delta\sigma_r = \sigma_{r,c} - \sigma_{r,0}$) due to the passive drag device. Note: the legend is identical for (a) and (b) and represents x_c/L and all error bars are presented for a 95 % confidence interval. The legend is identical for (a) and (b). . . . 94

5.5 (a) The shift in linear decay rate as a function of x_c/L. (b) Theoretical predictions of Magri and Juniper (2013c). Note: the legend is identical for (a) and (b) and represents x_c/L and all error bars are presented for a 95 % confidence interval. The legend is identical for (a) and (b). 95

5.6 Comparison between the shift in linear growth rate measured (i) via the pulsed forcing technique with $P = 170$ W and (ii) by stepping the primary heater power from $P_{Hopf} + \epsilon$ to 170 W (results from chapter 3). 96

5.7 (a) Baseline oscillation frequency during periods of linear decay ($\sigma_{i,0}$), and oscillation frequency during periods of linear decay with passive drag device installed ($\sigma_{i,c}$) for a range passive drag device locations (x_c/L). (b) The shift in oscillation frequency during periods of linear decay ($\delta\sigma_i = \sigma_{i,c} - \sigma_{i,0}$) due to the passive drag device. 97

5.8 (a) The shift in oscillation frequency during periods of linear decay as a function of x_c/L. (b) Theoretical predictions of Magri and Juniper (2013c) suggest that the model is deficient, not the adjoint. Note: the legend is identical for (a) and (b) and represents x_c/L and all error bars are presented for a 95 % confidence interval. . 98

5.9 (a) Linear decay rates measured with no control device ($\sigma_{r,0}$) and for a range of secondary heat source powers ($\sigma_{r,c}$) at $x_c/L = 0.70$. (b) Difference between the baseline linear decay rates and those measured for a range of secondary heater powers ($\delta\sigma_{r,c}$) at $x_c/L = 0.70$. (c) Averaged difference between the baseline linear decay rate ($\sigma_{r,0}$) and the linear decay rate obtained with a secondary heat source ($\sigma_{r,c}$) for a range of x_c/L. All error bars are presented with a 95 % confidence interval. The legend for (c) is the same as shown in figure 5.10c. 100

5.10 (a) Oscillation frequency during periods of linear decay measured with no control device ($\sigma_{i,0}$) and for a range of secondary heat source powers ($\sigma_{i,c}$) at $x_c/L = 0.70$. (b) Difference between the baseline oscillation frequency during periods of linear decay and those measured for a range of secondary heater powers ($\delta\sigma_{i,c}$) at $x_c/L = 0.70$. (c) Averaged difference between the baseline oscillation frequency during periods of linear decay ($\sigma_{i,0}$) and the oscillation frequency during periods of linear decay obtained with a secondary heat source ($\sigma_{ir,c}$) for a range of x_c/L. All error bars are presented with a 95 % confidence interval. 101

5.11 (a) Shift in linear decay rate as a function of x_c/L. (b) Theoretical predictions of Magri and Juniper (2013c). All error bars are presented for a 95 % confidence interval. 104

5.12 (a) Shift in oscillation frequency during periods of linear decay as a function of x_c/L. (b) Theoretical predictions of Magri and Juniper (2013c). All error bars are presented for a 95 % confidence interval. 105

5.13 (a) Linear decay rates measured with no control ($\sigma_{r,0}$), and with control ($\sigma_{r,c}$) for a range of D_{iris}. (b) The difference between the linear decay rates measured with no control ($\sigma_{r,0}$) and with control ($\sigma_{r,c}$). (c) The shift in linear decay rate as a function of D_{iris}/D_{tube}. The legend is identical for (a) and (b). 108

5.14 (a) Oscillation frequency during periods of linear decay measured with no control ($\sigma_{i,0}$), and with control ($\sigma_{i,c}$) for a range of D_{iris}. (b) The difference between the oscillation frequency during periods of linear decay measured with no control ($\sigma_{i,0}$) and with control ($\sigma_{i,c}$). (c) The shift in oscillation frequency during periods of linear decay as a function of D_{iris}/D_{tube}. The legend is identical for (a) and (b). 109

5.15 (a) Mean outlet temperature measured at the centreline as a function of D_{iris}/D_{tube}. (b) Mean inlet temperature measured at the centreline as a function of D_{iris}/D_{tube}. (c) Mean wall temperature measured on outside of tube as a function of D_{iris}/D_{tube}. Note that all data points in (a), (b) and (c) are averaged over 150 experimental tests. 112

6.1 Experimental apparatus. CD: Control Device. 117

6.2 (a) Raw pressure signal of a single data point obtained via the pulsed forcing technique. (b) Filtered analytical signal obtained using the Hilbert transform of the raw pressure signal shown in (a). (c) Raw pressure signal of a single data point obtained as the feedback controller is switched off. (d) Filtered analytical signal obtained using the Hilbert transform of the raw pressure signal shown in (c). 118

6.3 Operating region for results presented in §6.3. $P_{1,Hopf}$ indicates the stability curve for a variety of iris diameters. FBC denotes points where data is taken via feedback control. PFT denotes points where data is taken via the pulsed forcing technique. Spacing between each red circle and each blue cross is 20 W. 121

6.4 Linear growth rates measured via feedback control and linear decay rates measured via pulsed forcing for a range of iris diameters. 123

6.5 Averaged linear growth and decay rates for a range of D_i/D_t. A linear fit is applied to each set of linear growth and decay rate data. 124

7.1 Mean heat release rate as the equivalence ratio is changed for a 50 % methane/ 50 % ethylene mixture. All parameters used to generate this result were the same as discussed in §7.4 of this chapter. 130

7.2 Experimental set-up. 132

7.3 (a) Raw pressure during one linear decay rate measurement after a pulse at t = 1 s. (b) Filtered analytical Hilbert transformed signal during one decay rate measurement, showing linear decay over approximately 1 s. The linear decay rate is measured between the dashed lines, over approximately 0.5 s, which is 150 cycles. . . . 136

7.4 (a) Raw pressure during one linear growth rate measurement after the feedback controller is turned off at approximately t = 1 s. (b) Filtered analytical Hilbert transformed signal during one linear growth rate measurement, showing linear growth over approximately 1 s. The growth rate is measured between the dashed lines, over approximately 0.5 s, which is 150 cycles. 137

7.5 (a) S_l as a function of equivalence ratio for a pure methane-air flame. Cantera calculation validated against Vagelopoulos et al. (1994) and Vagelopoulos and Egolfopoulos (1998). (b) S_l as a function of equivalence ratio for a pure ethylene-air flame. Cantera calculation validated against Egolfopoulos et al. (1990), Hassan et al. (1998) and Jomaas et al. (2005). 140

7.6 Range of S_l achievable with methane, ethylene and air mixtures. . 141

7.7 L_f variations with operating point. A comparison is made with the results from the Cantera calculations. I = data obtained when the system was self-linearly stable; II = data obtained when the system was linearly stable in the presence of a feedback controller. 143

7.8 (a) Unprocessed flame image (natural emission integrated over line of sight). (b) Filtered image of the flame (a threshold value, F_{th}, where $F_{th} > x$ was set to zero. x was modified on a trial and error basis determined by the flame geometry). (c) Horizontal axis shows the summation of non-zero pixels to determine L_f. Note: 1 pixel $\approx$ 0.1538 mm. 145

7.9 Schematic of flame-burner configuration for the calculation of τ_c. L_f is the unperturbed flame length, $u_p(r)$ is the Poiseuille velocity profile as a function of the burner radius, r, and d is the burner diameter. 147

7.10 (a) τ_c as a function of L_f. I = data obtained when the system was self-linearly stable; II = data obtained when the system was linearly stable in the presence of a feedback controller. 148

7.11 (a) Linear growth and decay rates obtained for different operating points. (b) Linear growth and decay rate as a function of τ_c. . . . 151

7.12 The stability regions of an open-ended Rijke tube as a function of τ_c (McManus et al., 1993). 152

7.13 (a) Oscillation frequency observed during periods of linear growth and decay obtained for different operating points. (b) Oscillation frequency observed during periods of linear growth and decay as a function of τ_c. 153

7.14 L_f as a function of the percentage of ethylene in the fuel mixture. Cantera results are compared with experimental results to validate the S_l calculation code. 155

A.1 (a) Primary heater. (b) Passive drag device and secondary heat source. (c) Top disk of (a) and (b). (d) Diagram of the variable cross-sectional area outlet (mechanical iris). 174

List of tables

7.1 Phantom MIRO M310 settings 134

C.1 Operating points used in Chapter 7 180

Chapter 1

Introduction

This chapter provides a theoretical foundation and context for the work presented in this thesis. Thermoacoustic instability is discussed from a historical perspective, with its basic theory, driving mechanisms, and methods for its passive and active feedback control reviewed. The experimental campaigns conducted in this thesis have been performed on electrical and flame-driven Rijke tubes. Thus it is logical to give an overview of the physical underpinnings of the vertical Rijke tube as well as a concise overview of the state-of-the-art. This thesis focuses on experimental sensitivity analysis of linear growth rates, linear decay rates and oscillation frequency during periods of growth and decay. A background of theoretical sensitivity analysis is provided followed by a discussion of adjoint-based sensitivity analysis as applied to thermoacoustic systems. Experimental methods for obtaining growth and decay rates are discussed before ending the chapter with a summary the thesis' scope and structure.

1.1 Thermoacoustic oscillations

1.1.1 Historical perspective

In many combustion systems, there exist high-amplitude pressure oscillations whose frequency ranges are close to those of the natural acoustic modes of the combustion system (Lieuwen and Lu, 2005). These oscillations arise due to feedback between acoustic waves and unsteady heat release rate when the fluctuating heat release rate is sufficiently in phase with the unsteady pressure (figure 1.1). This phenomenon is known as thermoacoustic instability. It gives rise to high-amplitude pressure and velocity oscillations that threaten the operability and reliability of combustion systems by increasing the risks of thrust oscillations, mechanical vibration, excessive thermal and mechanical loading, resulting in decreased efficiency and ultimately system failure (Lieuwen and Lu, 2005).

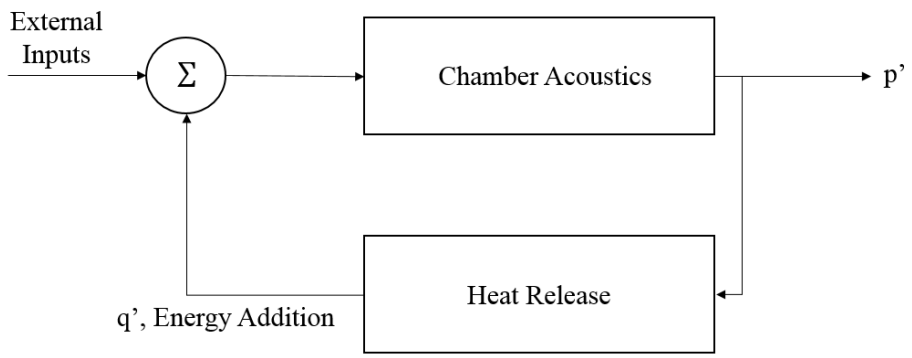

Fig. 1.1 Feedback illustrating how thermoacoustic instability can lead to a combustion system becoming unstable (Matveev, 2003).

The origins of thermoacoustic instability can be traced back to the early 19th century. It was observed by Higgins (1802) that sound was generated when hydrogen gas was heated as it flowed through a tube. Although this was the first recorded instance of thermoacoustic instability to the authors' knowledge, it was not until the early 20th century that industrial problems associated with

thermoacoustic oscillations began to arise (Lieuwen and Lu, 2005; Margolin, 1999). Thermoacoustic oscillations were noticed first in rocket engines (Crocco and Cheng, 1956; Culick, 1988; Harrje and Reardon, 1972), then aero-engine afterburners (Langhorne, 1988; Macquisten and Dowling, 1995), gas turbines and industrial furnaces (Correa, 1998). As an example of the extent to which thermoacoustic oscillations affect combustion systems, one can look at the F-1 engine[1]. During the development of these engines, it was found that pressure oscillations of approximately 100 % of the mean combustor pressure occurred at a frequency between 200-500 Hz. As well as the structural damage that these oscillations caused, they also incurred additional costs and time-delays in the development of the engine. Approximately 2000 full-scale tests had to be performed in order to suppress these oscillations (Oefelein and Yang, 1993).

More recently, the suppression of thermoacoustic oscillations has become an increasingly important consideration for the gas turbine industry. With environmental factors an ever present concern in engineering practice, stricter legislation regarding the emission of NO_x has been implemented (Lieuwen and Zinn, 1998). To meet the emission targets, there has been a shift towards gas turbines that operate under a lean and premixed regime. The heat release rate of lean premixed flames is more sensitive to acoustic perturbations. This is because they are very sensitive to equivalence ratio perturbations. Also, the flame attachment (and therefore heat release rate) become sensitive to perturbations. (Lieuwen et al., 2001).

[1]The engine on-board the Saturn Rocket as apart of NASA's Apollo Program.

1.1.2 Basic theory

The root cause of thermoacoustic instability is the interaction between the acoustics of a system and the unsteady heat release rate within that system. Rayleigh (1878) provided the first scientific explanation for how energy can be transferred by a heating element to the acoustic field. This explanation led to perhaps the most widely quoted statement in the field of thermoacoustics, the Rayleigh Criterion (Rayleigh, 1878):

> "If heat be periodically communicated to, and abstracted from a mass of air vibrating (for example) in a cylinder bounded by a piston, the effect produced will depend upon the phase of the vibration at which the transfer of heat takes place. If heat be given to the air at the moment of greatest condensation, or taken from it at the moment of greatest rarefaction, the vibration is encouraged. On the other hand, if heat be given at the moment of greatest rarefaction, or abstracted at the moment of greatest condensation, the vibration is discouraged."

The qualitative Rayleigh Criterion was expressed mathematically by Putnam and Dennis (1954) as:

$$\int_{\tau}\int_{V} q'(x,t)p'(x,t)\mathrm{d}x\mathrm{d}t > 0 \tag{1.1}$$

where $q'(x,t)$ is the fluctuating heat release rate, $p'(x,t)$ is the fluctuating pressure field, x and t are spatial and temporal variables respectively. Equation (1.1) is known as the Rayleigh integral and is evaluated over a time-period τ and a control volume V. The phase difference between the unsteady heat release rate, q, and the acoustic pressure, p, is labelled θ. If $|\theta| < 90°$ then the Rayleigh integral is positive and oscillations' energy grows. Conversely, if $90 < |\theta| < 270$ then the Rayleigh integral is negative and oscillations' energy decreases. Chu (1965)

updated equation (1.1) to include viscous dissipation and acoustic radiation, both of which extract energy from the acoustic oscillations. Further information can be found in the books by Crocco and Cheng (1956), Culick (1988), Lieuwen and Lu (2005), and Culick (2006).

1.1.3 Driving mechanisms

There are many physical mechanisms that can contribute to thermoacoustic oscillations. This section will cover the main driving mechanisms as discussed by Candel (1992, 2002) and Lieuwen and Lu (2005). The discussion will focus on the main physical mechanisms that cause a fluctuation in heat release rate in a thermoacoustic system. A discussion of the decomposition and propagation of fluctuations that can lead to oscillations can be found in Lieuwen's "Unsteady Combustor Physics" (Lieuwen, 2012).

1. **Vortex Interaction**.

   It is well known that flame-vortex interaction can instigate an unsteady heat release rate fluctuation (Candel, 1992, 2002; Lieuwen and Lu, 2005; Renard et al., 2000). Candel (1992, 2002) suggests that vortex interaction within a combustion system is one of the most prominent physical mechanisms driving thermoacoustic oscillations. When these vortical structures interact with the flame (or heat source) in a combustion system, a self-sustaining feedback mechanism that adds energy to the acoustic mode oscillations is created through delayed combustion of the vortex structure (Candel, 2002). According to Candel (1992), these vortical structures are usually caused by natural flow oscillations or external perturbations, such as pressure waves or structural vibrations.

2. **Equivalence-Ratio Oscillations**

   Equivalence-ratio oscillations as a physical mechanism driving thermoacous-

tic oscillations have been discussed by Lieuwen and Lu (2005) and Lieuwen and Zinn (1998). An oscillation in a reactive mixture's equivalence-ratio is usually attributed to a propagating pressure oscillation that causes fluctuations in reactant mixing processes and supply rates of fuel and/or oxidisers (Lieuwen and Lu, 2005).

3. **Oscillatory Atomization and Vaporisation**

   Oscillatory atomization and vaporisation as a driving mechanism for thermoacoustic oscillations have been discussed by (Kendrick et al., 1999; Lefebvre, 1980; Lieuwen and Lu, 2005). Atomization is a process in which a volume of liquid is decomposed into a multitude of small droplets. The aim of atomization is to improve the efficiency of combustion. This is achieved by increasing the ratio of surface area to the volume of the liquid, causing higher rates of evaporation, meaning that the combustion process can burn more of the liquid fuel (Lefebvre, 1980). In terms of driving thermoacoustic oscillations, interactions between the atomized fluid and the acoustic field can result in oscillatory variations in droplet geometry and evaporation rates. It is these variations that lead to oscillations in the equivalence-ratio (as discussed above), ultimately leading to fluctuations in heat release rate (Lieuwen and Lu, 2005).

Other physical mechanisms that drive thermoacoustic oscillations are discussed by Candel (1992, 2002) and include pulsations of the flame front or reacting jets, periodic extinctions and ignitions, flame acceleration and parametric instabilities, and flame interactions with the solid boundaries of the combustion system.

1.2 Rijke tube

The Rijke tube, first studied by Rijke (1859), is a simple configuration for the study of thermoacoustic instabilities (Raun et al., 1993). Typically, a Rijke tube configuration consists of a long tube with an electric heater or flame located in the first half. In this thesis, both the electrical and flame-driven Rijke tubes are orientated vertically.

1.2.1 Basic theory

To explain the physical mechanism it is convenient to neglect the mean heat release rate from the heater/flame and assume that the pressure fluctuation at the open ends of the tube is zero. Therefore, the fundamental acoustic mode has a pressure node at either end of the tube and an antinode at the midpoint. The acoustic velocity has a node at the centre and an antinode at either end. During the compression phase of the acoustic cycle, the acoustic velocity is directed towards the centre of the tube, causing the pressure in the tube to increase. When the heater is placed in the upstream half of the tube, the acoustic velocity and the mean velocity are in the same direction during the compression phase. This causes the air speed around the heater, and therefore the heat transfer, to be larger than average during the compression phase. Conversely, the heat transfer is lower than average during the expansion phase. Critically, there is also a time delay (Lighthill, 1954) between the velocity at the heater and the subsequent heat release rate. These two properties mean that, over an acoustic cycle, more heat release occurs during moments of higher pressure than occurs during moments of lower pressure, causing more mechanical work to be done by the gas expanding during the expansion phase than is needed to compress it during the compression phase (Rayleigh, 1878). This results in the amplitude of acoustic oscillations growing until the heat release rate perturbations saturate

and the excess work is balanced through acoustic radiation, viscous losses and thermal losses.

1.2.2 Literature survey

The Rijke tube has been the subject of rigorous theoretical and experimental studies since its inception in 1859 (Rijke, 1859). To date there have been two comprehensive review papers published on the Rijke tube (Feldman, 1968; Raun et al., 1993).

One of the first theoretical investigations was performed by Neuringer and Hudson (1952). They found that i) the heat transfer is largely dependent on the negative of the velocity gradient of the flow through the heater, and ii) that turbulence plays an important role in the excitation of the tones associated with the Rijke phenomenon.

Although the criterion for thermoacoustic oscillations was qualitatively established by Rayleigh (1878), it was not until 1954 that Putnam and Dennis (1954) mathematically framed Rayleigh's theory. In their paper, Putnam and Dennis (1954) propose a theory that suggests that the audible tones are due to a phase-lag between changes in flow rate and heat-transfer rate. Their theoretical predictions are well supported by corresponding experimental results.

The study that laid the ground work for the stability characteristics of the Rijke tube was conducted by Carrier (1954). Carrier (1954) was the first to perform linear stability analysis on a model of the Rijke tube, obtaining its eigenvalues. These give the growth rates and frequencies of the system.

Merk (1957) derived a model using transfer functions that successfully accounts for the main features of the physical phenomena seen in the Rijke tube: that the first mode of thermoacoustic oscillation was only excited when the heater was placed in the first half of the tube. Merk (1957) also went on to state that

the maximum excitation of the fundamental mode occurs if the gauze heater is placed at approximately 1/5 the total length, measured from the inlet. This value of 1/5 was later revised by Saito (1965). Furthermore, Merk (1957) showed that there should be two positions of the gauze heater, x/L = 0.1 and 0.48, that could give rise to the excitation of the first overtone Merk (1957). Merk (1957) found that since the values of the reduced circular frequency are smaller for the first overtone compared to the resonant tone, a higher air velocity is required for excitation.

Maling (1963) synthesised the work of Putnam and Dennis (1954), and derived a mathematical relationship that provided the first comprehensive study of the stability boundaries of the Rijke tube.

Saito (1965) further developed the theory of stability regions of the Rijke tube. Saito (1965) performed experiments that aimed to understand the relationship between the position of the primary heater and the onset of oscillations. This was a landmark experiment as it provided the most accurate profile of where the primary heater would excite thermoacoustic oscillations and where it would suppress them. Saito (1965) found that the optimal location of the primary heater for excitation was at 1/4 of the length of the Rijke tube, measured from its inlet. Saito (1965) also showed that thermoacoustic oscillations have a region of linear growth.

The study of stability regions was further developed through experiments by Collyer and Ayres (1972), Katto and Sajiki (1977) and Madrame (1983). In conjunction with these studies, theoretical work was conducted by Bayly (1985) and Kwon and Lee (1985).

Of particular interest are the experimental results of Katto and Sajiki (1977). They built on the work of Saito (1965), and experimentally showed how the onset of oscillations was affected by heat insulation and wall cooling, for the tube orientation (horizontal or vertical), the primary heater location, the tube length,

and the geometry of the primary heater. The paper provided comprehensive results on initial exploratory experiments on the Rijke tube.

Nicoli and Pelcé (1989) developed a simple one-dimensional model which calculated the longitudinal heat conduction and the unsteady heat transfer from a heater to a compressible gas. From this calculation, a transfer function for the heater was obtained allowing a better understanding of the stability limits of the Rijke tube.

Bayly (1985) conducted the first study on the nonlinear aspects of the Rijke tube. He investigated the nonlinear relationship between acoustic motion and the heat transfer to a gauze heating element. The model presented by Bayly (1985), gave a prediction for which mean flow velocities were conducive to oscillations. It was also noted that under certain circumstances, hysteresis[2] was possible.

Detailed analyses on the heat transfer throughout the Rijke tube have been rare. Raun and Beckstead (1993) and McIntosh and Rylands (1996) studied varying temperature gradients arising from thermoacoustic oscillations. Raun and Beckstead (1993), developed a model for the Rijke tube system, which was able to predict the growth rates and frequencies whilst also accounting for the underlying effects of heat loss and entrained particles on the acoustic field oscillations. The model identified that distributed heat loss had an effect on the growth rate of the oscillations. Raun and Beckstead (1993) found that an accurate prediction of the acoustic mode shape required an accurate consideration of distributed heat losses. This is important as if even the most subtle changes in the acoustic mode shape occur, the acoustic velocity and frequency of the flame significantly varies, causing an inaccurate prediction of the acoustic growth rate. The work

[2]Hysteresis refers to the lack of reversibility as a parameter of a nonlinear system is varied Strogatz (1994). For example, imagine x is a control parameter for a dynamical system. If x is increased from an initial state ($x = 0$) past a critical point ($x = x_{crit}$) the system will bifurcate to a larger-amplitude branch solution. If x is further increased, the solution continues to move along the large amplitude branch. Now, if x is reduced, the solution will still remain on the large-amplitude branch, even when $x = 0$.

conducted by McIntosh and Rylands (1996) employs the same approach as that of Raun and Beckstead (1993). The assumption made by McIntosh and Rylands (1996) is that in calculating the heat loss term, the majority of the heat losses occur due to a combination of forced convection inside the tube and natural convection outside the tube.

In the experimental studies on the Rijke tube, temperature measurements have rarely been obtained. The exception is in a study by Mcquay et al. (2000) where experiments were performed to assess how temperature profiles within the Rijke tube were affected by variations in the acoustic mode. It was observed that the flame height and structure varied significantly with the onset of oscillations, as expected.

Whilst these studies outlined heat transfer considerations for implementation in Rijke tube models, it was Matveev (2003) who produced the most comprehensive heat transfer model to date in his PhD thesis at the California Institute of Technology. In the model presented by Matveev (2003), four types of heat transfer were considered:

1. Forced convection between; i) the heating element and the air flow inside the tube, ii) the supporting structure attached to the heating element and the air flow inside the tube, iii) and the Rijke tube walls and the air flow inside the tube.

2. Natural convection between; i) the ambient air and the Rijke tube, ii) the ambient air and the supporting structure attached to the heating element outside the Rijke tube, iii) and the air flow and the supporting structure attached to the heating element inside the tube.

3. Heat conduction; i) in the walls of the Rijke tube, ii) between the heating element and the Rijke tube walls through the insulating structure, and iii) along the supporting structure of the heating element.

4. Thermal radiation; i) outside the Rijke tube between the Rijke tube walls and the environment, and ii) inside the Rijke tube between the heating element and the Rijke tube walls and environment.

The heat transfer model proposed by Matveev (2003) agrees well with experimental results. Prior to the onset of thermoacoustic oscillations the model calculations agreed with experimental results with approximately 2% error, whilst in the excited region the model agrees with experimental results with approximately 3% error.

Further mathematical modelling of the Rijke tube system was developed in papers by Dowling (1995) and Yoon et al. (1998).

The main research interests regarding the Rijke tube for the last two decades have been concerned with the control of thermoacoustic oscillations and the modelling of non-linearities in thermoacoustic systems. The control of thermoacoustic oscillations is discussed further in §1.3.

The most relevant nonlinear work relating to this thesis was conducted by Matveev (2003), Subramanian et al. (2010) and Subramanian et al. (2013). They studied the bifurcation characteristics of the Rijke tube. The Rijke tube exhibits the dynamical systems behaviour of a subcritical Hopf bifurcation. Matveev (2003) performed experimental studies on the bifurcation characteristics of a horizontal electrically-driven Rijke tube. Matveev (2003) showed that by incrementally increasing the power to the heat source, the system underwent a subcritical Hopf bifurcation. Numerical studies were performed by Subramanian et al. (2010) and Subramanian et al. (2013). They used the method of numerical continuation to obtain the bifurcation diagrams. The amplitudes of the resulting limit-cycles were able to be determined by the model, leading to the linear and nonlinear stability regions being obtained for variations in non-dimensional heater power, heater location, and damping coefficient. Furthermore, the exact

parameter values were able to be obtained for the onset time of the Hopf bifurcation.

As this thesis focused on thermoacoustic oscillations in the linear regime, nonlinear studies on thermoacoustic systems are not covered in depth here but further reading can be found in Hantschk and Vortmeyer (1999), Yoon et al. (2001), Bittanti et al. (2002), Matveev and Culick (2003), Balasubramanian and Sujith (2008), Juniper and Waugh (2010), Juniper (2011b), Juniper (2011a), Mariappan and Sujith (2011), Noble et al. (2012), Zhao (2012), Gopalakrishnan and Sujith (2014), Sayadi et al. (2014), Weng et al. (2014), Basok and Gotsulenko (2014), Li et al. (2014).

1.3 Control of thermoacoustic oscillations

Due to the dangers associated with thermoacoustic oscillations, their control remains an active area of research. Control measures must be employed to de-couple the acoustic waves and the unsteady heat release rate (Dowling and Morgans, 2005). The control methods used in the suppression of thermoacoustic oscillations can be divided up into two categories; passive control and active feedback control.

1.3.1 Passive control

Passive control of thermoacoustic oscillations can be achieved in two main ways (Culick, 1988; Dowling and Morgans, 2005): (i) hardware design modifications; and (ii) reducing the energy of the oscillation through the implementation of damping devices.

Steele et al. (2000) demonstrated that by varying the axial location of the fuel spokes inside a lean-premixed fuel injector, thermoacoustic oscillations were suppressed by the resulting reduction in excitation of the acoustic field within the

tested combustion system. Richards and Janus (1997) and Richards et al. (2003) have also demonstrated how passive control can be achieved through design changes in the combustor geometry. Helmholtz resonators have also been used with success (Bellucci et al., 2004; Gysling et al., 2000). Bellucci et al. (2004) and Gysling et al. (2000) have suggested that the use of Helmholtz resonators as a method of damping low-frequency oscillations in a combustion system is an effective way to improve the operability range of a combustor. Further examples of how the energy associated with thermoacoustic oscillations can be reduced via the implementation of perforated liners are given by Eldredge and Dowling (2003) and Noiray et al. (2007).

A sub-field of passive control is tuned passive control, in which the characteristics of the passive control methods are tuned in situ, for example by changing the power through a secondary heater (chapter 4 and 5) or modifying the throat area of the system outlet via a mechanical iris (chapter 5 and 6). Tuned passive control via a secondary heater has been described by Katto and Sajiki (1977) and Sreenivasan et al. (1985). In Katto and Sajiki (1977) it was shown that a secondary heater located at $x/L = 0.75$ had a stabilising effect on the system when the primary heat source was located at $x/L = 0.25$. Sreenivasan et al. (1985) showed that thermoacoustic oscillations present in a flame-driven Rijke tube could be suppressed by introducing a control heater downstream of the primary heater.

Further reading on the passive control of thermoacoustic oscillations can be found in Culick (1988) and Schadow and Gutmark (1992).

1.3.2 Active feedback control

Active feedback control methods utilise a controlled actuator mechanism, which acts on a specific system parameter, modifying it based on data acquisition from a sensor (in the case of closed-loop active control) or modifying it according to its own intrinsic control algorithms (in the case of open-loop feedback control) (Dowling and Morgans, 2005). The sensor informs the controller whether the system parameter needs to be increased or decreased in order to effectively control (suppress) the oscillation. A concise overview of the methods available can be found in the reviews by McManus et al. (1993) and Dowling and Morgans (2005).

One of the earliest applications of feedback control in thermoacoustics was performed by Heckl (1988). In this study, a microphone was placed upstream of the heat source. The signal was phase-shifted, amplified and transmitted to a loudspeaker downstream. This simple feedback loop was able to suppress thermoacoustic oscillations in a Rijke tube. More recently, work on active feedback control of thermoacoustic oscillations has been performed by Zhang et al. (2015) and Zhao et al. (2015). Zhang et al. (2015) used a tunable Helmholtz resonator to control thermoacoustic oscillations. The Helmholtz resonator was optimised by modifying its throat area in real-time, thus allowing it to suppress thermoacoustic oscillations over a large frequency range. Zhao et al. (2015) employ active open-loop forcing via an electrical heater to suppress thermoacoustic oscillations in a premixed flame-driven Rijke tube. It was found that the degree to which the electrical heater can damp the thermoacoustic oscillations is strongly dependent on its position and output power. This study shows that an electrical heater placed downstream of the primary heat source can suppress thermoacoustic oscillations, as shown previously in the experimental study of Sreenivasan et al. (1985) and the theoretical study of Magri and Juniper (2013b).

Further reading on active control can be found in Candel (1992), Neumeier and Zinn (1996), Annaswamy et al. (2000), Blonbou and Laverdant (2000), Sattinger et al. (2000), and Annaswamy and Ghoniem (2002).

1.4 Sensitivity analysis and adjoint-methods in thermoacoustics

This section provides an overview of sensitivity analysis of thermoacoustic oscillations before exploring the benefits of employing adjoint-based sensitivity analysis.

1.4.1 Sensitivity analysis of thermoacoustic oscillations

In classical linear stability analysis, the eigenmodes of a linear system are calculated enabling one to determine whether that system is stable or unstable. According to Juniper and Magri (2014), sensitivity analysis typically quantifies: (i) the sensitivity of each mode to internal feedback (known as feedback sensitivity); and (ii) the sensitivity of each mode to changes in the base state (known as base state sensitivity).

Because the focus of this thesis is the application rather than derivation of sensitivity analysis to thermoacoustic systems, a thorough background of its use in fluid mechanics will not be given here. A selection of landmark papers regarding sensitivity analysis in fluid mechanics include Bottaro et al. (2003), Mohammadi and Pironneau (2004), Chomaz (2005), Giannetti and Luchini (2007), Marquet et al. (2008), Giannetti et al. (2010), Luchini and Bottaro (2014), and Schmid and Brandt (2014).

1.4.2 Adjoint-based sensitivity analysis

Adjoint-based sensitivity analysis was first introduced to thermoacoustic instability by Magri and Juniper (2013c). In traditional sensitivity analysis, the eigenvalues are calculated at a single operating point, a parameter is then varied slightly, and the eigenvalues are re-calculated at the new operating point. This approach gives the sensitivity of all the eigenvalues to a change in a single parameter. In adjoint-based sensitivity analysis, the eigenvalues are calculated for one operating point. Then one eigenvalue is selected and the governing equations reformulated such that the second calculation gives the sensitivity of that eigenvalue to a change in all parameters. In thermoacoustics, usually only a few eigenvalues are of interest, but many parameters can be modified. Adjoint-based sensitivity analysis is therefore much more efficient than traditional sensitivity analysis. In addition, the sensitivities calculated with a single adjoint calculation can be combined such that the effect of any passive device can be determined with one further cheap calculation. Using this technique, Magri and Juniper (2013a,c) were able to determine the effect a passive drag device and a secondary heater have on the shift in linear growth rate and shift in frequency of thermoacoustic oscillations. The sensitivity information obtained can be combined with optimization algorithms to develop optimal passive control strategies. It is important to note that this method is a linear technique, and therefore is only accurate for small changes to parameters.

1.4.2.1 Historical perspective

Adjoint methods were first used in the study of flow instability by Hill (1992) and independently by Chomaz (1993). The study used adjoint solutions of linearised equations of motion to numerically study the restabilisation effect seen by placing a small cylinder in specific locations of the wake of a larger cylinder

in low-Reynolds number flow. It was found that the results agreed well with the previously conducted experiments of Strykowski and Sreenivasan (1990). Other early studies which included the use of adjoint methods in flow instability can be found in work by Hill (1995). It was not until almost a decade later that the use of adjoint methods in flow instability became widespread with the landmark papers of Giannetti and Luchini (2007), Marquet et al. (2008) and Marino and Luchini (2009).

The use of adjoint methods in flow instability have been the subject of three review papers; Chomaz (2005) Sipp et al. (2010) and Luchini and Bottaro (2014).

1.4.2.2 Application to thermoacoustic systems

The use of adjoint methods in thermoacoustics is a recent endeavour. The first studies that applied adjoint methods to a thermoacoustic system were conducted by Juniper (2011a), Juniper (2011b) and Juniper (2012). The main focus of these studies was on the nonlinear aspects of the Rijke tube, which lead to transient growth and triggering.

The application of adjoint methods to sensitivity analysis in thermoacoustic systems has been developed over the past few years with several papers; Magri and Juniper (2013a,b,c, 2014a,b) and Juniper et al. (2014).

As the experimental campaigns conducted in chapters 3, 4, 5, and 6 of this thesis were carried out on an electrically heated Rijke tube, the work in Magri and Juniper (2013c) is the most relevant. In their paper, Magri and Juniper (2013c) study a horizontal Rijke tube with a hot-wire acting as a compact heat source. Their main investigations included: (i) the sensitivity of the linear growth rate and frequency of thermoacoustic oscillations to the addition of a passive control device into the system; and (ii) the sensitivity of the system to the location of a secondary heat source. An overview of the model used by Magri and Juniper (2013c) is discussed in chapter 2.

This work was extended and in the studies of Magri and Juniper (2013a), Magri and Juniper (2013b) and Magri and Juniper (2014b), a Rijke tube with a ducted heat source in the form of a diffusion flame is considered. The same numerical method outlined in Magri and Juniper (2013c) is applied to a horizontal Rijke tube geometry utilising a ducted diffusion flame in place of the hot wire heat source. The techniques in Magri and Juniper (2014b) show how to extend adjoint sensitivity analysis to complex geometries.

1.5 Determination of experimental growth and decay rates

The main focus of this thesis is based on experimental sensitivity analysis in thermoacoustic systems. A key component of this is the experimental determination of growth and decay rates. It is therefore worthwhile to provide some context.

A review paper by Huerre and Monkewitz (1990) provided a concise overview of the experimental techniques available for measuring growth rates in hydrodynamic systems. Huerre and Monkewitz (1990) explain that for the detection of self-excited global modes, there exists two suitable types of experiments: (i) the "easy" experiments for studying the steady-periodic behaviour of the system. This type of experiment is only useful for ascertaining whether self-excited oscillations exist; and (ii) the "hard" experiments which are focused on understanding the transient properties of a system. This type of experiment not only provides conclusive evidence of self-excitation, but it also allows for a more rigorous investigation of the system as it transitions from a non-oscillatory fixed point to a self-excited oscillatory state (the transient regime). In this thesis, this investigation was taken a step further to precisely measure linear growth and decay rates, as well as the oscillation frequencies observed during periods of

linear growth and decay. Hence, we are only interested in the transient regime, thus the "hard" experimental category applies.

Studying the transient behaviour of self-excited oscillations involves tracking a global instability through three stages: (i) onset, (ii) small-amplitude linear growth, and finally to (iii) saturation (Huerre and Monkewitz, 1990). Provansal et al. (1987) used the Stuart-Landau equation to describe the dynamical behaviour of the wake of a circular cylinder above and below a critical threshold, Re_c, when the flow is subjected to external forcing. While this paper is not related to thermoacoustics, it is relevant in the context of this thesis because it was one of the earliest studies to experimentally determine the growth rates of a hydrodynamic system as it transitions from a steady state to an oscillatory state. Strykowski and Sreenivasan (1990) also looked at the transient behaviour of the suppression of vortex shedding behind cylinders. Strykowski and Sreenivasan (1990) were able to experimentally obtain transient growth rates of velocity fluctuations using a hot-wire anemometer and found that the addition of a cylinder to the system resulted in reduced growth rates. It was also found that the suppression of vortex shedding, was consistent with no sharp spectral peaks and negative transient growth rates.

In the same framework as Provansal et al. (1987), Schumm et al. (1994) measured experimentally the coefficients of the Stuart-Landau equation: linear temporal growth rate, linear frequency and the Landau constant, by exciting the fundamental transverse bending mode of the bluff-body via the application of a sinusoidal voltage signal. This excitation caused the system to transition from a stable fixed point to a stable limit cycle.

More recently, Mejia et al. (2016) studied four experimental methods for extracting growth and decay rates on a methane-air laminar burner at a range of operating points. The methods were: (i) a harmonic response method in which a loudspeaker forced the flame in the linearly stable regime; (ii) a white noise

method in which a stochastic signal was used to force the flame in either the linearly stable or unstable region; (iii) an impulse response method in which an impulse signal was used to momentarily excite the flame in the linearly stable regime, allowing for a decay rate to be measured as the system returns to a steady-state; and (iv) an active control method which involved switching on and off an active controller in the unstable regime and measuring the temporal evolution of the oscillations. Fittings were applied to power spectral density and time-series signals of acoustic pressure fluctuations, acoustic velocity fluctuations and heat release fluctuations, from which the growth rate and oscillation frequency were determined. It was found that all four methods were suitable for determining the growth rates, decay rates, and frequencies of thermoacoustic oscillations. It was this work that inspired the "pulsed forcing technique" developed in chapter 5 of this thesis.

Further reading on the determination of growth and decay rates on larger combustion systems can be found in Noiray and Schuermans (2013), Stadlmair et al. (2017), and Hummel et al. (2017).

1.6 Thesis scope

The main aim and novelty of this thesis is to develop experimental methods for sensitivity analysis in thermoacoustics and to provide a first experimental comparison with the adjoint-based sensitivity analysis of Magri and Juniper (2013b). The objectives of the thesis are listed below.

1. To develop repeatable automated experimental techniques for determining linear growth rates, linear decay rates and frequencies observed during the growth and decay of thermoacoustic oscillations. Through these methods, several hundred experimental data points were obtained and a thorough uncertainty analysis of the random error was performed. This type of

rigorous analysis is rare in thermoacoustic studies due to the time and cost associated with experimental work.

2. To develop repeatable automated experimental techniques for performing experimental sensitivity analysis on a simple thermoacoustic system. The idea is to lay the foundation for further work by demonstrating that the techniques can work well for the simple configuration of an electrically-heated vertical Rijke tube.

3. To assess the effect of a variety of passive control devices on the linear growth rate, linear decay rate and oscillation frequencies observed during periods of linear growth and decay. The aim was to map out regions of the system where the linear growth rate and linear decay rate was most sensitive to a passive control device. These experimental mappings were compared with the predictions of adjoint-based sensitivity analysis and used in the development of optimal passive control strategies for the suppression of thermoacoustic oscillations.

4. To extend the experimental sensitivity analysis techniques developed for an electrically-heated Rijke tube to a real combustion system, a flame-driven Rijke tube.

5. To assess the sensitivity of the linear growth rates, linear decay rates and oscillation frequencies observed during periods of linear growth and decay to changes in the convective-time delay present in a flame-driven thermoacoustic system.

In the context of this thesis, the term linear growth rate refers to linear growth rates in which the growth of amplitude is proportional to the amplitude which can be represented by $da/dt = ka$. This relation gives rise to an exponential

growth in amplitude, i.e. exponential growth of the amplitude $a(t)$ is caused by the amplitude having a linear growth rate $da/dt \propto a$.

1.7 Thesis structure

This thesis contains five results chapters. The first four results chapters have been published as a peer-reviewed publication. The contributions of named authors are noted at the beginning of each chapter. The articles are:

1. Rigas, G., Jamieson, N. P., Li, L. K., Juniper, M. P. (2016). *Experimental sensitivity analysis and control of thermoacoustic systems.* Journal of Fluid Mechanics, 787, R1.

2. Jamieson, N. P., Rigas, G., Juniper, M. P. (2017). *Experimental sensitivity analysis via a secondary heat source in an oscillating thermoacoustic system.* International Journal of Spray and Combustion Dynamics. Special Edition. https://doi.org/10.1177/1756827717696325.

3. Jamieson, N.P., Juniper, M. P. (2017). *Experimental sensitivity analysis of a linearly stable thermoacoustic system via a pulsed forcing technique.* Experiments in Fluids. (58):123. https://doi.org/10.1007/s00348-017-2402-2.

4. Jamieson, N.P., Juniper, M. P. (2017). *Experimental sensitivity analysis and the equivalence of pulsed forcing and feedback control in thermoacoustic systems.* Proceedings of the ASME Turbo Expo 2017, Volume 4A: Combustion Fuels and Emissions. doi:10.1115/GT2017-63441.

Chapter 2 gives an overview of the model used by Magri and Juniper (2013c). As the results of Magri and Juniper (2013c) are referred to throughout the thesis,

it was thought that an overview of the main assumptions, governing equations, numerical implementation and results would be useful for completeness.

Chapter 3 investigates the effect of a passive drag device on the shift in linear growth rate and oscillation frequency observed during periods of linear growth. A novel, automated experimental procedure was used to perform the sensitivity analysis. The results were then compared to theoretical predictions from adjoint-based sensitivity analysis.

Chapter 4 investigates the effect of a secondary heat source on the shift in linear growth rate and oscillation frequency observed during periods of linear growth. A novel, automated experimental procedure was used to perform the sensitivity analysis and the results were compared to the theoretical predictions of adjoint-based sensitivity analysis. Both chapters 3 and 4 act as the first comparison of adjoint-based sensitivity analysis to experimental findings in thermoacoustics.

Chapter 5 presents the development of a novel pulsed forcing experimental technique that can be used successfully in the experimental sensitivity analysis of thermoacoustic systems. The technique, inspired by Mejia et al. (2016), was approximately 12 times faster than the methods used in chapters 3 and 4. In chapter 5, a passive drag device, secondary heat source, and a variable area outlet (in the form of a mechanical iris) were used as control devices and their effect on the linear decay rate and oscillation frequency during periods of linear decay was investigated.

Chapter 6 presents an investigation of the prediction of zero growth rate by both the pulsed forcing method (developed in chapter 5) and feedback control in thermoacoustic systems. These experimental methods were investigated in the presence of a variable area outlet (a mechanical iris) at the downstream end of the Rijke tube. This chapter is important as it shows that both the pulsed

forcing method and feedback control can be used for experimental sensitivity analysis in thermoacoustic systems.

Chapter 7 presents an experimental sensitivity analysis performed on a flame-driven Rijke tube. The flame used was a ducted premixed conical laminar flame. This chapter shows how the techniques developed in chapters 3, 4, 5 and 6 can be applied to a real combustion system. Finally, the chapter presents an investigation into the sensitivity of the linear growth rates, linear decay rates and oscillation frequencies observed during periods of growth and decay to changes in convective time delay, one of the most sensitive parameters in any thermoacoustic system (Juniper and Sujith, 2018).

This thesis culminates with a summary of the main findings and suggestions for future work.

Chapter 2

Details of the adjoint-based model

This chapter gives a concise overview of the model used by Magri and Juniper (2013c). As the results of Magri and Juniper (2013c) are referred to throughout this thesis, it was thought that for completeness, an overview of the main assumptions, the governing equations, numerical implementation, and the results of the model would be useful. It should be noted that the work contained in this chapter was not completed by the author, but is a summarised overview of the work conducted by Luca Magri and Matthew Juniper in Magri and Juniper (2013c).

2.1 Introduction

In this chapter, the model used by Magri and Juniper (2013c) is explored. Firstly, the main assumptions and governing equations are discussed, followed by an overview of the adjoint-based equations used in the sensitivity analysis. As this chapter is more focused on the model itself, the numerical implementation of the adjoint-based model is not discussed in great detail. For further information on how the model was numerically implemented refer to Magri and Juniper (2013c). The chapter culminates with a discussion of the main findings of Magri and Juniper (2013c).

It should be stressed that the analysis presented in Magri and Juniper (2013c) is based on a highly simplified model and only attempted to give a qualitative description of the effects of a passive drag device and a secondary heat source on the shift in linear growth rate, linear decay rate and frequency observed during periods of linear growth and decay. Therefore, in comparing the results of Magri and Juniper (2013c) to the experimental results contained in this thesis it is important to remember that significant work needs to be done to update the current adjoint-based model to yield an accurate quantitative comparison.

2.2 The model

2.2.1 Governing equations and main assumptions

The thermoacoustic system that was investigated by Magri and Juniper (2013c) was that of a horizontal Rijke tube which was open at both ends and driven by an electrical heater (assumed to be a point source). The thermoacoustic system described above is governed by the following non-linear equations:

$$\frac{\partial u}{\partial t} + \frac{\partial p}{\partial x} = 0 \tag{2.1}$$

$$\frac{\partial p}{\partial t} + \frac{\partial u}{\partial x} + \zeta p - \dot{q} = 0 \tag{2.2}$$

$$\dot{q} = \frac{2}{\sqrt{3}}\beta\left(\left|\frac{1}{3} + u(t-\tau)\right|^{1/2} - \left(\frac{1}{3}\right)^{1/2}\right)\delta(x - x_h) \tag{2.3}$$

where u, p, $\dot{q}$, and ζ are the non-dimensional velocity, pressure, heat release rate, and damping factor, respectively. Equation 2.1 is the non-linear momentum equation, equation 2.2 is the energy equation written in terms of pressure and equation 2.3 is a modified version of King's law (Heckl, 1988). Within equation 2.3, it was assumed that the β term included all relevant information about the electrical heater, base velocity and ambient conditions; τ is the time-delay between velocity perturbations and heat release rate perturbations; and the position of the electrical heater is modelled as a Dirac delta function, $\delta(x - x_h)$, with the electrical heater being placed at $x = x_h$.

It can be seen in equations 2.1, 2.2 and 2.3 that there are four control parameters that are able to be tweaked within the model. These are the damping factor, ζ, the heat release parameter, β, the time-delay, τ, and the position of the electrical heater, x_h. The damping factor, $\zeta_j = c_1 j^2 + c_2\sqrt{j}$, models the dissipation and end losses in each j-th mode, where c_1 and c_2 are constants.

The heat release rate (equation 2.3) was then linearized in the time-delay and in the amplitude of u around a fixed point in the system assuming $|u| << 1$:

$$\dot{q} = \beta\left(u + \tau\frac{\partial p}{\partial x}\right)\delta(x - x_h) \tag{2.4}$$

The partial differential equations shown in equations 2.1, 2.2, and 2.4 were then discretized into a set of ordinary differential equations using the Galerkin method. The boundary conditions used in the analysis were: at the ends of the tube (i) p was set to zero, and (ii) $\partial u/\partial x$ was set to zero. These boundary conditions

meant that the system could not dissipate acoustic energy by doing work on the surroundings. A detailed discussion of the numerical discretization methodology used by Magri and Juniper (2013c) was not considered essential to this chapter and is therefore only briefly mentioned. For further information please see Magri and Juniper (2013c).

To summarise, the main assumptions used in the model of Magri and Juniper (2013c) were:

1. Equations 2.1 and 2.2 were derived from the Navier-Stokes equations and energy equations assuming first-order acoustics.

2. One-dimensional acoustic standing waves in the Rijke tube changed the mean flow velocity at the primary heat source, which caused a change in the heat transfer from the primary heater to the air.

3. The heat release rate was modelled as a modified form of King's law (equation 2.3) which included a time-delay term, τ. The value for β used throughout the analysis was 0.5. It was assumed that β encapsulated all relevant information about the electrical heater. I.e. wire properties, ambient properties and the temperature change across the heater. As the value of β was kept constant throughout the analysis, the unsteady heat release rate did not correspond to a physical heater power. This assumption would need to be re-visited should one wish to update the model to yield a more accurate quantitative comparison. A re-formulation would need to occur which would allow the heat release rate parameter to be compared to the power given to the primary heater in the experiment. A method for accurately measuring the mean flow velocity through the tube should also be devised. If this was a measured quantity, it could be incorporated into an updated model of the base flow.

4. The adjoint-based sensitivity analysis was a linear analysis. I.e. the governing equations (equations 2.1, 2.2, and 2.4) were linearised, assuming for equation 2.4 that $|u| << 1$ and τ is very small compared with the period of the highest Galerkin mode, respectively. The small amplitude assumption was fine for the experiments contained in this thesis. The linearization of the time delay is more problematic, but we are moving away from that now by using wave-based acoustics rather than Galerkin acoustics (Aguilar et al., 2017). This assumption would need to be re-visited should one wish to update the model to yield a more accurate quantitative comparison. This is currently the focus of two current PhD students in the Cambridge University Engineering Department.

5. The temperature inside the Rijke tube is modelled as T_1 between $x = 0$ and $x = x_h$, and T_2 between $x = x_h$ and $x = L$. This assumption would need to be re-visited should one wish to update the model to yield a more accurate quantitative comparison. A model for heat transfer similar to that used by Matveev and Culick (2003) could be used to better capture the physical changes in temperature within the system.

6. The boundary conditions used in the analysis were p and $\partial u/\partial x$ were equal to zero at the ends of the Rijke tube. These boundary conditions are currently being updated through the use of measured data from the multi-microphone method. This work was started by the author and was passed onto the proceeding PhD student.

2.2.2 Adjoint-based equations and sensitivity analysis

This section outlines the adjoint-based equations that were used in the sensitivity analysis of Magri and Juniper (2013c). A brief overview of the two sets of adjoint-equations is given. For derivations and further detail regarding the

mathematics please see Magri and Juniper (2013c). The eigenvalue analysis is then discussed which resulted in the equations for (i) eigenvalue drift in the presence of a secondary heat source, and (ii) the structural sensitivity tensor for the introduction of a passive drag device. The physical descriptions of these equations are given in §2.3. For further information on the derivations refer to Magri and Juniper (2013c).

The adjoint-equations can be derived from the continuous direct equations and then discretized (continuous adjoint - CA). The CA method involves integrating the continuous equations by parts and then applying Green's theorem as defined in Magri and Juniper (2013c). The adjoint-equations can also be derived from the discretized equations (discrete adjoint, DA), but a discussion of this was beyond the scope of this summary chapter. A set of CA adjoint equations were derived from equations 2.1, 2.2, and 2.4. The adjoint-equations derived from equations 2.1, 2.2, and 2.4 are referred to as CA_1:

$$\frac{\partial u^+}{\partial t} + \frac{\partial p^+}{\partial x} + \beta p^+ \delta(x - x_h) = 0 \tag{2.5}$$

$$\frac{\partial u^+}{\partial x} + \frac{\partial p^+}{\partial t} - \zeta p - \beta\tau \frac{\partial [p^+ \delta(x - x_h)]}{\partial x} = 0 \tag{2.6}$$

The above equations govern the behaviour of the adjoint variables, u^+ and p^+, which can be thought of as Lagrange multipliers. Thus u^+ is the Lagrange multiplier of the acoustic momentum equation (equation 2.1). This can be physically thought of as the spatial distribution of the thermoacoustic system's sensitivity to a force (Magri and Juniper, 2013c). Similarly, p^+ is the Lagrange multiplier of the pressure equation (equation 2.2) and equation 2.4. This can be physically thought of as the thermoacoustic systems sensitivity to heat addition.

The difference in these equations occurs due to the different governing equations used but has no physical significance.

Magri and Juniper (2013c) then transform equations 2.1, 2.2, 2.4 and the adjoint-equations 2.5 and 2.6 from the (x,t) domain to the (x,σ) domain by substituting in $u(x,t) = \hat{u}(x,\sigma)e^{\sigma t}$, $u^+(x,t) = \hat{u}^+(x,\sigma)e^{-\bar{\sigma}t}$, $p(x,t) = \hat{p}(x,\sigma)e^{\sigma t}$, and $p^+(x,t) = \hat{p}^+(x,\sigma)e^{-\bar{\sigma}t}$. Magri and Juniper (2013c) then introduced a small perturbation to the linearized system described above: $\sigma_{new} = \sigma + \delta\sigma$, $\hat{p}_{new} = \hat{p} + \delta\hat{p}$, and $\hat{u}_{new} = \hat{u} + \delta\hat{u}$, where $\delta\sigma = \epsilon\sigma$, $\delta\hat{p} = \epsilon\hat{p}$, $\delta\hat{u} = \epsilon\hat{u}$ and $|\epsilon| << 1$.

Magri and Juniper (2013c) then go onto derive two equations. The first equation was the structural sensitivity tensor for a general feedback mechanism via CA_1:

$$S = \frac{\delta\sigma}{\delta C_1} = \frac{\begin{bmatrix} \hat{\hat{u}}^+ & \hat{\hat{p}}^+ \end{bmatrix}^T \otimes \begin{bmatrix} \hat{u} & \hat{p} \end{bmatrix}^T}{\int_L (\hat{u}\hat{\hat{u}}^+ + \hat{p}\hat{\hat{p}}^+)dx} \tag{2.7}$$

where:

$$\delta C_1 = \begin{bmatrix} 0 & 0 \\ \delta\beta_c\delta(x-x_h) & \delta\beta_c\tau_c\delta(x-x_h)\frac{\partial}{\partial x} \end{bmatrix} \tag{2.8}$$

In equations 2.7 and 2.8, δC represents the structural perturbation by applying the Green's identity (defined in Magri and Juniper (2013c)) to the perturbed direct and adjoint-equations, the subscript c represents the parameters used in the model of secondary heat source (discussed in §2.3.2), $\hat{}$ represents the complex-conjugate adjoint eigenfunctions, and L represents the linear operator defined by the Green's identity defined in Magri and Juniper (2013b).

The second equation was the change in the eigenvalue due to the presence of a secondary heat source with a small heat release parameter, $\delta\beta_c$ via CA_1:

$$\frac{\delta\sigma}{\delta\beta_c} = \frac{\hat{\hat{p}}_c^+\left(\hat{u}_c + \tau_c\frac{\partial\hat{p}_c}{\partial x}\right)}{\int_L (\hat{u}\hat{\hat{u}}^+ + \hat{p}\hat{\hat{p}}^+)dx} \tag{2.9}$$

where the parameters in equations 2.9 have the same meanings as defined above.

In §2.3, equations 2.7 and 2.9 are used to show how sensitive the linear growth rate and frequency observed during periods of growth was to (i) the introduction of a passive drag device; and (ii) the introduction of a secondary heat source. It was these results that were most relevant to this thesis.

2.3 Main results

This section summarises the results of Magri and Juniper (2013c) that were relevant to the remainder of this thesis. Each section below gives the main result and a physical description of what that result represents.

As mentioned above, Magri and Juniper (2013c) determine the adjoint-equations via two different methods, the continuous adjoint (CA) and the discrete adjoint (DA) methods. Each result discussed below was calculated via both methods and found to be essentially identical. As this chapter is concerned with a the results of Magri and Juniper (2013c) and a physical interpretation of them, the various methods used to derive the adjoint-equations are beyond the scope of this chapter. Therefore, only one result line which represents the results of both derivation methods is plotted below for ease of explanation.

2.3.1 Sensitivity to a passive drag device

This section shows the results of Magri and Juniper (2013c) for the sensitivity of the linear growth rates and oscillation frequencies observed during periods of linear growth to an introduction of a passive drag device. The four components of S (equation 2.7) quantify how a feedback mechanism that is proportional to the state variables affects the linear growth rates and observed frequency during periods of linear growth (Magri and Juniper, 2013c). Of relevance is the component S_{11}, which demonstrates the effect that a feedback mechanism which is proportional to the velocity and that forces the momentum equation (equation

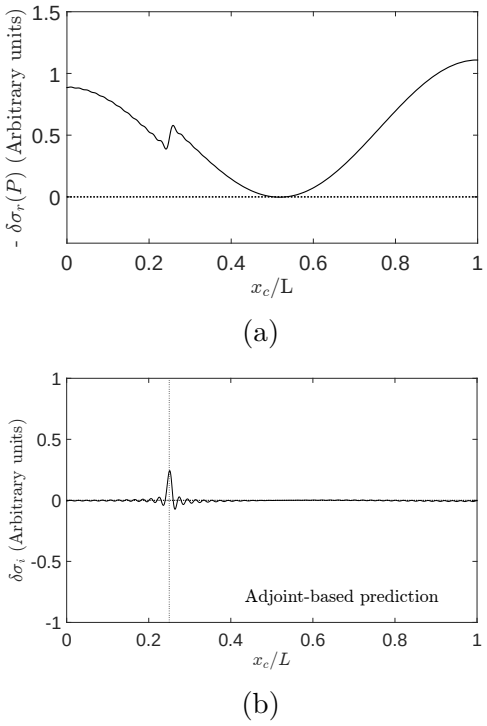

Fig. 2.1 (a) Shift in linear growth rate due to the introduction of a passive drag device. (b) Shift in frequency during periods of linear growth dur to the introduction of a passive drag device. The model parameters used were $\tau = 0.01$, $\beta = 0.5$, $c_1 = 0.01$, and $c_2 = 0.004$. These figures were adapted from Magri and Juniper (2013c)

2.1) has on the linear growth rate and frequency observed during periods of linear growth. This type of feedback mechanism could be introduced experimentally in the form of a passive mesh (drag device). The real (linear growth rate) and imaginary (frequency) components of S_{11} are taken from Magri and Juniper (2013c) and shown in figure 2.1a and b.

It can be seen in figure 2.1a that the passive drag device has the greatest effect on the system when placed at the ends of the tube. This is because the velocity mode is maximal there. The passive drag device imparts a drag force ($D = \frac{1}{2}\rho u^2 A C_d$) in the opposite direction to the velocity mode. When the velocity is at a maximum the drag force will also be at a maximum because the drag force scales with u^2. Physically, the introduction of the passive drag device induces flow perturbations which result in the system becoming more damped leading to

losses in acoustic energy. It can also be seen that the shift in linear growth rate is negative for all locations of the passive drag device, x_c/L. This means that the introduction of a passive drag device will always have a stabilising effect.

In figure 2.1b, Magri and Juniper (2013c) predict that the introduction of a passive drag device has no effect on the shift in frequency observed during periods of linear growth. It is experimentally found in chapter 3 and 4 that this is not the case. The physical reasons for this are discussed in chapter 3 and 4, respectively.

2.3.2 Sensitivity to a secondary heat source

This section shows the results from Magri and Juniper (2013c) for the sensitivity of the linear growth rates and oscillation frequency observed during periods of linear growth due to the introduction of a secondary heat source. Equation 2.9 was used by Magri and Juniper (2013c) to investigate the sensitivity of the system to the introduction of a secondary heat source. The secondary heat source was modelled in Magri and Juniper (2013c) by adding a $\dot{q}$ term (equation 2.3) to equation 2.2 and replacing β, τ, and x_h with β_c, τ_c, and x_c. The real (linear growth rate) and imaginary (frequency) components of $\delta\sigma/\delta\beta_c$ are taken from Magri and Juniper (2013c) and shown in figure 2.2a and b.

It can be seen in figure 2.2a that the secondary heat source has a destabilising effect on the system when $0 < x_c/L <$0.56 and a stabilising effect on the system when $0.56 < x_c/L < 1$. It can also be seen in figure 2.2b that the secondary heat source causes a positive shift in the oscillation frequency observed during periods of linear growth when $0 < x_c/L <$0.56 and causes a negative shift in the oscillation frequency observed during periods of linear growth when $0.56 < x_c/L < 1$.

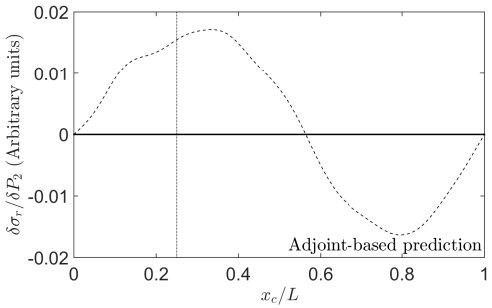

(a)

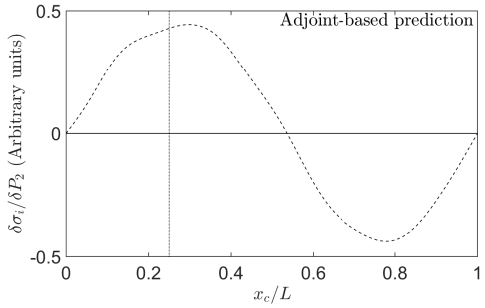

(b)

Fig. 2.2 (a) Shift in linear growth rate due to the introduction of a secondary heat source. (b) Shift in frequency during periods of linear growth dur to the introduction of a secondary heat source. The model parameters used were $\tau = \tau_c = 0.01$, $\beta = 0.5$, $\beta_c = \beta/10$ $c_1 = 0.01$, and $c_2 = 0.004$. These figures were adapted from Magri and Juniper (2013c)

To explain the physical mechanism it is convenient to recall that (i) the fundamental acoustic mode has a pressure node at either end of the tube and an antinode at the midpoint; and that (ii) the acoustic velocity has a node at the centre and an antinode at either end. During the compression phase of the acoustic cycle, the acoustic velocity is directed towards the centre of the tube, causing the pressure in the tube to increase. When the heater is placed in the upstream half of the tube, the acoustic velocity and the mean velocity are in the same direction during the compression phase. This causes the air speed around the heater, and therefore the heat transfer to be larger than average during the compression phase. Critically, there is also a time delay (Lighthill, 1954) between the velocity at the heater and the subsequent heat release rate. These two properties mean that, over an acoustic cycle, more heat release occurs

during moments of higher pressure than occurs during moments of lower pressure, causing more mechanical work to be done by the gas expanding during the expansion phase than is needed to compress it during the compression phase (Rayleigh, 1878). This results in the amplitude of acoustic oscillations growing until the heat release rate perturbations saturate and the excess work is balanced through acoustic radiation, viscous losses and thermal losses. When the heater is placed in the downstream half of the tube, the opposite is true, resulting in the heater having a stabilising effect on the system. This physical explanation is re-iterated in chapter 4 and a simple mathematical treatment is provided.

2.4 Concluding remarks

This chapter has given an overview of the model used by Magri and Juniper (2013c) which the remaining chapters of the thesis attempt to experimentally validate. This chapter was included so that the reader does not have to keep referring to the paper of Magri and Juniper (2013c). In the following chapters, experimental results are obtained and explained in the context of this chapter.

It should be stressed that the model outlined in this chapter is very much a highly simplified model and that Magri and Juniper (2013c) did not attempt to accurately quantify what would be later found in experimentally. An updated model is currently under development and briefly discussed in chapter 8.2. Furthermore, as this chapter's main purpose was to elaborate on the assumptions of the model of Magri and Juniper (2013c), the mathematical derivations contained in Magri and Juniper (2013c) were out of scope. Interested readers are referred to Magri and Juniper (2013c) for further information.

Chapter 3

Sensitivity analysis and passive control via a drag device

This chapter has been published as a journal paper in Rigas et al. (2015). All experiments were completed by the the author, the post-processing was completed in equal parts with Georgios Rigas and the automation procedure was conceived in equal parts with Georgios Rigas and implemented in National Instruments LabVIEW by Georgios Rigas.

3.1 Introduction

In this chapter, we investigate the passive control of a simple thermoacoustic system, an electrically-heated Rijke tube, via a passive drag device placed downstream of the heater. We carefully measure and compare experimental results with theoretical predictions from adjoint sensitivity analysis. The findings suggest that adjoint-based methods can provide industry with a valuable tool for developing optimal control strategies for more complex thermoacoustic systems.

3.2 Experimental set-up

Experiments were conducted on a 1 m long stainless steel vertical Rijke tube with an internal diameter of 47.4 mm and a wall thickness of 1.7 mm (figure 3.1). Two identical heaters were used. The primary heater was attached to two rods and held in place at $x_p/L = 0.25$, the optimal position for exciting thermoacoustic oscillations (Saito, 1965). It was powered by a 640 Watt EA Elektro-Automatik EA-PSI 5080-20 A DC programmable power supply. The secondary heater was used as a passive drag device with no power input. The passive drag device was attached to an automated digital height gauge at the top of the Rijke tube, enabling it to be traversed with an accuracy of ± 0.01 mm. The primary heater and passive drag device are shown in appendix A. A Brüel Kjaer condenser type 2619 microphone with a sensitivity of 11.4 mV Pa^{-1} was used to measure pressure fluctuations. The microphone was angled at 45° and placed 55 mm from the bottom end of the tube. The raw pressure signal was sampled at 10 kHz, much higher than the anticipated frequencies of the thermoacoustic oscillations, approximately 190 Hz. Data was acquired via a National Instruments BNC-2110 DAQ device using LabVIEW. Two type-K thermocouples, with an accuracy of ±1 K, were used to measure the air flow temperature at the inlet and outlet

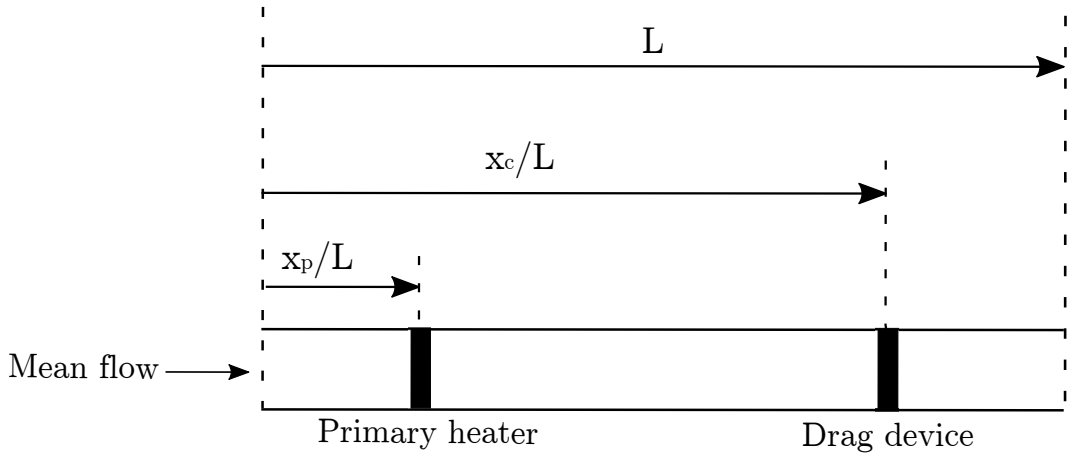

Fig. 3.1 Experimental set-up. Where L is the length of the Rijke tube; x_c/L is the position of the passive drag device; and x_p/L is the position of the primary heater.

of the Rijke tube. Five type-K thermocouples were attached to the outside of the Rijke tube, at $x/L = 0.05$, 0.25, 0.55, 0.75 and 0.95, to monitor the surface temperature of the tube. The temperature data was sampled at a frequency of 1 Hz and logged with an Omega TC-08 DAQ.

Near the open end of the tube, the phase and amplitude depend strongly on the position of the microphone. This does not matter, however, because (i) we are only concerned with the growth of the amplitude relative to the baseline, and (ii) we are not concerned with the phase. It would become a problem if the reflection coefficient were to depend on amplitude within the range of amplitudes that were examined within the linear regime, because then the position of the pressure node would change relative to the microphone. Over the small amplitudes that were considered, it is safely assumed that the reflection coefficient is constant.

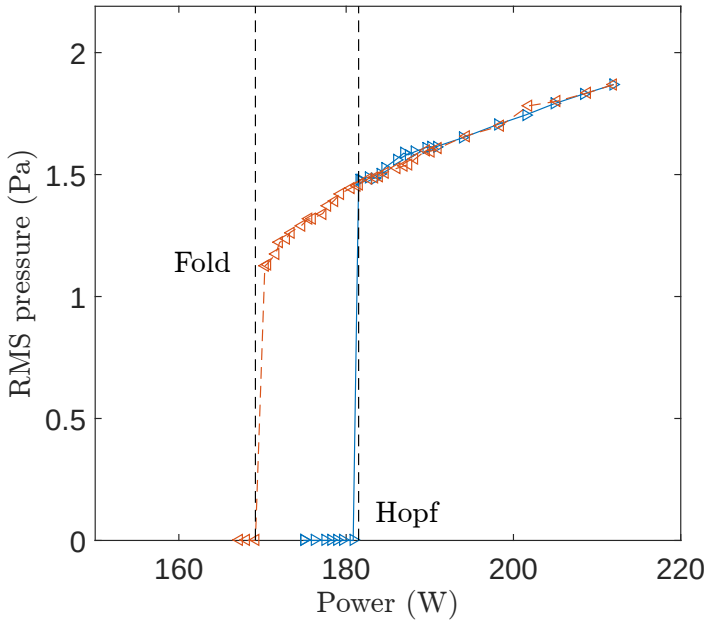

Fig. 3.2 Bifurcation diagram obtained experimentally on the Rijke tube. The system becomes unstable through a subcritical Hopf bifurcation. The forward path (right-pointing triangles) shows the position of the Hopf point, and the backward path (left-pointing triangles) shows the position of the fold point.

3.3 Baseline

The baseline experiments were performed without the passive drag device. The electric heater was fixed at $x_p/L = 0.25$ and the power supplied to it was used as the control parameter.

Figure 3.2 shows the steady-state root-mean-square amplitude of the pressure signal as a function of the heater power. The heater power was increased in ≈ 0.8 W increments until the Hopf point was found (forward path), and then decreased in ≈ 0.8 W increments until the fold point was found (backward path). When the Hopf point was found, the pressure signal grew in amplitude leading to a stable limit-cycle. When the fold point was found, the system returned to a stable fixed point. A hysteresis region of approximately 15 W wide exists between the Hopf and fold points, characteristic of the subcritical bifurcations

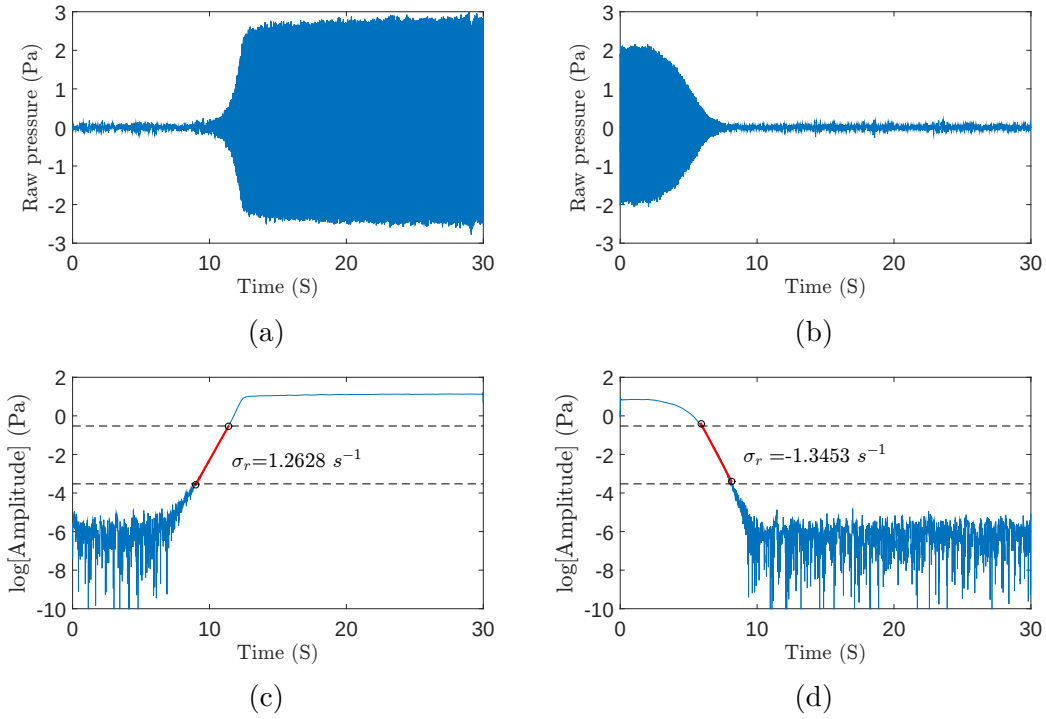

Fig. 3.3 Top: transient pressure signals obtained by applying step changes to the heater power input. (a) Growth, from $P_H - \epsilon$ to $P = 223$ W. (b) Decay, from $P_f + \epsilon$ to $P = 140$ W. Bottom: logarithm of the amplitude of the filtered pressure signals obtained by using the Hilbert transform. The linear growth (c) and linear decay (d) regions are represented by the red lines fitted between the noise floor and the point where nonlinear effects become important.

observed in similar thermoacoustic systems (Crocco et al., 1969; Mariappan, 2011; Matveev, 2003; Subramanian et al., 2013).

3.3.1 Linear growth rates, linear decay rates and oscillation frequencies

The linear growth rates, linear decay rates, and oscillation frequencies were measured, in the small amplitude regime, for a range of heater powers.

To obtain the linear growth rates and oscillation frequencies at heater power P, the heater power was initially set just below that of the Hopf point, $P_H - \epsilon$, where $\epsilon = 15$ W. This value of ϵ was the minimum such that triggering due to environmental disturbances was avoided (Juniper, 2011b). The heater power

was then increased abruptly to P. Oscillations grew to a limit-cycle (figure 3.3a) and the linear regime was identified as that in which the oscillations grew exponentially (figure 3.3c).

To obtain the linear decay rates and oscillation frequencies at power P, the heater power was initially set just above that of the fold point, $P_F + \epsilon$. It was then decreased abruptly to P. Oscillations decayed to a stable fixed point (figure 3.3b) and the linear regime was identified as that in which the oscillations decayed exponentially (figure 3.3d).

The procedure described above to obtain growth and decay rates was repeated for a range of heater powers P above the Hopf point and below the fold point, respectively. A bandpass Butterworth filter was applied to the raw pressure signal to reduce the noise, enabling clean regions of linear growth and decay to be identified. The instantaneous amplitude, $A(t)$, and phase, $\phi(t)$, of the pressure signal was extracted with the Hilbert transform, in a similar framework to Schumm et al. (1994). In Matlab, the `hilbert` function determines an analytical signal of the form $X(t) = x(t) + ix_H(t) = A(t)e^{i\phi(t)}$, where $x(t)$ is the original signal, $A(t)$ and $\phi(t)$ have the same definition as above, and the Hilbert transform of $x(t)$ is $x_H(t) = \pi^{-1} P.V. \int_{-\infty}^{\infty} \frac{s(\tau)}{t-\tau} d\tau$, where $P.V.$ indicates that the Cauchy principal value is taken. Whilst $A(t)$ and $\phi(t)$ can be computed via this method for any arbitrary $x(t)$, they only have a physical meaning if the signal is narrowband and has a dominant frequency peak (Pikovsky et al., 2003), as was the case for our signal. The linear growth and decay regions were defined as the regions between the noise floor, $A > \exp(-3.53) \approx 0.03$ Pa, and the amplitude threshold where nonlinear effects become important, $A > \exp(-0.52) \approx 0.59$ Pa. In the linear regime, the growth/decay rate is $\sigma_r = d(log(A))/dt$ and the frequency is $\sigma_i = d\phi/dt$.

Within the linear growth and decay regions defined above, constant growth/decay rates and frequencies were fitted to the data using linear regression, and the

results are shown in figure 3.4. Close to the critical power, $P_{crit} = P_H$, the growth rate and frequency can be approximated by

$$\sigma \simeq \sigma(P_{crit}) + [P - P_{crit}] \left. \frac{d\sigma}{dP} \right|_{P_{crit}}, \tag{3.1}$$

where $\sigma = \sigma_r + i\sigma_i$, as shown in figure 3.4 by the fitted lines. Notice that σ_i is expressed in Hz. For the baseline case, $P_{crit} = 181.49$ W, and $\sigma_r(P_{crit}) = 0$. It was found that $\sigma_i(P_{crit}) = 183.81$ Hz, and the gradients are $d\sigma_r/dP = 0.0236$ and $d\sigma_i/dP = 0.0211$ $(\text{Ws})^{-1}$. It can be seen in figure 3.4 that the growth rates and frequencies that are measured by applying a step change to the power of the primary heater exhibit a linear trend. There is no reason to expect this result to be linear a priori, but it was observed to be so.

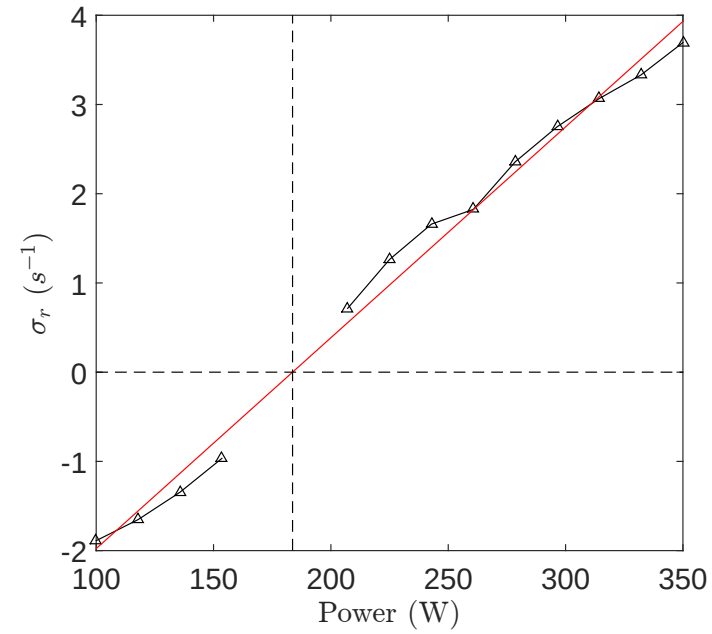

(a)

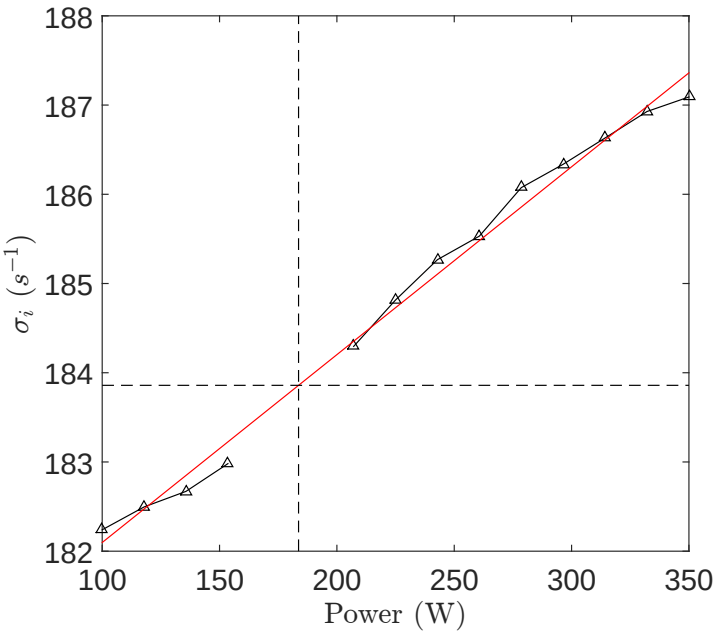

(b)

Fig. 3.4 Linear stability characteristics for baseline case as a function of the primary heater power: (a) Linear growth and decay rate, σ_r; (b) oscillation frequency, σ_i. Experimental data (symbols) and linear fit (red line).

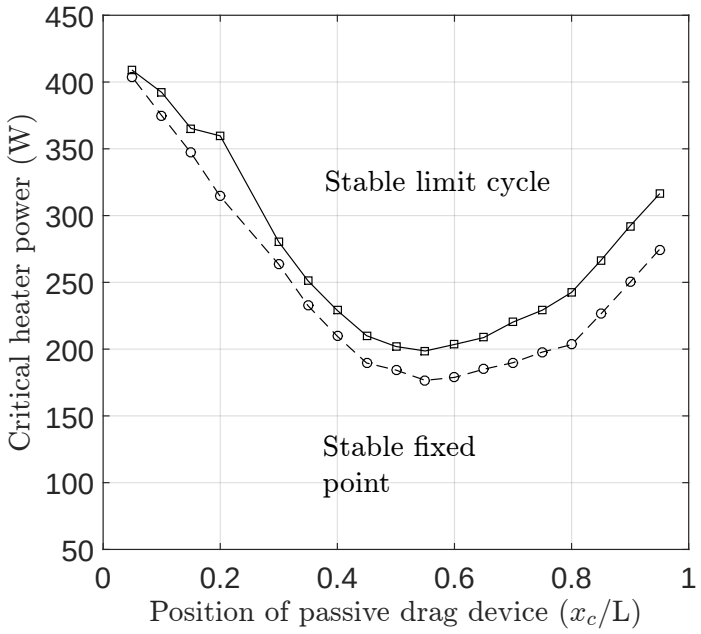

Fig. 3.5 Stability regions as a function of the passive drag device position. Forward path critical powers: Hopf points (squares); backward path critical powers: fold points (circles). A bistable region exists between the two lines.

3.4 Passive control via a drag device

In this section, we examine the change of the linear stability characteristics of the system, quantified as shifts in the linear growth rate and oscillation frequency, that was caused by the introduction of a passive drag device. The eigenvalue shift defined in the theoretical analysis of Magri and Juniper (2013c) was obtained here experimentally as:

$$\delta\sigma(x_c, P) = \sigma_c(x_c, P - P_{crit,c}) - \sigma_0(P - P_{crit,0}). \tag{3.2}$$

where the subscript c corresponds to the case with the passive drag device installed and the subscript 0 to the baseline case. A procedure similar to the

one followed in §3.3 was followed to obtain σ_c, when the passive drag device was placed at x_c/L from 0.05 to 0.95.

3.4.1 Effect on critical power

For each position x_c of the passive drag device, a bifurcation diagram similar to figure 3.2 was obtained enabling the Hopf and fold points to be located. These are shown in figure 3.5. The minimum forward and backward path critical powers correspond to the passive drag device being positioned at $x_c/L = 0.55$, and the maxima towards the two ends of the tube. To a first order, the sensitivity of the linear growth rate around the critical baseline power is proportional to the change of the critical power in the presence of a control device. An estimate of the sensitivity of the linear growth rate can be obtained from the critical power shift. However, in this study we measured it directly, as described in §3.4.2.

3.4.2 Shift in linear growth rate

The linear growth rates and oscillation frequencies were measured experimentally for various heater powers, P, and axial positions, x_c, of the passive drag device. A comparison with the baseline at the same heater power P gives the linear growth rate and oscillation frequency shift, $\delta\sigma$, caused by the passive drag device. Time series were measured to obtain the linear growth and decay rates and are plotted for $x_c/L = 0.4$ in figure 3.6. Data were acquired for various axial locations, x_c/L; for brevity, only one case is shown. A map of the linear growth and decay rates as a function of heater power and x_c/L is shown in figure 3.7a, and a map of the shift in linear growth rate relative to the baseline is shown in figure 3.7b. By subtracting the baseline measurements from the measurements observed in the presence of a passive drag device, the effect of just the passive drag device was determined (figure 3.7b). This was sufficient as the baseline measurements

contained all information regarding the perturbation effects introduced by the primary heater due to drag and the unsteady heat release rate, leaving only the measured data showing the effect of the passive drag device.

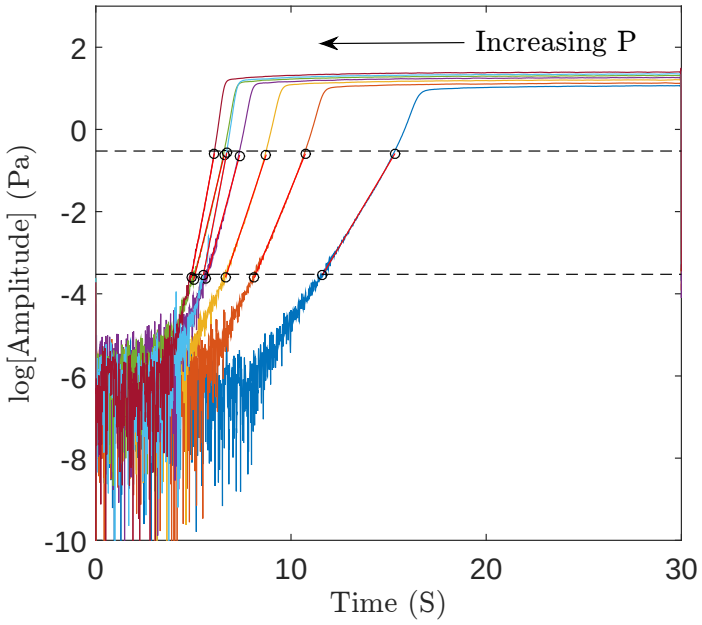

(a)

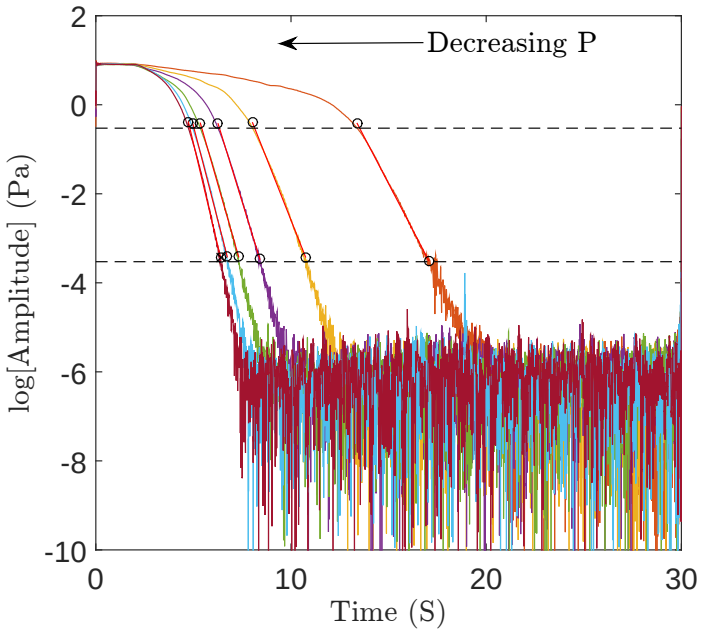

(b)

Fig. 3.6 (a) Linear growth rates and (b) linear decay rates, $\sigma_{r,c}$, obtained with the passive drag device positioned at $x_c/L = 0.4$. Each curve represents the amplitude response for a different step size above or below the Hopf or fold point.

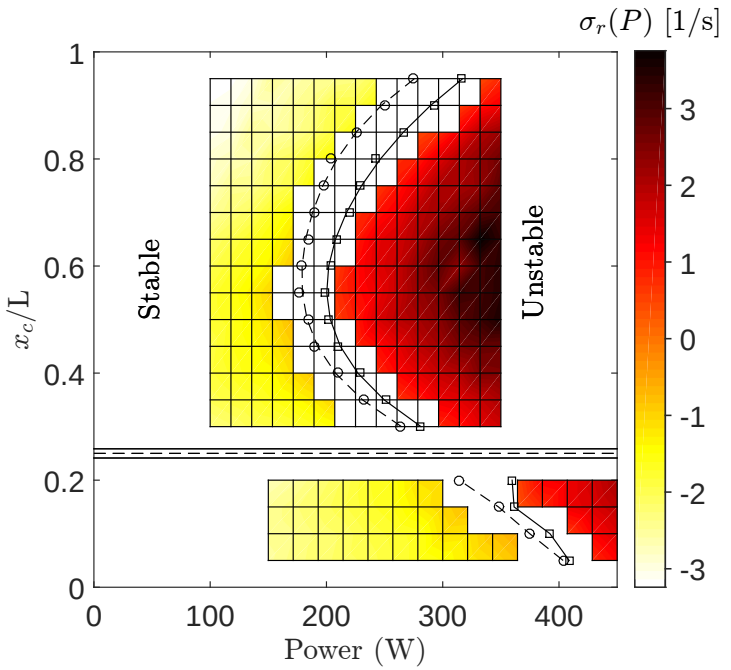

(a)

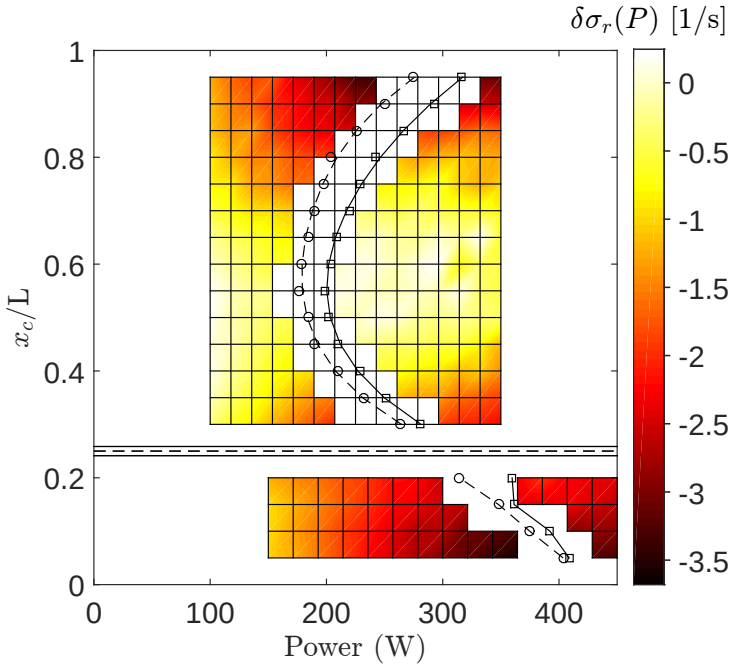

(b)

Fig. 3.7 (a) Linear growth rate and (b) shift in linear growth rate, experimentally obtained, as a function of power supplied to the heater and position of the passive drag device. Forward path critical powers (squares) and backward path critical powers (circles). The primary heater was located at $x_c/L = 0.25$.

In figure 3.8 we qualitatively compare the experimentally measured linear growth rate shift with the theoretical predictions from Magri and Juniper (2013c). Each experimental curve corresponds to a different heater power, P, which is shown in the legend. It can be seen in figure 3.8, that as P is increased, the measured shift in linear growth rate increases until $P = 385.7$ W, after which the measured shift in linear growth rate begins to decrease. The mean of these is given as a visual aid for the general qualitative behaviour of the system, not for comparison with the model of Magri and Juniper (2013c). In agreement with the predictions, the largest changes in linear growth and decay rates occur when the drag device is positioned at the ends of the Rijke tube: $x_c/L = 0.05$ and 0.95. The passive drag device has the greatest effect on the system when placed at the ends of the tube because the velocity mode is maximal there. The passive drag device imparts a drag force ($D = \frac{1}{2}\rho u^2 A C_d$) in the opposite direction to the velocity. When the velocity is at a maximum the drag force will also be at a maximum because the drag force scales with u^2. Physically, the introduction of the passive drag device induces flow perturbations which result in the system becoming more damped causing an acoustic energy loss. In comparing the experimental results with the results from adjoint-based sensitivity analysis (figure 3.8), it is clear that the theoretical results predict the main features of the physical observations. The results of Magri and Juniper (2013c) were not expected to give accurate quantitative results for comparison because of the simplicity of the model used, as discussed in §2. In particular, the model does not capture changes to the base flow caused by the introduction of the passive drag device. Because drag is in the opposite direction to the velocity, we plot $-\delta\sigma_r$ on the vertical axis.

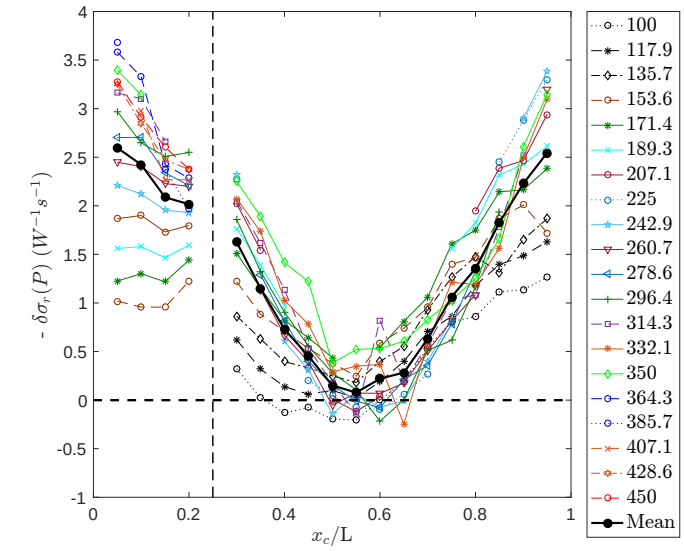

(a)

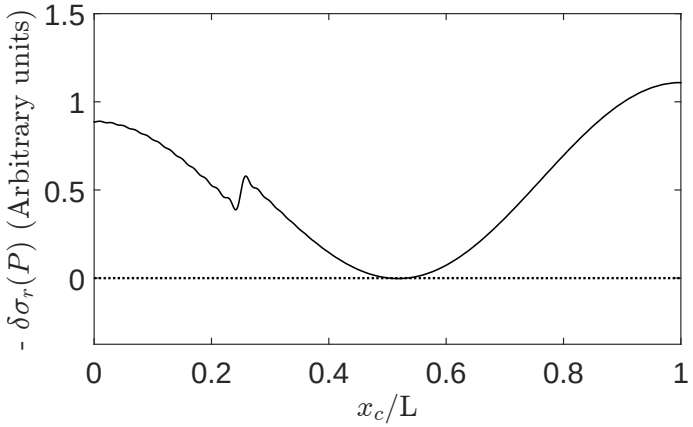

(b)

Fig. 3.8 Sensitivity of the linear growth rate to a passive drag device. (a) Experimental results and (b) theoretical predictions by Magri and Juniper (2013c) in arbitrary units. The legend for (a) shows the different primary heater powers which were examined. The units for all legend entries are Watts. The average sensitivity is also given as a visual aid to show the general qualitative behaviour.

3.4.3 Shift in oscillation frequency

The shift in oscillation frequency in the presence of the passive drag device was also measured and is shown in figure 3.9b. Magri and Juniper (2013c) predict that the frequency shift should be two orders of magnitude smaller than the linear growth rate shift (figure 2.1, §2.3.1) and here we measure it to be of the same order. In the experiment a non-negligible increase of the mean air temperature downstream of the heater was observed. This was due to the heat transfer between the heater and the mean flow through the Rijke tube. The increased temperature is mainly due to the increased critical power required for the transition of the system, $P_{crit,c}$, when the control device is introduced, as seen in figure 3.10. Magri and Juniper (2013c) examined the sensitivity of the system to changes in the heat release rate parameter, which in the experimental set-up can be linked to the power supplied to the heater. They found that a variation in the heat release rate parameter, here P_{crit}, has a much greater effect on the frequency than on the linear growth rate.

The mean temperature deviation due to the increase of P_{crit}, which is not captured in the Magri and Juniper (2013c) model, changes the speed of sound and the frequency of the thermoacoustic oscillation. If the mean air temperature is assumed to be the outlet air temperature, which was measured during the experiments, then an estimate of the expected frequency of the fundamental (1/2 wavelength) mode is approximately given by:

$$f = \left[\frac{2(L_u + 0.61D)}{c_u} + \frac{2(L_d + 0.61D)}{c_d} \right]^{-1} \tag{3.3}$$

where L_u and c_u are the tube length and local speed of sound upstream of the primary heater, L_d and c_d are the tube length and local speed of sound downstream of the primary heater, and $0.61D$ is the end correction where D is the diameter of the Rijke tube (Rienstra and Hirschberg, 2006). The main assumptions that

were made in this approximation were that (i) the total frequency could be approximated by summing the upstream and downstream frequencies estimated for the fundamental mode, $f = (2L/c)^{-1}$; (ii) the upstream local speed of sound, c_u, could be determined from the measured ambient temperature, assuming the mean temperature of the flow upstream of the primary heater was similar to the measured ambient temperature; and (iii) the downstream local speed of sound, c_d, could be determined from the measured outlet flow temperature, assuming that the mean flow temperature downstream of the primary heater was similar to the measured outlet flow temperature. Whilst this was a very approximate calculation of the frequency, the aim was to see whether the change in measured outlet temperature could account for the observed experimental results. The comparison (figure 3.10a) shows that both the empirically calculated frequency and the measured frequency are similar in magnitude and depict the same features. Each experimental curve in figure 3.10a corresponds to a different heater power, P, which is shown in the legend. It can be seen in figure 3.10a, that as P is increased, the measured shift in frequency observed during periods of linear growth and decay decreases. This was a good indication that the modelling of the base flow of the system is essential and therefore demonstrates that the model needs to be updated to include base flow changes induced by the introduction of a passive drag device. It also indicates that the shift in oscillation frequency due to the changes in the mean conditions greatly exceeds the expected frequency shift due to feedback from the passive drag device. It can therefore be inferred that the expected frequency shift due to feedback from the passive drag device was much smaller than the frequency shift due to the change in the mean flow.

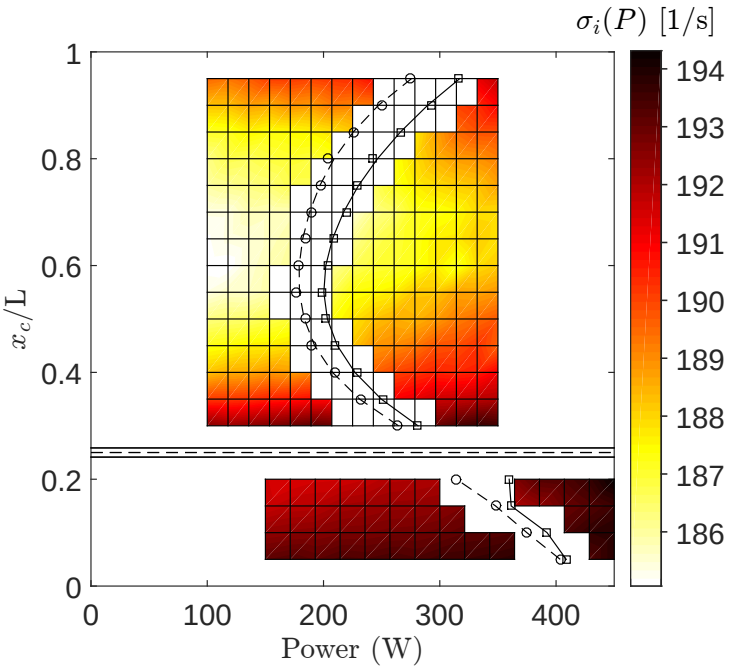

(a)

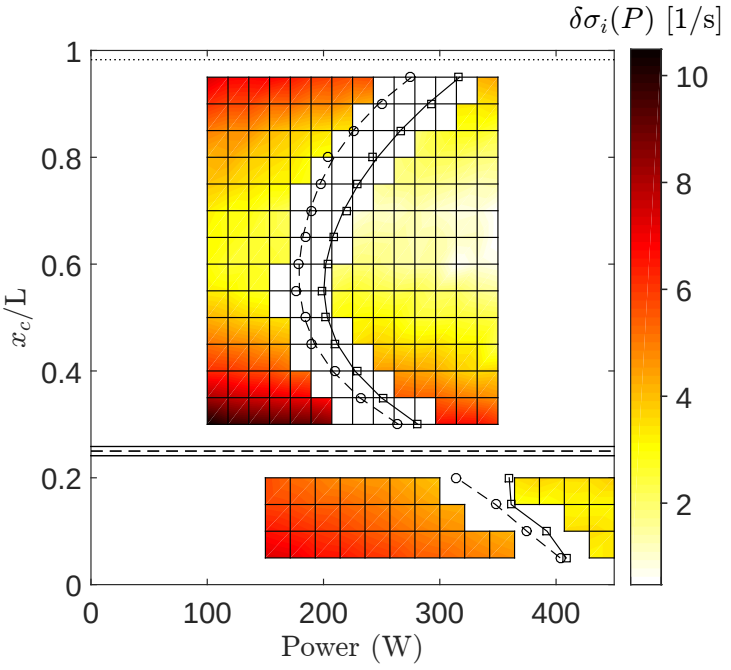

(b)

Fig. 3.9 (a) Oscillation frequency and (b) shift in oscillation frequency, experimentally obtained, as a function of power supplied to the heater and position of the passive drag device. Forward path critical powers (squares) and backward path critical powers (circles).

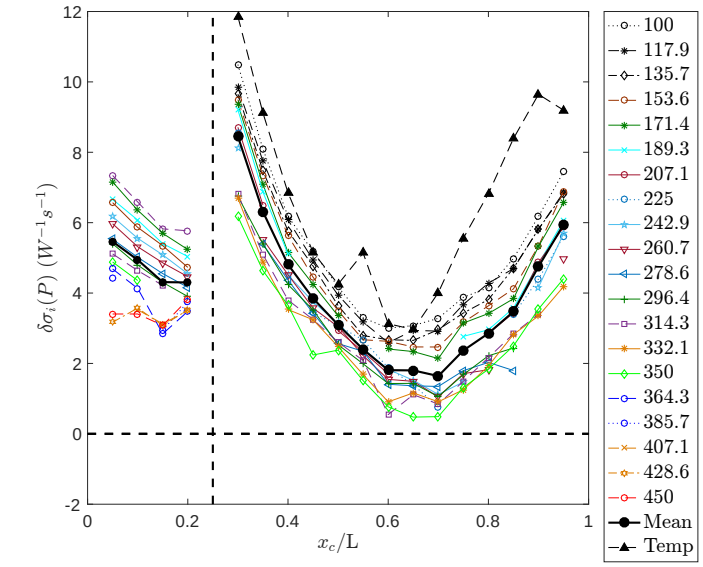

(a)

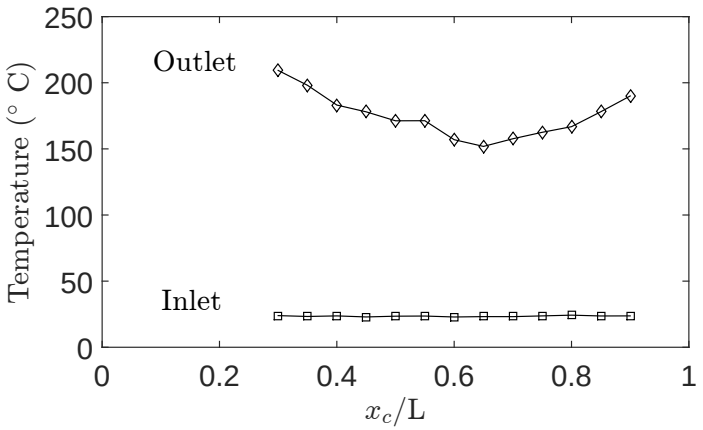

(b)

Fig. 3.10 (a) Sensitivity of the oscillation frequency to a passive drag device. The legend for (a) shows the different primary heater powers which were examined. The units for all legend entries, except for "Temp", are Watts. The average sensitivity is also given as a visual aid to show the general qualitative behaviour. An estimate of the oscillation frequency change due to variations in the outlet temperature shown in (b).

3.5 Concluding remarks

This chapter has shown that experimental sensitivity analysis can be performed on a vertical Rijke tube to determine how sensitive the linear growth rates and oscillation frequencies are to passive feedback control in the form of a passive drag device. The shift in linear growth rates, linear decay rates and oscillation frequency during periods of linear growth and decay are experimentally obtained and compared with the theoretical predictions of Magri and Juniper (2013c).

Chapter 4

Sensitivity analysis and control via a secondary heat source

This chapter has been published as a journal paper in Jamieson et al. (2016). All experiments were completed by the author, the post-processing was completed by the author and the automation procedure was conceived in equal parts with Georgios Rigas and implemented in National Instruments LabVIEW by Georgios Rigas.

4.1 Introduction

In this chapter, we investigate the control of an electrically-heated Rijke tube via a secondary heat source placed downstream of the primary heat source with a constant power input. We use the techniques developed in chapter 3 to ascertain the effect that a secondary heat source has when introduced to our thermoacoustic system.

In this chapter we carefully measure and compare experimental results with theoretical predictions from adjoint-based sensitivity analysis. We also build upon the work discussed in chapter 3 by performing an uncertainty analysis to quantify the random error in the measurements. The findings suggest that adjoint-based methods could provide industry with a valuable tool for developing optimal control strategies for more complex thermoacoustic systems.

4.2 Experimental set-up

Experiments were conducted on a 1 m long stainless steel vertical Rijke tube with an internal diameter of 47.4 mm and a wall thickness of 1.7 mm. The primary heater was attached to two rods and held in place at $x_p/L = 0.25$, the optimal position for exciting thermoacoustic oscillations (Saito, 1965). It was powered by a 640 Watt EA Elektro-Automatik EA-PSI 5080-20 A DC programmable power supply. The secondary heat source was used as a passive drag device with no power input for the first experiment and with a power input for the second experiment. The control device was attached to an automated digital height gauge at the top of the Rijke tube, enabling it to be traversed with an accuracy of $\pm$ 0.01 mm. Both the primary heater and the secondary heat source are shown in appendix A

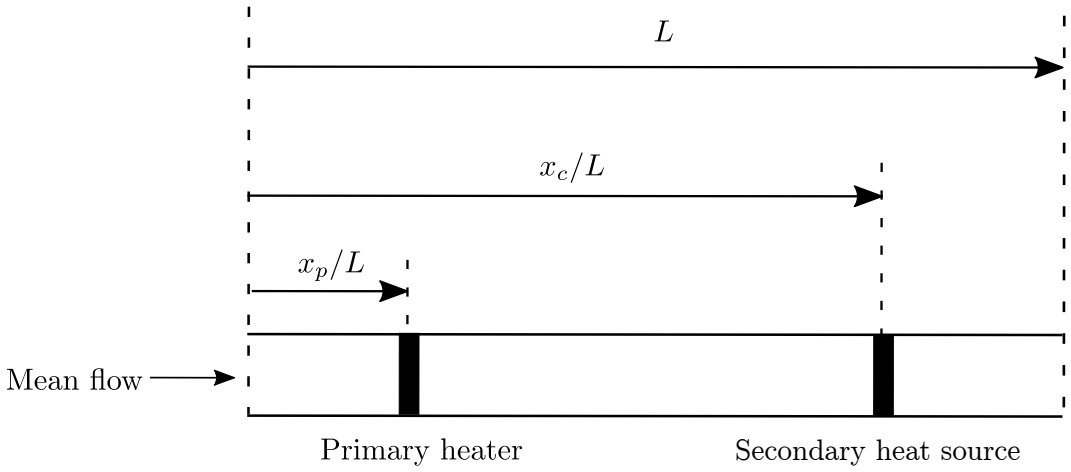

Fig. 4.1 Schematic of experimental set-up.

A Brüel Kjaer condenser type 2619 microphone with a sensitivity of 11.4 mV Pa^{-1} was used to measure pressure fluctuations. The microphone was angled at 45° and placed 55 mm from the bottom end of the tube. The raw pressure signal was sampled at 10 kHz, much higher than the anticipated frequencies of the thermoacoustic oscillations, approximately 190 Hz. Data was acquired via a National Instruments BNC-2110 DAQ device using LabVIEW. The set-up used is shown in figure 4.1.

4.3 Control via a secondary heat source

In this section, the control of an electrically-heated Rijke tube via the introduction of a secondary heat source is investigated. The aim of this work was to extend the methods described in chapter 3 and carefully compare experimental results with the theoretical predictions of adjoint-based methods.

4.3.1 Methodology

Experiments were performed for a range of operating points (figure 4.2). The experimental procedure comprised of three steps: (i) the system was heated up

to a steady state with a primary heater power input of ≈ 138 W, (ii) the power input to the primary heater was then abruptly increased to ≈ 393 W, and the linear growth rate was measured as the system transitioned from a stable fixed point to a stable limit cycle, and (iii) the power input to the primary heater was then abruptly decreased to ≈ 138 W, and the linear decay rate was measured as the system transitioned from a stable limit cycle to a stable fixed point.

For each of the above steps, the secondary heat source was held at a constant power. The secondary heat source was then given a range of predetermined power inputs, seen as the corresponding x-axis power for a given acquisition point "×" in figure 4.2.

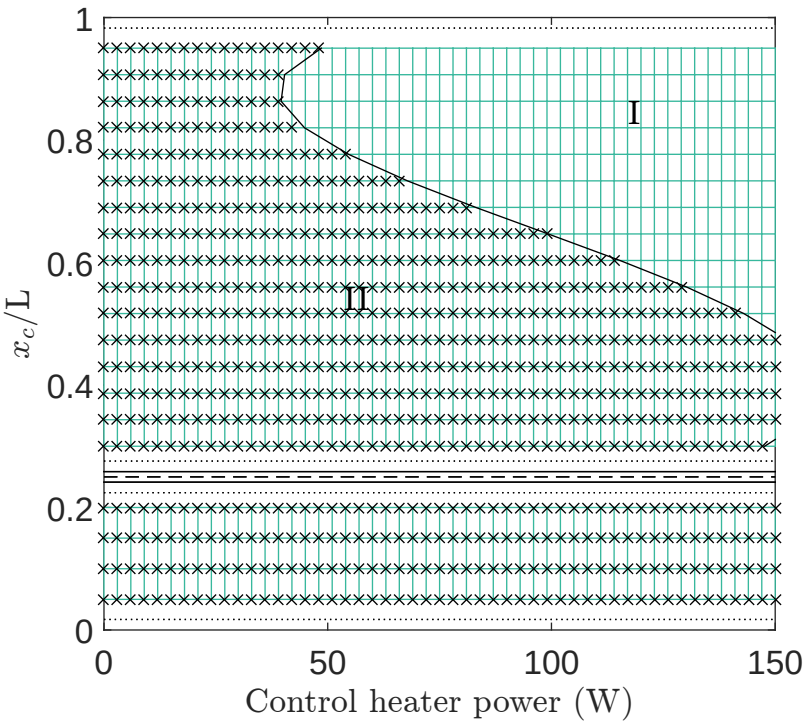

Fig. 4.2 Experimental operating range. "×" mark a point where a linear growth rate, linear decay rate and oscillation frequency measurement was acquired. Dashed lines at $x_c/L = 0.25$ indicate the location of the primary heater. The experiment was repeated five times at each data point.

The secondary heat source was traversed from $x_c/L = 0.05$ to 0.2 and 0.3 to 0.95 in 0.05 increments. At each examined location, the acquisition process was

repeated three times with no power input to the secondary heat source to obtain a baseline growth rate, $\sigma_{0,r,g}$, decay rate, $\sigma_{0,r,d}$, frequency during the period of linear growth, $\sigma_{0,i,g}$, and the frequency during the period of linear decay, $\sigma_{0,i,d}$.

At locations $x_c/L = 0.55$ to 0.95, the range of examined secondary heat source powers was reduced. Above the critical power denoted by the line separating the unstable and stable sections of the figure 4.2, the abrupt step in primary heater power did not cause the system to transition from a stable fixed point to a stable limit cycle. A higher power input may have transitioned the system, but we were restricted by the maximum power of the secondary power supply.

The novelty in the experimental set-up is that the entire process was automated. We were able to acquire every data point exhibited in figure 4.2 in approximately 42 hours of testing. To ensure repeatability of results, the experiment was repeated five times such that a detailed uncertainty analysis could be performed (appendix B).

The shift in linear growth rate and decay rate defined in the theoretical analysis of Magri and Juniper (2013c) is obtained experimentally as:

$$\begin{aligned}\delta\sigma_{r,g}(P_c, x_c, P_p) = \sigma_{r,c}(P_c, x_c, P_{p,2})... \\ -\sigma_{r,0}(x_c, P_{p,2}).\end{aligned} \tag{4.1}$$

$$\begin{aligned}\delta\sigma_{r,d}(P_c, x_c, P_p) = \sigma_{r,c}(P_c, x_c, P_{p,1})... \\ -\sigma_{r,0}(x_c, P_{p,1}).\end{aligned} \tag{4.2}$$

where $P_{p,2}$ is the power to the primary heater when the system was at a stable limit-cycle, and $P_{p,1}$ is the power to the primary heater when the system was at a stable fixed point. The subscript c corresponds to the control case (heater

on) and the subscript 0 to the baseline case (heater off). The data for linear growth rates, decay rates and frequency during periods of growth and decay were obtained via the same acquisition and data processing methods as discussed in chapter 3. For brevity, these methods are not reiterated in this chapter.

4.3.2 Measurement of linear growth and decay rates

The linear growth and decay rates were measured experimentally for a range of secondary heat source powers, P_2, and secondary heat source axial locations, x_c/L.

To determine the shift in linear growth rates and linear decay rates due to the presence of a secondary heat source the data obtained at each location was processed in exactly the same way. For brevity, the data for only $x_c/L = 0.35$ and $x_c/L = 0.55$ are presented here, see figure 4.3 and figure 4.4.

Figure 4.3a shows the growth rates (blue) and decay rates (red) obtained over the course of the five repeated experiments at $x_c/L = 0.35$. The baseline growth rates and baseline decay rates are plotted in the dashed green lines. Each green line corresponds to a baseline obtained for data taken on a particular day. Figure 4.4a shows the same but for $x_c/L = 0.55$. The reason the baseline measurement changes between days is most likely due to ambient temperature and humidity changes in the laboratory. The Rijke tube operated at temperatures of approximately 100 - 380°C and ambient air temperature and humidity changed by approximately 8°C and 5%, respectively, over the course of a day.

Figure 4.3b shows the difference between the linear growth rate obtained with the secondary heat source on, $\sigma_{c,r,g}$, and the baseline linear growth rate, $\sigma_{0,r,g}$, at $x_c/L = 0.35$. The data obtained over the five experiments was averaged and the mean was plotted. To extract the shift in linear growth rate, a least-squares regression fitting was constructed between 0 W and 50 W, the region where the

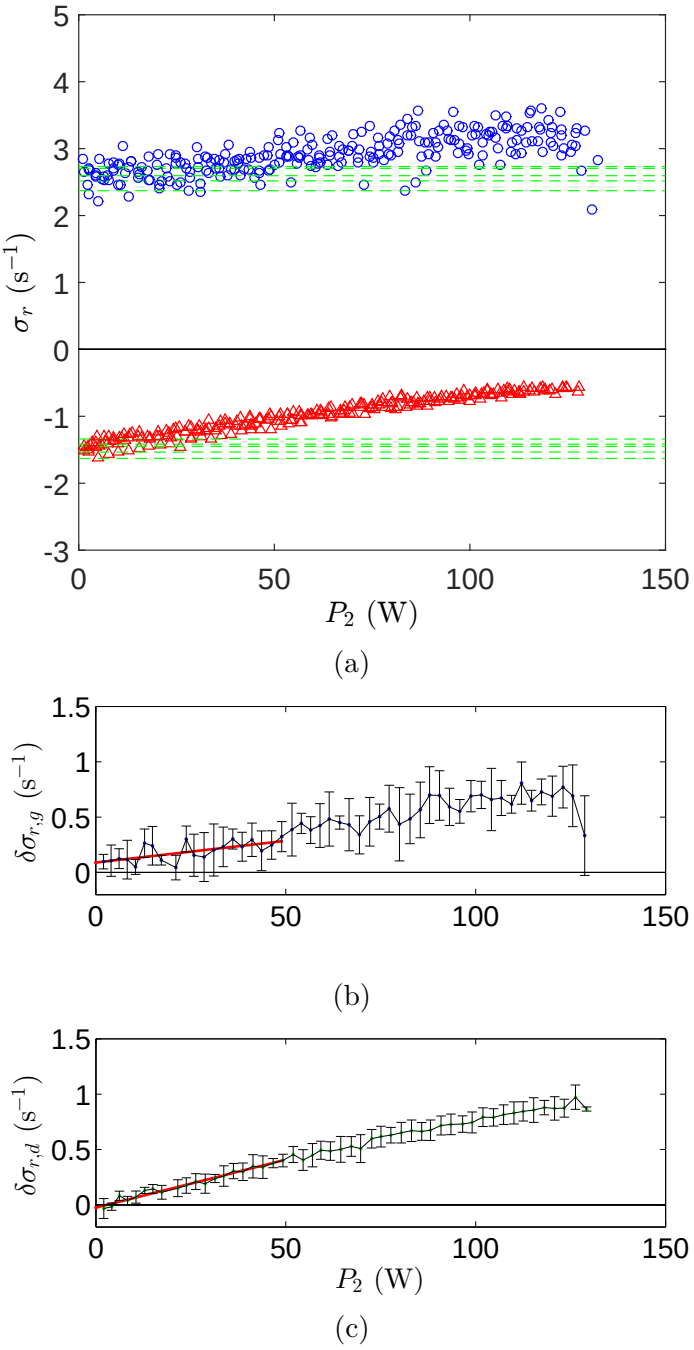

Fig. 4.3 (a) $x_c/L = 0.35$: Linear growth rates (blue) and linear decay rates (red) obtained for a range of secondary heat source powers. All baseline runs are shown in green; (b) $x_c/L = 0.35$: difference between growth rate with the secondary heat source and the baseline linear growth rate, $\delta\sigma_{r,g}$; (c) $x_c/L = 0.35$: difference between linear decay rate with the secondary heat source and the baseline decay rate, $\delta\sigma_{r,d}$.

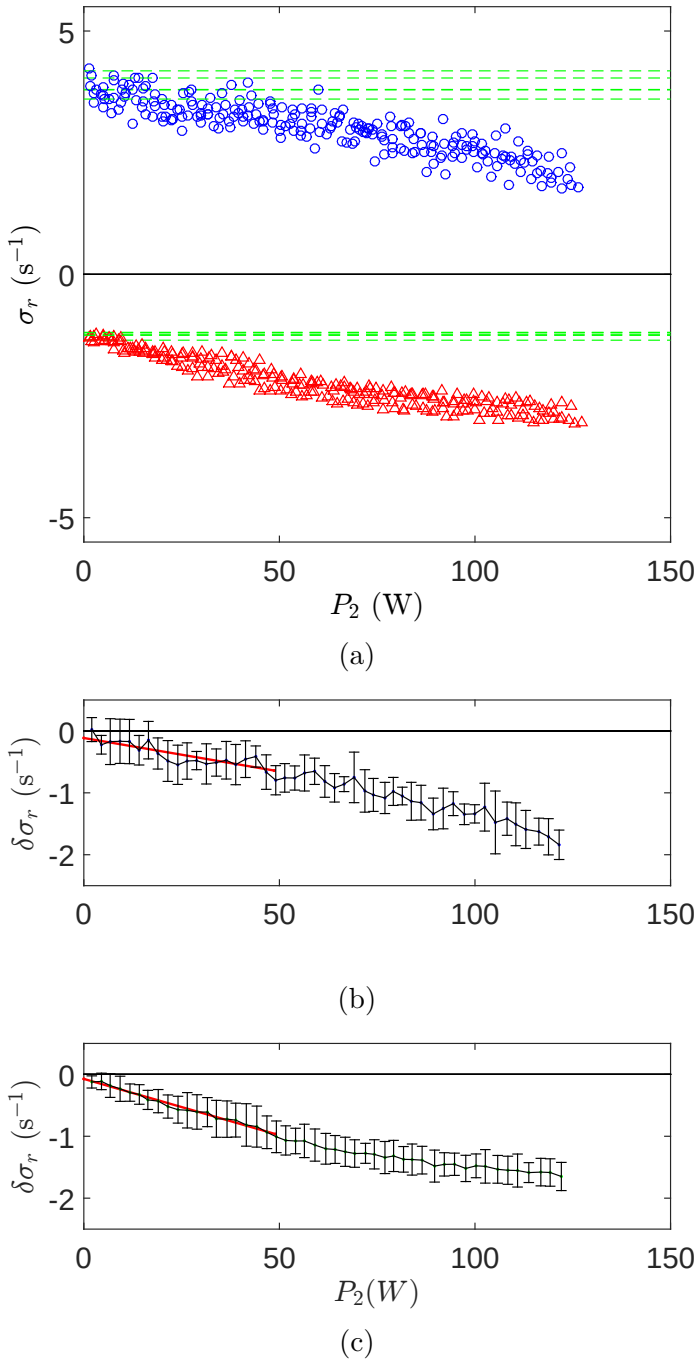

Fig. 4.4 (a) $x_c/L = 0.55$: Linear growth rates (blue) and linear decay rates (red) obtained for a range of secondary heat source powers. All baseline run is shown in green; (b) $x_c/L = 0.55$: difference between linear growth rate with the secondary heat source and the baseline linear growth rate, $\delta\sigma_{r,g}$; (c) $x_c/L = 0.55$: difference between linear decay rate with the secondary heat source and the baseline linear decay rate, $\delta\sigma_{r,d}$.

shift in growth rate was deemed to be linear. Figure 4.3c shows the difference between the linear decay rate obtained with the secondary heat source on, $\sigma_{c,r,d}$, and the baseline linear decay rate, $\sigma_{0,r,d}$. Figure 4.4b and 4.4c show the same for $x_c/L = 0.55$. Error bars are presented for each data point in figure 4.3b, 4.3c, 4.4b and 4.4c. The uncertainty analysis is discussed in appendix B.

It can be seen that the gradient of the data in figure 4.3a, 4.3b and 4.3c is positive, whilst the gradient of the data in figure 4.4a, 4.4b and 4.4c is negative. This demonstrates that the presence of the secondary heat source has a destabilising effect in the bottom half of the tube, $x_c/L = 0.35$, and a stabilising effect when placed in the top half of the tube, $x_c/L = 0.55$. This is a well known qualitative result. Our results quantify the degree of stabilization and can be compared with the predictions of Magri and Juniper (2013c).

4.3.3 Measurement of frequency during linear growth and decay of oscillations

The frequency during the linear growth and decay of the thermoacoustic oscillations were obtained for a variety of secondary heat source powers, P_2, and secondary heat source axial locations. Data was obtained over the same operating range as the linear growth and decay rate measurements.

To determine the shift in the frequency during the period of linear growth and decay of the oscillations due to a secondary heat source, the data was processed at each axial location in the exact same way. For brevity, only the data for $x_c/L = 0.35$ and $x_c/L = 0.55$ are presented here, see figure 4.5 and figure 4.6.

Figure 4.5a shows the frequency during the linear growth of the oscillations (blue) and the frequency during the linear decay of the oscillations (red). The baseline frequencies exhibited during these periods are denoted by the green

dashed line. Each baseline frequency measurement corresponds to the data taken on a particular day.

Figure 4.5b shows the difference between the frequency during the linear growth of the oscillations obtained with a secondary heat source on, $\sigma_{c,i,g}$, and the baseline frequency during the linear growth of oscillations, $\sigma_{0,i,g}$. The data obtained over the five experiments is averaged and the mean is plotted. To extract the shift in frequency during the period of linear growth of oscillations, a least-squares regression fitting was constructed between 0 W and 50 W, the region where the shift in frequency during the growth of oscillations was deemed to be linear. Figure 4.5c shows the difference between the frequency during the linear decay of the oscillations obtained with a secondary heat source on, $\sigma_{c,i,d}$, and the baseline frequency during the linear decay of oscillations, $\sigma_{0,i,d}$. The data obtained over the five experiments is averaged and the result is plotted. Figure 4.6b and 4.6c show the same for $x_c/L = 0.55$. Error bars are presented for each data point in figure 4.5b, 4.5c, 4.6b and 4.6c. The uncertainty analysis is discussed in appendix B.

It can be seen that the gradient of the data in each subplot of figure 4.5 and 4.6 is positive. For the frequency measurements, this was expected because by increasing the secondary heat source power we were always increasing the temperature of the mean flow in the Rijke tube. As the flow temperature increases, the local speed of sound will also increase resulting in a positive increase in frequency of oscillation (Rigas et al., 2015).

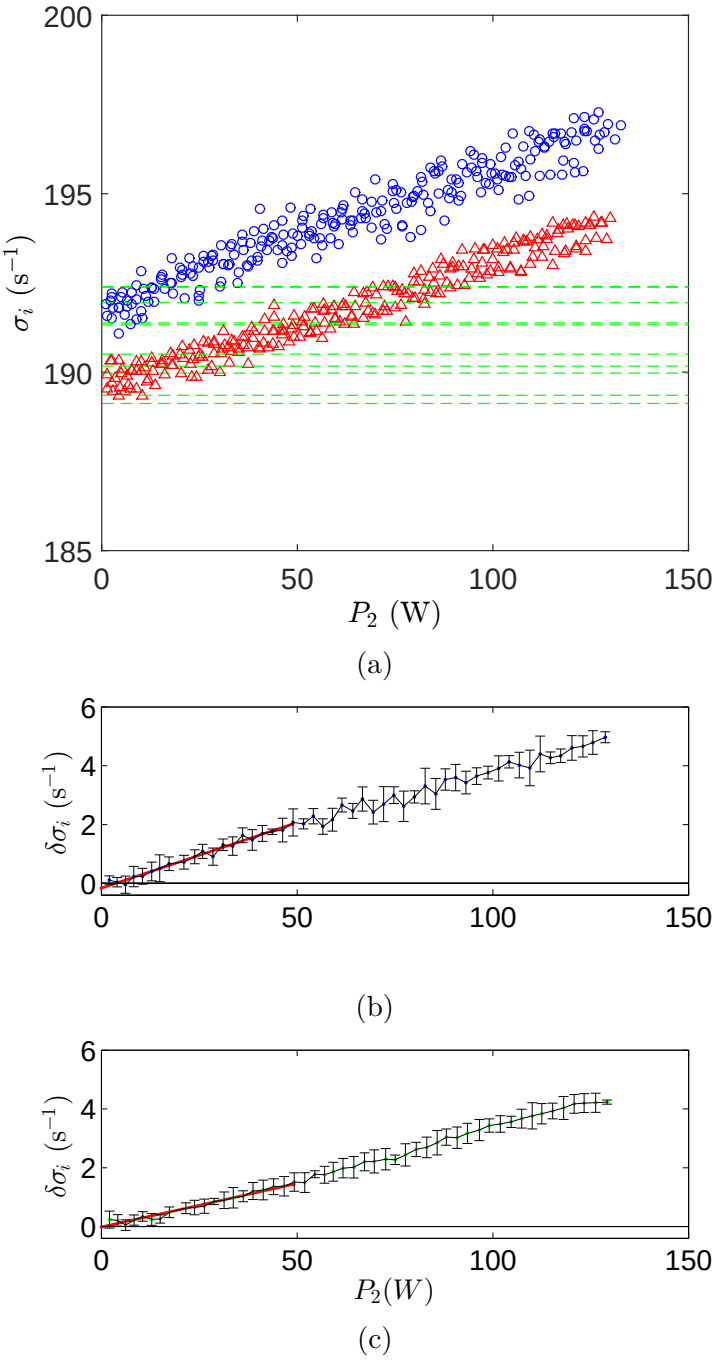

Fig. 4.5 (a) $x_c/L = 0.35$: Frequency during period of growth (blue) and decay (red) of oscillations obtained for a range of secondary heat source powers. All baseline runs are shown in the green; (b) $x_c/L = 0.35$: oscillation frequency during period of linear growth with and without the secondary heat source, $\delta\sigma_{i,g}$; (c) $x_c/L = 0.35$: oscillation frequency during period of linear decay with and without the secondary heat source, $\delta\sigma_{i,d}$.

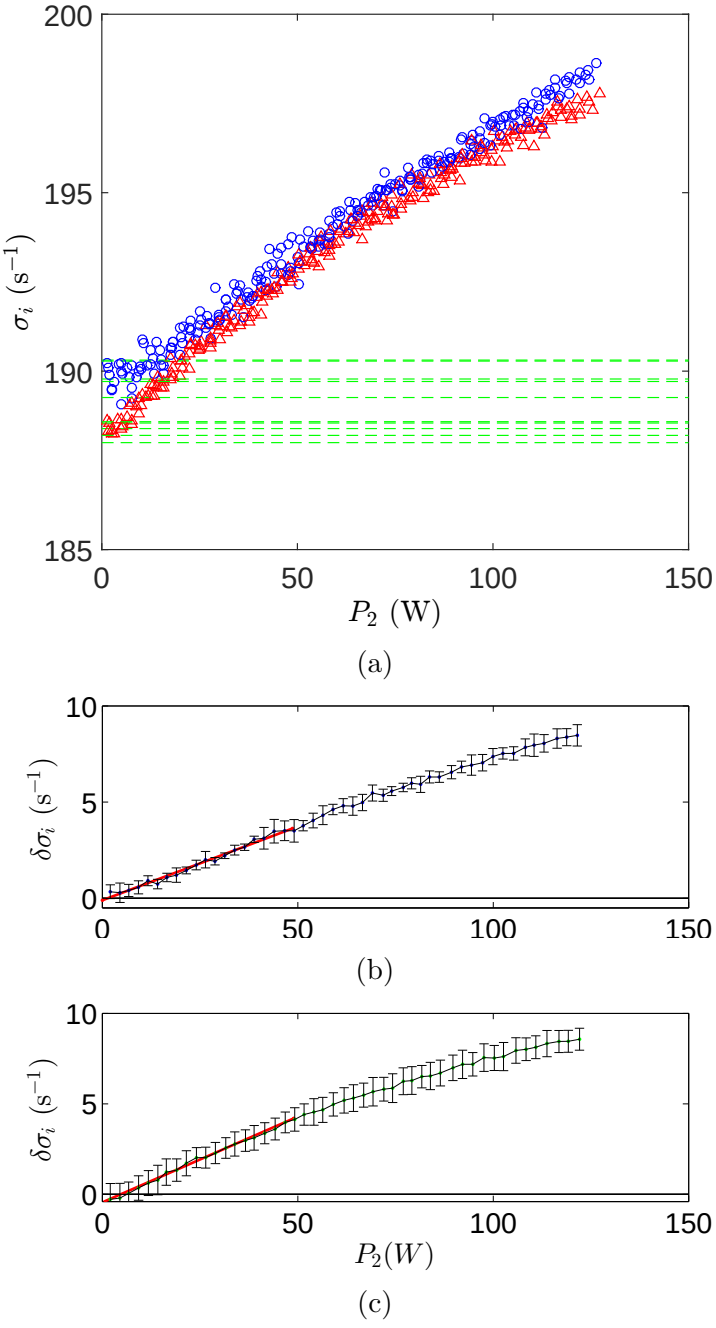

Fig. 4.6 (a) $x_c/L = 0.55$: Frequency during period of growth (blue) and decay (red) of oscillations obtained for a range of secondary heat source powers. All baseline runs are shown in the green; (b) $x_c/L = 0.55$: oscillation frequency during period of linear growth with and without the secondary heat source, $\delta\sigma_{ri,g}$; (c) $x_c/L = 0.55$: oscillation frequency during period of linear decay with and without the secondary heat source, $\delta\sigma_{i,d}$.

4.4 Sensitivity analysis

4.4.1 Shift in linear growth and decay rate

This section presents the experimental sensitivity analysis results detailing the shift in linear growth and decay rate due to the introduction of a secondary heat source.

Figure 4.8a and 4.8b show $\delta\sigma_{r,g}$ and $\delta\sigma_{r,d}$ for x_c/L = 0.1, 0.15, 0.35, 0.45, 0.55, 0.75, and 0.85. These points were chosen so that a clear depiction could be obtained of how the gradient of the $\delta\sigma_{r,g}$ and $\delta\sigma_{r,d}$ data varies as the secondary heat source was traversed through a range of axial locations. The coloured patching around the mean $\delta\sigma_{r,g}$ and $\delta\sigma_{r,d}$ represents the uncertainty in the measurement at that axial location. It can be seen that at axial locations x_c/L = 0.75 and 0.85, the uncertainty is larger. The reason for this was that we had fewer data points when compared with other axial locations.

Figure 4.9a presents the experimental sensitivity analysis results for the shift in linear growth rate (blue) and linear decay rate (red) due to the introduction of secondary heat source. We compare the experimental results with the predictions of Magri and Juniper (2013c) (figure 4.9b) and find that they qualitatively compare well. It can be seen in figure 4.9a that the introduction of a secondary heat source had a destabilising effect when placed between $x_c/L = 0.05$ and $x_c/L = 0.4$. Magri and Juniper (2013c) found that this was because when the secondary heat source was placed between $x_c/L = 0.05$ and $x_c/L = 0.4$, the acoustic pressure and unsteady heat release rate are sufficiently in phase, making a positive contribution to the growth of oscillation over a cycle. When the secondary heat source is placed between $x_c/L = 0.45$ and $x_c/L = 0.95$, figure 4.9a shows that it has a stabilising effect on the system. This is because in this region, the acoustic pressure and unsteady heat release rate are out of phase

such that they negatively contribute to the growth of oscillations over a cycle (Magri and Juniper, 2013c).

To explain the physical mechanism it is convenient to recall that (i) the fundamental acoustic mode has a pressure node at either end of the tube and an antinode at the midpoint; and that (ii) the acoustic velocity has a node at the centre and an antinode at either end. During the compression phase of the acoustic cycle, the acoustic velocity is directed towards the centre of the tube, causing the pressure in the tube to increase. When the heater is placed in the upstream half of the tube, the acoustic velocity and the mean velocity are in the same direction during the compression phase. This causes the air speed around the heater, and therefore the heat transfer to be larger than average during the compression phase. Critically, there is also a time delay (Lighthill, 1954) between the velocity at the heater and the subsequent heat release rate. These two properties mean that, over an acoustic cycle, more heat release occurs during moments of higher pressure than occurs during moments of lower pressure, causing more mechanical work to be done by the gas expanding during the expansion phase than is needed to compress it during the compression phase (Rayleigh, 1878). This results in the amplitude of acoustic oscillations growing until the heat release rate perturbations saturate and the excess work is balanced through acoustic radiation, viscous losses and thermal losses. When the heater is placed in the downstream half of the tube the opposite is true, resulting in the heater having a stabilising effect on the system.

Mathematically, the physical description given above can be demonstrated by considering the Rayleigh criterion (Rayleigh, 1878) and using simple expressions from Lieuwen (2012) and Carvalho et al. (1989). Particularly, by plotting the Rayleigh index for an open-open tube one can determine the regions of the flow field that contribute most to the Rayleigh criterion, thus encouraging ($I > 0$) or

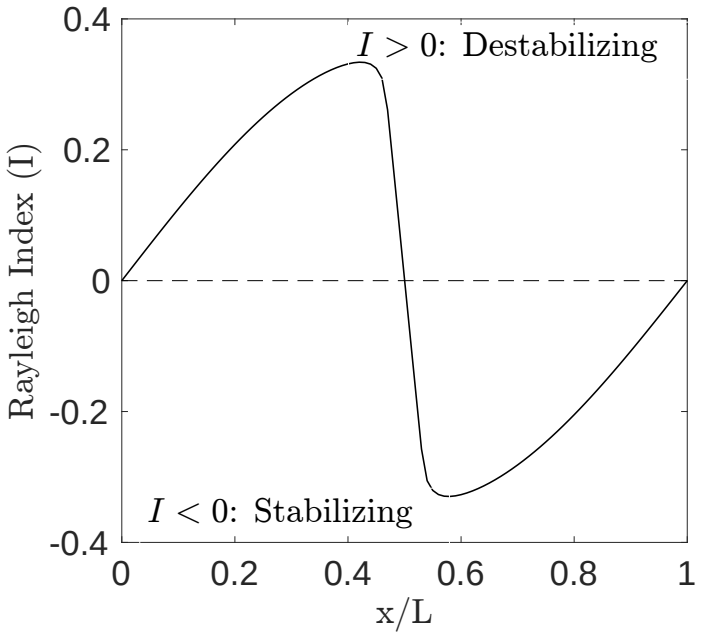

Fig. 4.7 Rayleigh index showing at which locations the heater encourages and discourages thermoacoustic oscillations. $A = 0.5$, $a = 1$, $K = 1$, $L = 1$ m, $c = 343$ m/s, $\bar{u} = 0.1$ m/s, and $\tau = 0.001$ s.

discouraging ($I < 0$) thermoacoustic oscillations:

$$I = \oint p' \dot{q} \, dt \tag{4.3}$$

where p' and u' are derived in Lieuwen (2012) to be:

$$p' = 2A \sin\left(\frac{n\pi x}{L}\right) \sin\left(\frac{n\pi c}{L} t\right) \tag{4.4}$$

$$u' = 2A \cos\left(\frac{n\pi x}{L}\right) \cos\left(\frac{n\pi c}{L}(t - \tau)\right) \tag{4.5}$$

and $\dot{q}$ is from Carvalho et al. (1989):

$$\dot{q} = K + a|\bar{u} + u'| \tag{4.6}$$

In equations 4.4, 4.5 and 4.6: A, a, and K are arbitrary constants, n is the mode, x is the axial location of the heater, L is the length of the tube, c is the speed of sound, t is time, $\bar{u}$ is the mean flow velocity and τ is the time delay. Substituting equation 4.4, 4.5 and 4.6 into equation 4.3 gives:

$$I = \oint \left[K + a \left| \bar{u} + 2A \cos\left(\frac{n\pi x}{L}\right) \cos\left(\frac{n\pi c}{L}(t-\tau)\right) \right| \right] ... \left[2A \sin\left(\frac{n\pi x}{L}\right) \sin\left(\frac{n\pi c}{L} t\right) \right] dt \tag{4.7}$$

Integrating equation 4.7 over one period and plotting I against x/L demonstrates the regions of the flow field that encourage and discourage thermoacoustic oscillations (figure 4.7).

In accordance with the description above, figure 4.7 shows that in the upstream half of the tube, $I > 0$, indicating p' and $\dot{q}$ are sufficiently in phase so that thermoacoustic oscillations are encouraged. Whilst in the downstream half of the tube, $I < 0$, indicating that p' and $\dot{q}$ are sufficiently out of phase so that thermoacoustic oscillations are discouraged. This result compares well to the results presented in figure 4.9. It should be noted, however, that the values used in equation 4.7 do not represent the thermoacoustic system discussed in this chapter and were chosen so that a simple model based on Lieuwen (2012) and Carvalho et al. (1989) could be used to aid in the physical description above of why a secondary heat source could suppress thermoacoustic oscillations.

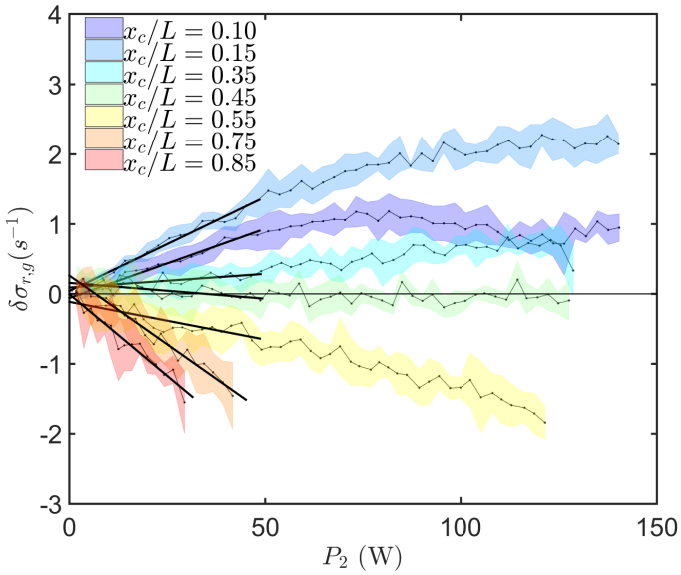

(a)

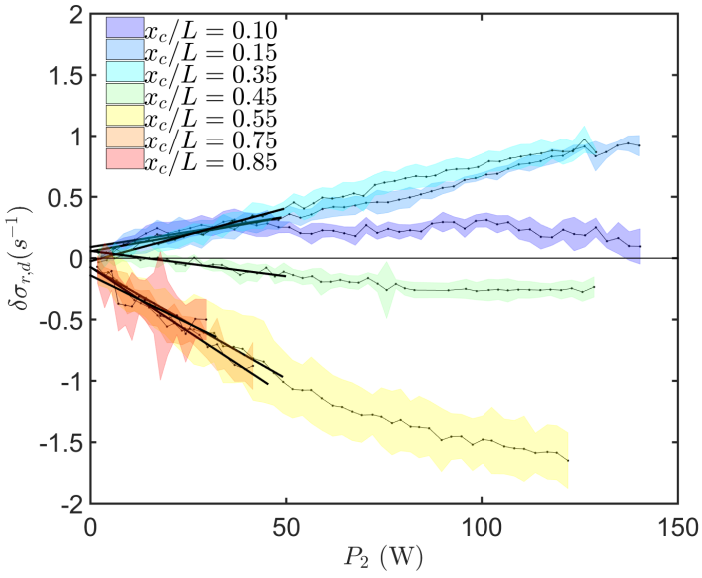

(b)

Fig. 4.8 (a) Range of $\delta\sigma_{r,g}$ with the color patch outlining the uncertainty; (b) Range of $\delta\sigma_{r,d}$ with the color patch outlining the uncertainty.

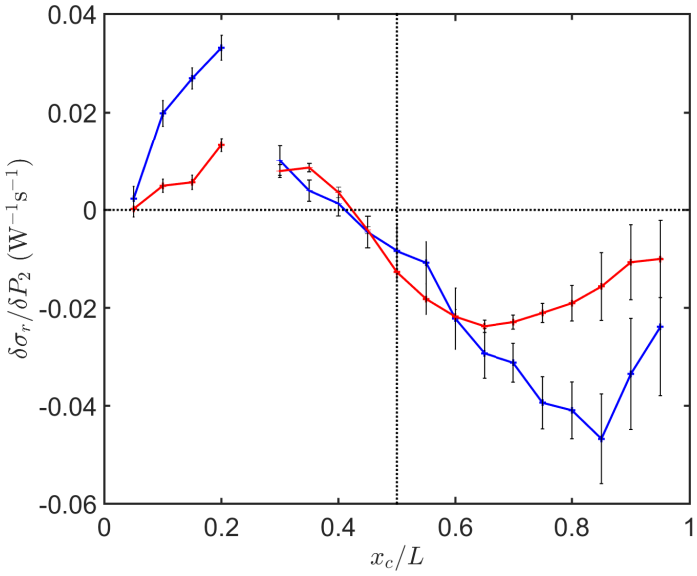

(a)

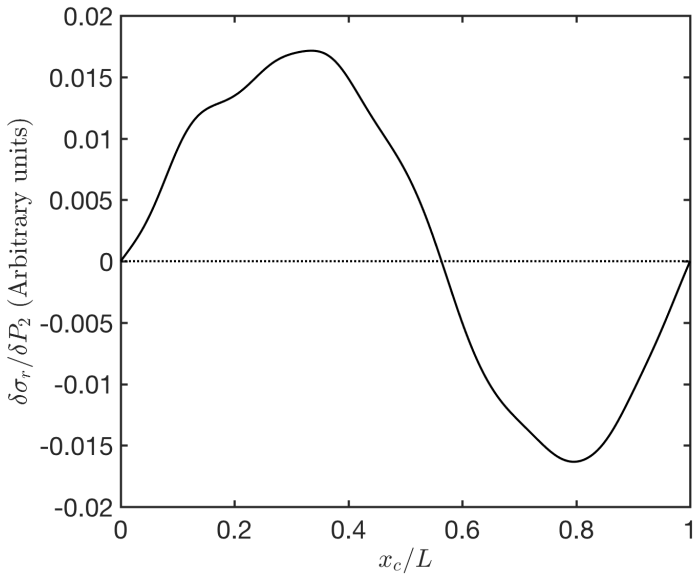

(b)

Fig. 4.9 (a) The shift in linear growth rate (blue) and linear decay rate (red) due to a secondary heat source; (b) The adjoint-based predicted shift in linear growth rate due to a secondary heat source (Magri and Juniper, 2013c).

We find that when placed at $x_c/L = 0.85$, the secondary heat source is most successful at stabilising the growth of thermoacoustic oscillations. It can be seen in figure 4.9a that both the shift in linear growth rate and the shift in linear decay rate exhibit the same qualitative trends. However, both sets of data do not overlay perfectly. We believe this to be due to changes in the base state of the system. In comparing the experimental results with the results from adjoint-based sensitivity analysis (figure 4.9), it is clear that the theoretical results predict the main features of the physical observations. The results of Magri and Juniper (2013c) were not expected to give accurate quantitative results for comparison because of the simplicity of the model used, as discussed in §2. In particular, the model does not capture changes to the base flow caused by the introduction of a secondary heat source. This base-state sensitivity analysis is the subject of current work by the Energy Group at the Cambridge University Engineering Department. Error bars are presented with the experimental data in figure 4.9a to indicate random error and are discussed in appendix B.

4.4.2 Shift in frequency during linear growth and decay of oscillations

This section presents the experimental sensitivity analysis results detailing the shift in frequency during periods of linear growth and decay of the thermoacoustic oscillations.

Figure 4.10a and 4.10b show $\delta\sigma_{i,g}$ and $\delta\sigma_{i,d}$ for $x_c/L = 0.1$, 0.15, 0.35, 0.45, 0.55, 0.75, and 0.85. These points were chosen so that a clear depiction could be obtained of how the gradient of $\delta\sigma_{i,g}$ and $\delta\sigma_{i,d}$ data varies as the secondary heat source was traversed through a range of axial locations. The coloured patching around the mean $\delta\sigma_{i,g}$ and $\delta\sigma_{i,d}$ has the same meaning as above. Again, at

locations $x_c/L = 0.75$ and 0.85 the uncertainty is larger. This was because fewer experimental points were taken at these locations.

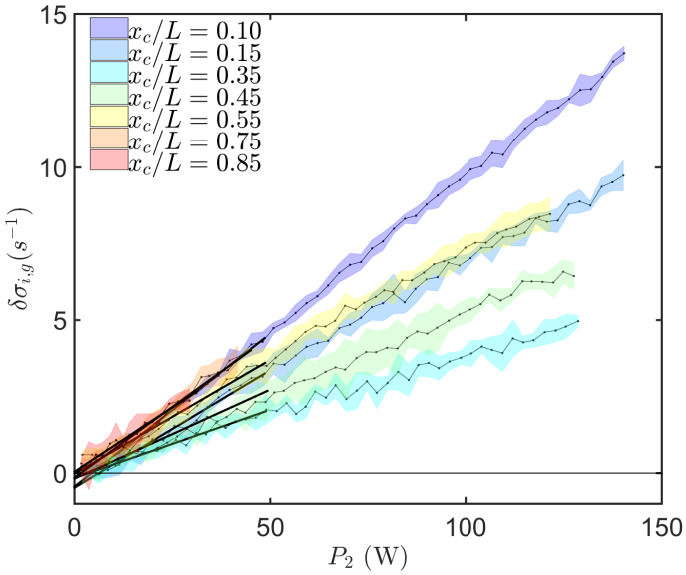

(a)

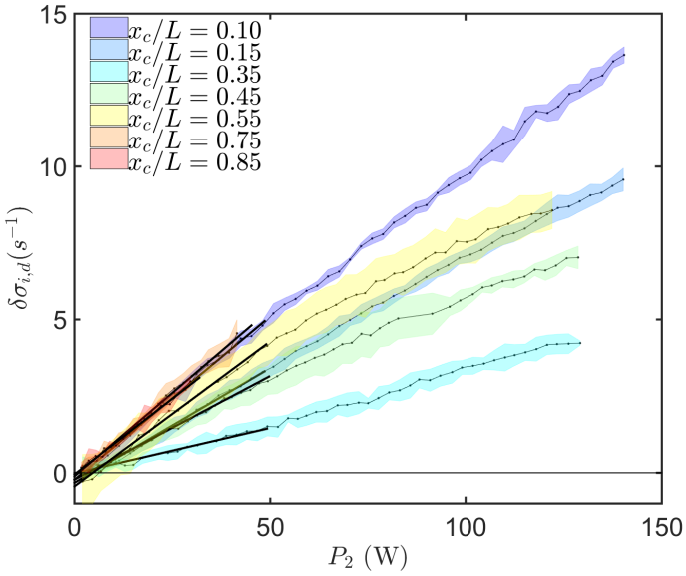

(b)

Fig. 4.10 (a) Range of $\delta\sigma_{i,g}$ with the color patch outlining the uncertainty; (b) Range of $\delta\sigma_{i,d}$ with the color patch outlining the uncertainty.

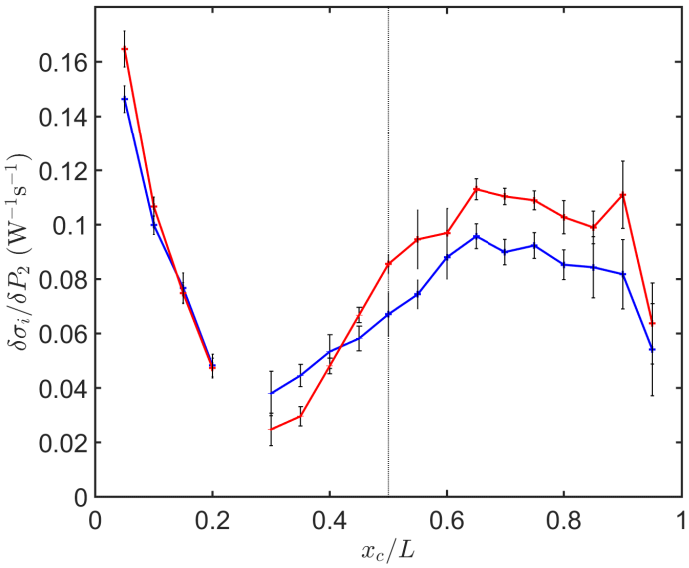

(a)

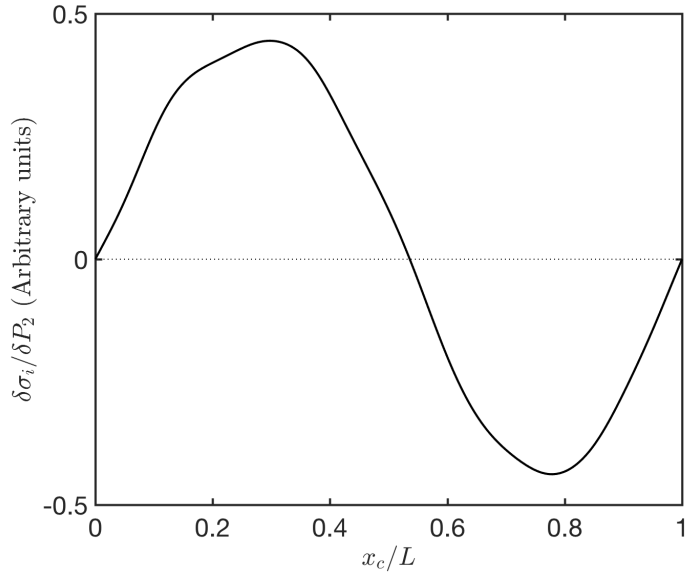

(b)

Fig. 4.11 (a) The shift in oscillation frequency during linear growth (blue) and linear decay (red) due to a secondary heat source; (b) The adjoint-based predicted shift in oscillation frequency during periods of linear growth due to a secondary heat source (Magri and Juniper, 2013c).

The shift in frequency during the periods of linear growth (blue) and decay (red), obtained via the experimental sensitivity analysis, are presented in figure 4.11a. We compare the experimental results with the predictions of Magri and

Juniper (2013c) (figure 4.11b) and find that they do not agree. We find that the experimental results are opposite in sign and shifted on the y-axis when compared to the theoretical predictions made by adjoint-based sensitivity analysis. This result is counter intuitive. One would expect that when both the primary heater and the secondary heat source are located in the upstream half of the tube, the mean heat release rate that occurs in the upstream half of the tube would be higher than the mean heat release rate when the secondary heat source is located in the downstream half of the tube. The reason for why these counter intuitive physical observations occur are currently unknown.

Magri and Juniper (2013c) predict that the introduction of a secondary heat source will have a greater effect on the oscillation frequency shift than the linear growth and decay rate shift. This is manifested in the order of magnitude seen in figure 4.11b. When we compare the order of magnitude seen in figure 4.11a with that seen in figure 4.9a, we find that the secondary heat source does in fact have a greater effect on the shift in frequency during periods of linear growth and decay of oscillations than it does have on the shift in the linear growth and decay rate.

Whilst the experimental sensitivity analysis results for the shift in frequency during periods of growth and decay of oscillations do not match the adjoint-based predictions they are important to present. This discrepancy highlights the limitations of the model in capturing the physics pertaining to the frequency. Of particular relevance is the model's inability to capture changes in the base-state of the system due to the introduction of the secondary heat source. By developing a revised model which accounts for flow perturbations caused by the unsteady heat release rate and the drag induced by both the primary heater and the secondary heat source, it may be possible to get results from an adjoint-based sensitivity analysis that provide a better quantitative comparison to experimental results. The experimental results presented here will feed back into the development of a

revised model, taking into account the suggestions made throughout this thesis, to obtain a more accurate adjoint-based model of the system. This is further discussed in chapter 8.2.

4.5 Concluding remarks

This chapter has shown that sensitivity analysis can be performed experimentally on a vertical Rijke tube to determine how sensitive the linear growth rates, linear decay rates and oscillation frequency during periods of linear growth and decay are to the introduction of a secondary heat source. Experimental results were compared with the results of adjoint-based sensitivity analysis and a thorough uncertainty analysis was performed to reduce the random error of experimental measurements.

Chapter 5

Sensitivity analysis of a linearly stable thermoacoustic system via a pulsed forcing technique

This chapter was published as a journal paper in Jamieson and Juniper (2017b). All experiments and post-processing were completed by the author.

5.1 Introduction

In this chapter, the control of an electrically-driven, vertical Rijke tube was investigated via three methods; (i) a passive drag device, (ii) a secondary heat source, and (iii) a variable area outlet. Using a novel technique inspired by Mejia et al. (2016), the measurements in chapters 3 and 4 were repeated, which were for the passive drag device and secondary heat source, and new measurements performed for the variable area outlet. With this more efficient method, large datasets of experimental results were compiled and compared with theoretical predictions from adjoint-based sensitivity analysis of models currently under development by the group.

The experiments were performed in the linearly stable regime, with control methods that alter the linear decay rate and frequency of oscillation. Magri and Juniper (2013c) and the previous experimental work contained in chapter 3 and 4 show that, when passive control is implemented, the shift in linear growth rate when the system is unstable is equal and opposite to the shift in linear decay rate when the system is stable. In other words, passive control methods that make a stable system more stable also make an unstable system less unstable or stable. This means that these passive control methods will apply similarly to linearly unstable systems.

This chapter builds on the work of chapter 3, 4 and Mejia et al. (2016) to develop a more efficient experimental technique for experimental sensitivity analysis in thermoacoustics. The pulsed forcing technique presented in this chapter allows the same amount of data to be collected approximately 12 times faster than the data presented in chapters 3 and 4, thus allowing for significantly larger data sets to be obtained and used to refine thermoacoustic models.

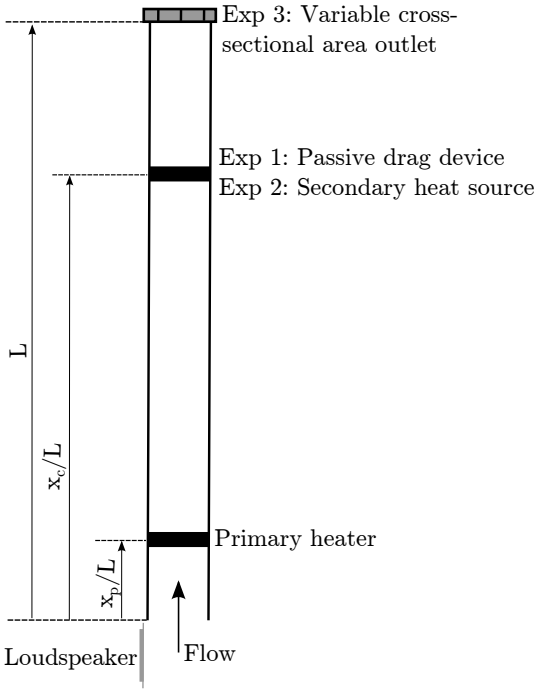

Fig. 5.1 Experimental set-up. Experiment 1: passive drag device and two open ends; Experiment 2: secondary heat source and two open ends; Experiment 3: variable area at the outlet of the tube.

5.2 Experimental set-up and data processing

5.2.1 Apparatus

Experiments were conducted on a 1 m long stainless steel vertical Rijke tube with an internal diameter of 47.4 mm and a wall thickness of 1.7 mm (figure 6.1). For all experiments, the primary heat source was attached to two rods and held in place at $x_p/L = 0.25$, the ideal location for the self-excitation of thermoacoustic oscillations (Saito, 1965). The primary heater (figure A.1a) was powered by a 640 Watt EA Elektro-Automatik EA-PSI 5080-20 A DC programmable power supply. A G.R.A.S. 46AG 1/2" LEMO microphone with a sensitivity of 12 mV/Pa was used to measure the thermoacoustic oscillations. The microphone was angled at 45° towards the inlet of the Rijke tube and placed approximately 55 mm from the bottom of the tube. The raw pressure signal was sampled at 10 kHz, much

higher than the anticipated frequencies of the thermoacoustic oscillations, 180 - 190 Hz.

Type-K thermocouples were secured at the centreline of the inlet and outlet, and at $x/L = 0.05$, 0.25, 0.50, 0.75, and 0.95. Temperature data were sampled continuously at 1 Hz and logged with an Omega TC-08 DAQ. A Pro Signal 55-1205 loudspeaker was fixed at the base of the tube. The loudspeaker was connected to an STA-500 600 W Pro Power amplifier and provided an acoustic pulse controlled through National Instruments LabVIEW. All data was acquired through National Instruments BNC-2110 DAQ device using LabVIEW.

The set-up varied according to the control method being used: (i) for the passive drag device, a wire was wrapped around two ceramic discs (figure A.1b) and mounted on two rods attached to an automated digital height gauge. This could be automatically traversed through the tube with an accuracy of ± 0.01 mm; (ii) the secondary heat source used a ISO-TECH IPS 2010 20 V 10 A programmable power supply. The secondary heat source was also a wire wrapped around two ceramic discs (figure A.1b). It was also mounted to two rods and attached to an automated digital height gauge, allowing it to be automatically traversed throughout the tube with an accuracy of ± 0.01 mm; (iii) for the variable area outlet case, a Standa 8MID60-4-H motorised iris with a maximum aperture of 60 mm and a minimum aperture of 4 mm was mounted at the outlet of the Rijke tube (figure A.1d). The iris was controlled via a Standa 8SMC4-USB-B8-1 1-axis stepper motor and could withstand temperatures of approximately 400°C, much higher than those expected during the experimental campaign, approximately 250 - 300°C. The mean flow velocity through the tube was not measured but was estimated to be between 0.1 and 1 m/s.

5.2.2 Data acquisition and processing

This Rijke tube exhibits the dynamical system behaviour of a sub-critical Hopf bifurcation. The acquisition of a single data point, containing both a linear decay rate and oscillation frequency during periods of linear decay, is shown in figure 5.2. Figure 5.2a shows the raw pressure signal of a single data point. The acquisition time was 10 seconds. During data acquisition the primary heat source had a constant power of 170 Watts. A simple proportional-integral controller was implemented to ensure that, if the resistance of the heater changed over the course of many hours, the power would remain constant, thus not introducing a systematic error into the baseline measurements.

In this study we set $P_1 = 170$ W, so that the system remained in the linearly stable region. An acoustic pulse was delivered by the loudspeaker after approximately 1.5 seconds. The acoustic pulse was a sinusoidal wave of ≈2.5 Pa amplitude, 0.05 seconds time duration, and 175 Hz frequency. This stimulated the first mode for around 9 cycles, which differs from (Mejia et al., 2016) who used a short Gaussian pulse. The type of forcing is unimportant, as long as there is sufficient amplitude to lead to a long period of linear decay in the mode one wishes to examine. As can be seen in figure 5.2, the amplitude caused by the initial pulse was larger than strictly required and there was a long period of linear decay shortly afterwards. The methods of processing the the experimental data were identical to those discussed in chapter 3 and are not repeated again here.

At each operating point in §5.3, §5.4 and §5.5, 150 data points were obtained so that a detailed uncertainty quantification of the random error could be performed. The uncertainty analysis followed the process outlined in appendix B and all error bars are presented with a 95 % confidence interval.

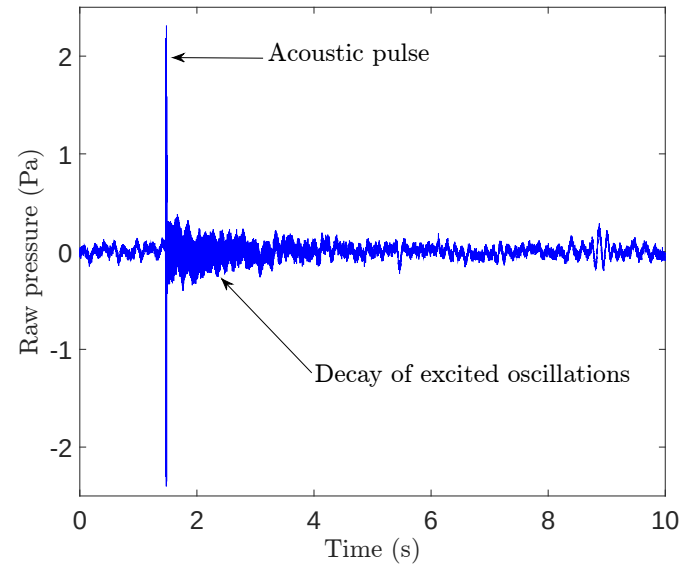

(a)

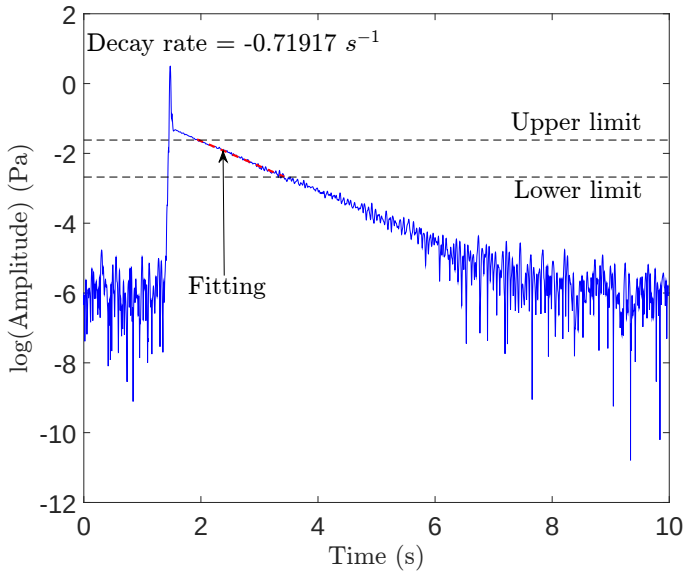

(b)

Fig. 5.2 (a) Raw pressure signal of single data point. (b) Filtered analytical signal obtained using the Hilbert transform. Red dashed line denotes the region of linear decay from which data was extracted.

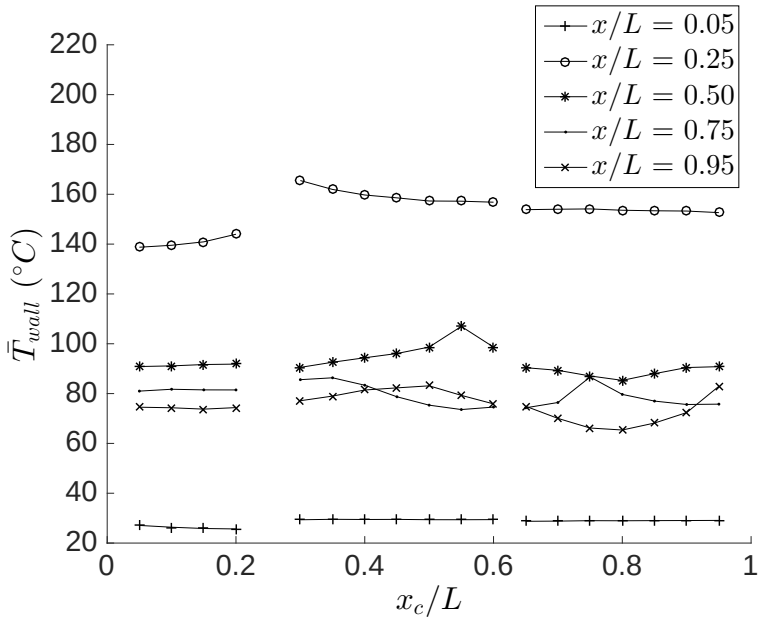

Fig. 5.3 Mean wall temperature, measured at position x/L, with the passive device placed at position x_c/L.

5.3 Control via a passive drag device

This section details an experimental sensitivity analysis that was performed to determine the effect of a passive drag device on the shift in linear decay rate and oscillation frequency during periods of linear decay.

5.3.1 Methodology

The experimental method for this control case consisted of the following steps: (i) with no control device installed in the Rijke tube, the system was allowed to reach a steady-state with $P_1 = 170$ W; (ii) 150 acoustic pulses were given in 10 second intervals resulting in 150 baseline data points; (iii) the passive drag device was introduced at a specific axial location, x_c/L, and then 150 acoustic pulses were given in 10 second intervals resulting in 150 data points for a given x_c/L; (iv) step (iii) was repeated for each axial location, between $x_c/L = 0.05$ to 0.20 and 0.30 to 0.95; (v) step (ii) was then repeated to determine whether the baseline measurements of the system had drifted over the course of the

experiments. The final baseline was determined by averaging both the "before" baseline (step (ii)) and the "after" baseline (step (v)) and interpolating a 150 point linear spacing between the two, accounting for any drift in the baseline over the course of the experiment. Figure 5.3 shows the wall temperatures measured during these experiments.

5.3.2 Shift in linear decay rate and oscillation frequency

The linear decay rate, σ_r, and oscillation frequency during periods of linear decay, σ_i, were measured experimentally for a range of x_c/L. The shift in linear decay rate and oscillation frequency defined in the theoretical studies of Magri and Juniper (2013c) were experimentally obtained as:

$$\delta\sigma_{r,i}(P_1, x_c/L) = \sigma_{r,i,c}(P_1, x_c/L) - \sigma_{r,i,0}(P_1) \tag{5.1}$$

where $\sigma_{r,c}$ is the linear decay rate measured with the passive drag device installed, $\sigma_{i,c}$ is the oscillation frequency with the passive drag device installed, $\sigma_{r,0}$ is the baseline linear decay rate, and $\sigma_{i,0}$ is the baseline oscillation frequency. The baseline linear decay rate and oscillation frequency were measured with only the primary heater installed. To determine the shift in linear decay rate, the data obtained for each x_c/L was processed in an identical way. For brevity, only the data for $x_c/L = 0.65$, 0.70, 0.75, 0.80, 0.85, 0.90, and 0.95 is presented (figure 5.4 and 5.7).

Figure 5.4a shows the baseline linear decay rates, $\sigma_{r,0}$, and the linear decay rates when a passive drag device was installed, $\sigma_{r,c}$, for a range of x_c/L. As the passive drag device was traversed toward $x_c/L = 0.95$, the magnitude of the measured linear decay rate increased, indicating that the system was becoming more stable. It was also seen that as the passive drag device was traversed toward $x_c/L = 0.95$ the variance in the data increased. This was because at these more

stable locations of the passive drag device, the linear decay rate was obtained from a fitting over fewer thermoacoustic oscillation cycles and therefore was more susceptible to random measurement error.

Figure 5.4b shows the difference between $\sigma_{r,0}$ and $\sigma_{r,c}$ for a range of x_c/L. The shift in linear decay rate due to the introduction of a passive drag device was then calculated by averaging the $\delta\sigma_r$ data obtained and plotting it as a function of x_c/L (figure 5.5a). It can be seen in figure 5.5a that the introduction of the passive drag device has a minimal effect when placed at $x_c/L = 0.60$ and the largest stabilising effect when placed at $x_c/L = 0.95$. The physical reason for this is discussed in chapter 2 and 3.

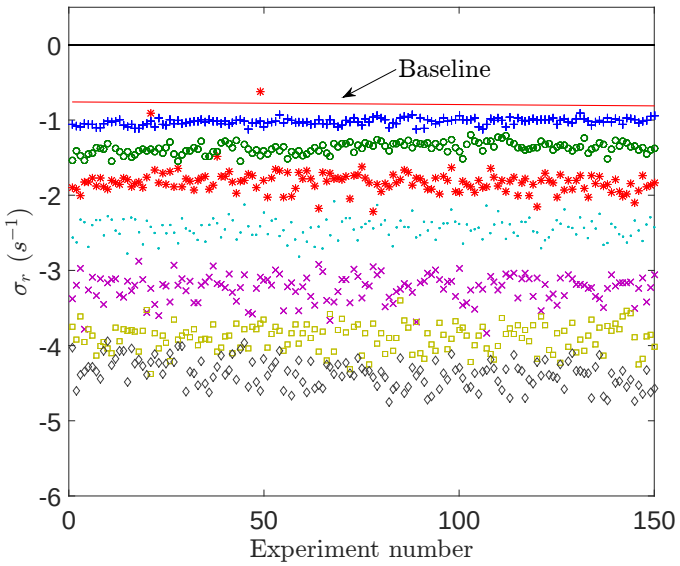

(a)

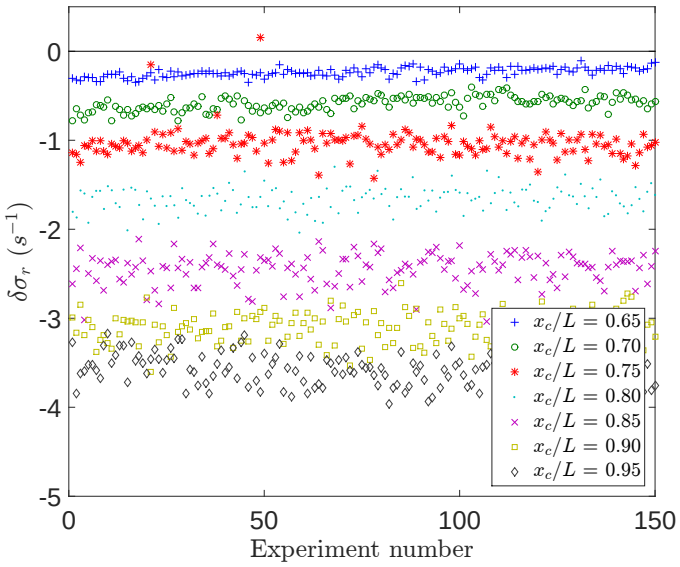

(b)

Fig. 5.4 (a) Baseline linear decay rate ($\sigma_{r,0}$), and controlled linear decay rate ($\sigma_{r,c}$) for a range of passive drag device locations (x_c/L). (b) The shift in linear decay rate ($\delta\sigma_r = \sigma_{r,c} - \sigma_{r,0}$) due to the passive drag device. Note: the legend is identical for (a) and (b) and represents x_c/L and all error bars are presented for a 95 % confidence interval. The legend is identical for (a) and (b).

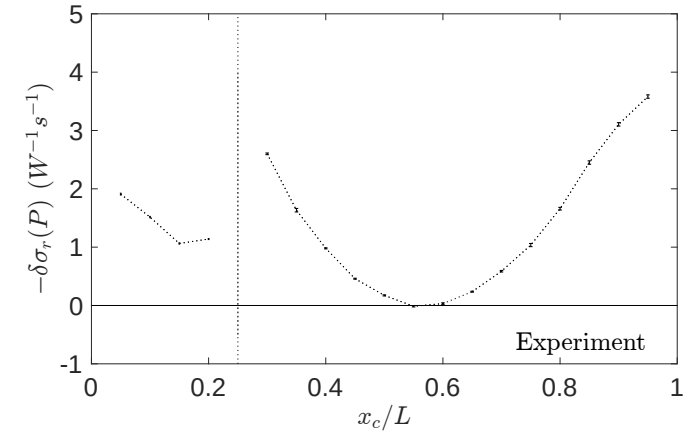

(a)

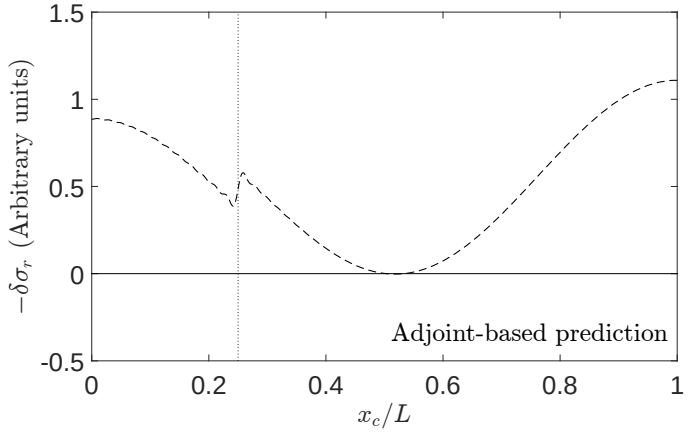

(b)

Fig. 5.5 (a) The shift in linear decay rate as a function of x_c/L. (b) Theoretical predictions of Magri and Juniper (2013c). Note: the legend is identical for (a) and (b) and represents x_c/L and all error bars are presented for a 95 % confidence interval. The legend is identical for (a) and (b).

It was also interesting to compare the shift in linear decay rate as a function of x_c/L, found in chapter 3 of this thesis, to that found using the pulsed forcing technique (figure 5.5a). Figure 5.6 shows this comparison. It can be seen that when the measured quantities are plotted together that they do not exactly match, but do however, exhibit the same qualitative features. The reason why the results do not overlay identically is probably due to the perturbations to the base flow caused by the experimental measurement. Whilst both measurements occur at the same primary heater power, the measurement methods used introduce

different perturbations to the base flow. The pulsed forcing method introduces a small perturbation to the mean flow and heat release rate via the acoustic pulse, whereas the method used in chapter 3 introduces a small perturbation to the mean flow and heat release rate via abruptly stepping the primary heater power from $P_{Hopf} + \epsilon$ to 170 W. These differences could be enough to slightly change the measured quantity.

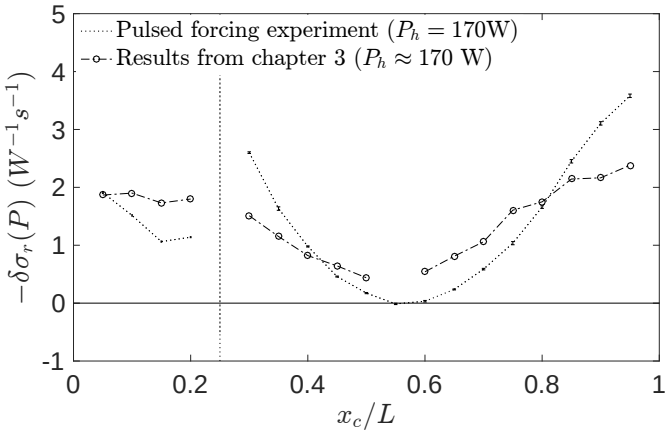

Fig. 5.6 Comparison between the shift in linear growth rate measured (i) via the pulsed forcing technique with $P = 170$ W and (ii) by stepping the primary heater power from $P_{Hopf} + \epsilon$ to 170 W (results from chapter 3).

Figure 5.7a shows the baseline oscillation frequency, $\sigma_{i,0}$, and the oscillation frequency when a passive drag device was installed, $\sigma_{i,c}$, during periods of linear decay, for a range of x_c/L. It was observed that as the passive drag device was traversed from $x_c/L = 0.65$ to 0.95 the measured oscillation frequency decreased and the variance in the data increased.

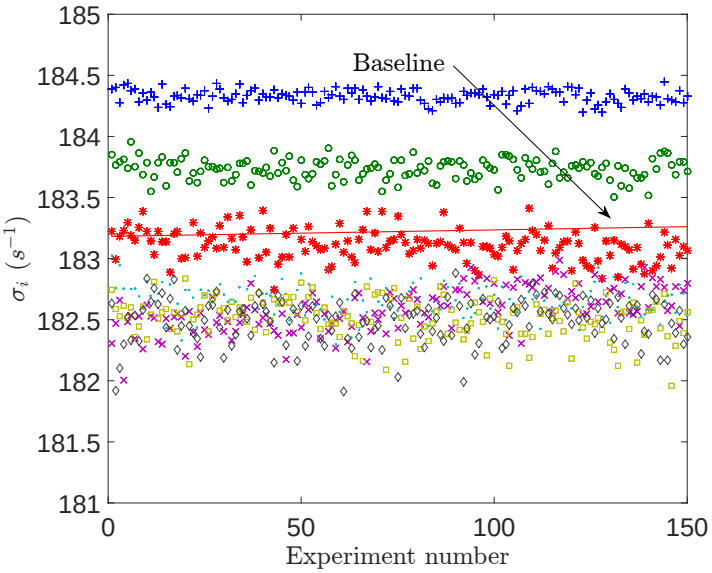

(a)

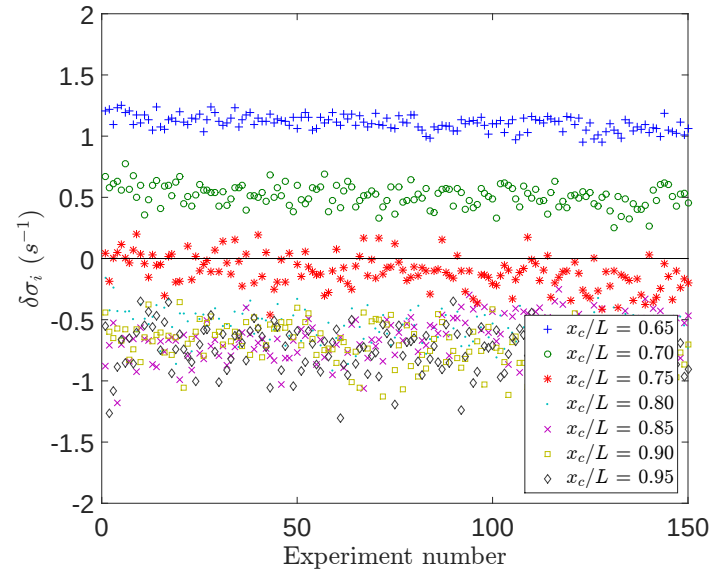

(b)

Fig. 5.7 (a) Baseline oscillation frequency during periods of linear decay ($\sigma_{i,0}$), and oscillation frequency during periods of linear decay with passive drag device installed ($\sigma_{i,c}$) for a range passive drag device locations (x_c/L). (b) The shift in oscillation frequency during periods of linear decay ($\delta\sigma_i = \sigma_{i,c} - \sigma_{i,0}$) due to the passive drag device.

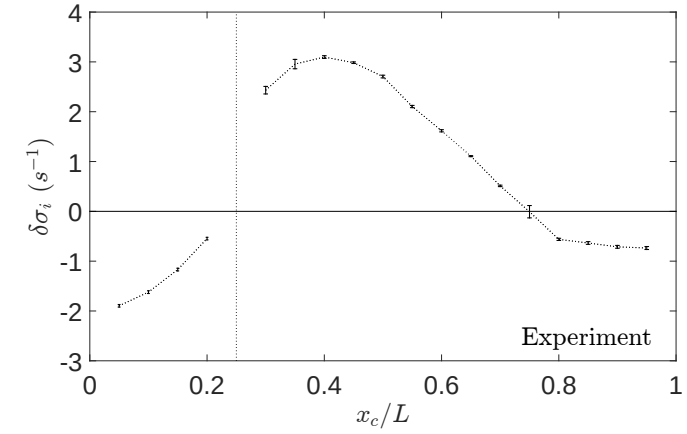

(a)

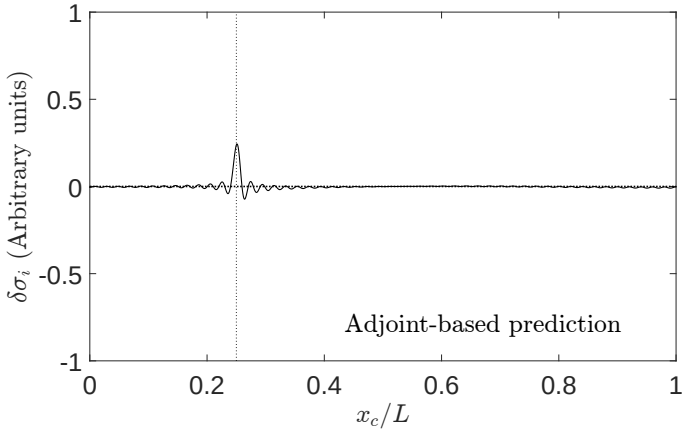

(b)

Fig. 5.8 (a) The shift in oscillation frequency during periods of linear decay as a function of x_c/L. (b) Theoretical predictions of Magri and Juniper (2013c) suggest that the model is deficient, not the adjoint. Note: the legend is identical for (a) and (b) and represents x_c/L and all error bars are presented for a 95 % confidence interval.

Figure 5.7b shows the difference between $\sigma_{i,0}$ and $\sigma_{i,c}$ for a range of x_c/L. The shift in oscillation frequency was calculated in the same way as the shift in linear decay rate and is shown in (figure 5.8a). Comparing the figures 5.8a and 5.8b it is clear that the shift in oscillation frequency predicted by Magri and Juniper (2013c) does not agree with experimental results. This discrepancy is probably because of the model's inability to capture changes in the base-state of the system due to the introduction of the passive drag device. By developing a

revised model which accounts for flow perturbations caused by the unsteady heat release rate and the drag induced by both the primary heater and the passive drag device, it may be possible to get results from an adjoint-based sensitivity analysis that provide a better quantitative comparison to experimental results. The experimental results presented here will feed back into the development of a revised model, taking into account the suggestions made throughout this thesis, to obtain a more accurate adjoint-based model of the system. This is further discussed in §8.2.

5.4 Control via a secondary heat source

This section details an experimental sensitivity analysis that measured the effect of a secondary heat source on the shift in linear decay rate and oscillation frequency during periods of linear decay.

5.4.1 Methodology

The experimental method for this control case consisted of the following steps: (i) with the secondary heater installed at the first axial location, the system was allowed to reach a steady-state with $P_1 = 170$ W and a secondary heat source power, $P_2 = 0$ W; (ii) at a given x_c/L, 150 acoustic pulses were given in 10 second intervals resulting in 150 baseline data points; (iii) at the same x_c/L used in step (ii), P_2 was increased to 5 W, at which point 150 acoustic pulses were given in 10 second intervals resulting in 150 data points; (iv) step (iii) was repeated for $P_2 = 15$, 25, 35, and 45 W, which resulted in four sets of 150 data points; (v) step (ii) was repeated twice, with $P_2 = 0$ W, allowing the system enough time to reach a steady-state. The second set of data was used as the second baseline measurement; (vi) steps (ii) - (v) were then repeated for $x_c/L = 0.05$ to 0.20 and 0.30 to 0.95.

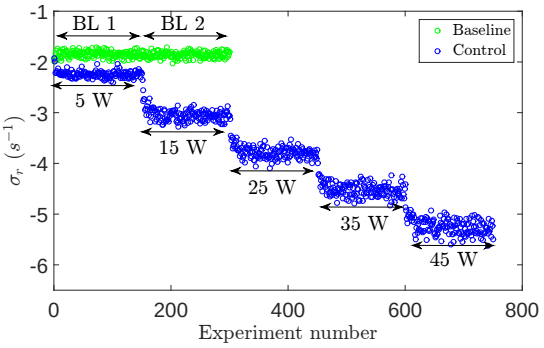

(a)

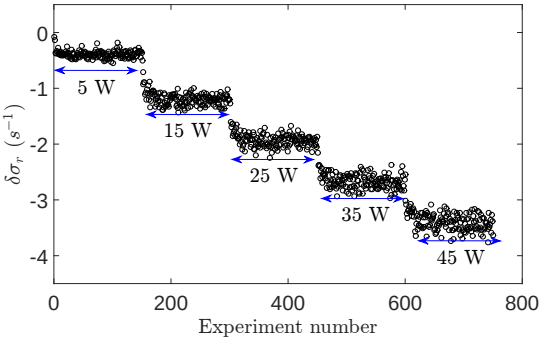

(b)

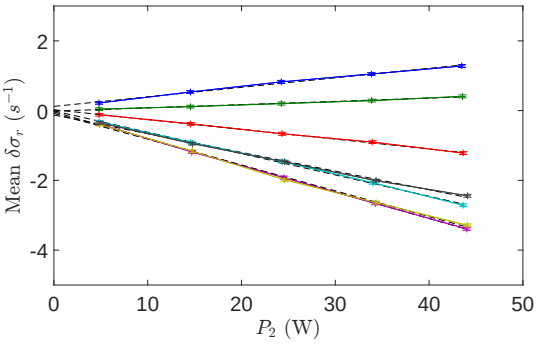

(c)

Fig. 5.9 (a) Linear decay rates measured with no control device ($\sigma_{r,0}$) and for a range of secondary heat source powers ($\sigma_{r,c}$) at $x_c/L = 0.70$. (b) Difference between the baseline linear decay rates and those measured for a range of secondary heater powers ($\delta\sigma_{r,c}$) at $x_c/L = 0.70$. (c) Averaged difference between the baseline linear decay rate ($\sigma_{r,0}$) and the linear decay rate obtained with a secondary heat source ($\sigma_{r,c}$) for a range of x_c/L. All error bars are presented with a 95 % confidence interval. The legend for (c) is the same as shown in figure 5.10c.

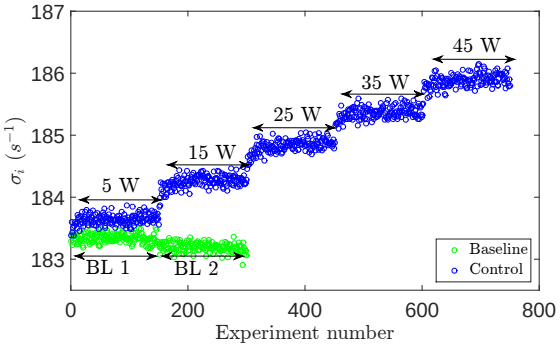

(a)

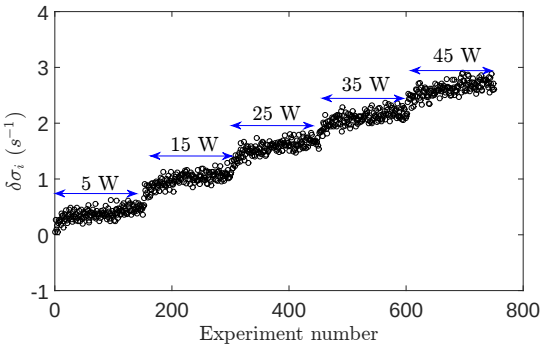

(b)

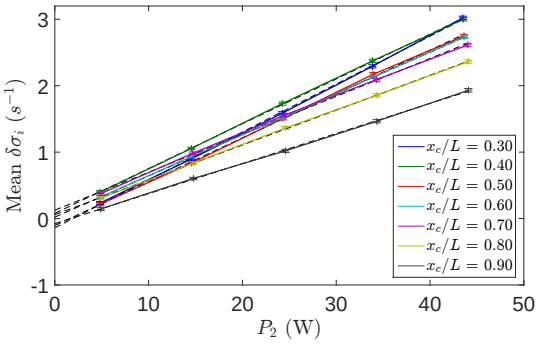

(c)

Fig. 5.10 (a) Oscillation frequency during periods of linear decay measured with no control device ($\sigma_{i,0}$) and for a range of secondary heat source powers ($\sigma_{i,c}$) at $x_c/L = 0.70$. (b) Difference between the baseline oscillation frequency during periods of linear decay and those measured for a range of secondary heater powers ($\delta\sigma_{i,c}$) at $x_c/L = 0.70$. (c) Averaged difference between the baseline oscillation frequency during periods of linear decay ($\sigma_{i,0}$) and the oscillation frequency during periods of linear decay obtained with a secondary heat source ($\sigma_{ir,c}$) for a range of x_c/L. All error bars are presented with a 95 % confidence interval.

5.4.2 Shift in linear decay rate and oscillation frequency

The linear decay rate, σ_r, and oscillation frequency during periods of linear decay, σ_i, were measured experimentally for a range of secondary heat source powers, P_2, and axial positions, x_c/L. The process used to measure the linear decay rates and oscillation frequency was discussed in §5.4.1 and was used for all data acquisition for this control case. The shift in linear decay rate and oscillation frequency, defined in the theoretical studies of Magri and Juniper (2013c), were experimentally obtained as:

$$\delta\sigma_{r,i}(P_1, P_2, x_c/L) = \sigma_{r,i,c}(P_1, P_2, x_c/L) - ... \tag{5.2}$$

$$\sigma_{r,i,0}(P_1, x_c/L) \tag{5.3}$$

where $\sigma_{r,c}$ is the linear decay rate obtained with control, $\sigma_{i,c}$ is the oscillation frequency obtained with control, $\sigma_{r,0}$ is the baseline linear decay rate obtained without control, $\sigma_{i,0}$ is the baseline oscillation frequency obtained without control, P_1 and P_2 are the same as previously defined. For brevity, only the data for $x_c/L = 0.70$ is presented here.

Figure 5.9a shows the baseline linear decay rates, $\sigma_{r,0}$, and the linear decay rates measured in the presence of a secondary heat source, $\sigma_{r,c}$, for $x_c/L = 0.70$. The final baseline was determined via the same process as discussed in §5.3.1. This 150 point dataset for the overall baseline was then subtracted from the corresponding dataset of each P_2 tested, resulting in the difference in linear decay rate with and without control, $\delta\sigma_r$ (figure 5.9b).

It can be seen in figure 5.9a that, as the power of the secondary heat source was increased from $P_2 = 5$ W to 45 W, the measured linear decay rate increased in magnitude. This increase in magnitude shows that, as expected, the secondary heat source at this location stabilizes the system.

Similar datasets to figure 5.9a and 5.9b were acquired at $x_c/L = 0.05$ to 0.20 and 0.30 to 0.95. Following this, each set of $\delta\sigma_r$ data was averaged for each individual P_2 tested. Figure 5.9c shows $\delta\sigma_r$ for $x_c/L = 0.30$, 0.40, 0.50, 0.60, 0.70, 0.80, and 0.90, illustrating how the gradient of $\delta\sigma_r$ varies with P_2 and x_c/L. A linear fit was used to extract the gradient of the averaged $\delta\sigma_r$ data. It can be seen in figure 5.9c that, as the secondary heat source was traversed through the tube, the gradient decreased from $x_c/L = 0.30$ to 0.70 and then increased from $x_c/L = 0.80$ to 0.90.

The gradients obtained in figure 5.9c were then plotted as a function of x_c/L to show the shift in linear decay rate due to the introduction of a secondary heat source (figure 5.11a). Figure 5.11a shows the results of the experimental sensitivity analysis which determined the shift in the linear decay rate due to the introduction of a secondary heat source. The experimental results are compared with the theoretical predictions by Magri and Juniper (2013c) (figure 5.11b). The physical mechanism for why a secondary heat source will have a stabilising effect in the downstream half of the Rijke tube and a destabilising effect in the upstream half of the Rijke tube is discussed in detail in chapter 4. It can be seen that the experimental results are shifted down on the vertical axis when compared with the theoretical predictions. The reason for this is not yet known.

Figure 5.10a shows the baseline oscillation frequency, $\sigma_{i,0}$, and the oscillation frequency measured during periods of linear decay in the presence of a secondary heat source, $\sigma_{i,c}$, for $x_c/L = 0.70$. The data was processed in the same way as discussed above and resulted in the difference in oscillation frequency with and without control, $\delta\sigma_i$ (figure 5.10b).

It can be seen in figures 5.10a and 5.10b that as P_2 was increased from $P_2 =$ 5 W to 45 W, the measured oscillation frequency during periods of linear decay increases in magnitude and is always positive. This was expected because, by increasing P_2, the heat transfer from the heater to the mean flow increases. As

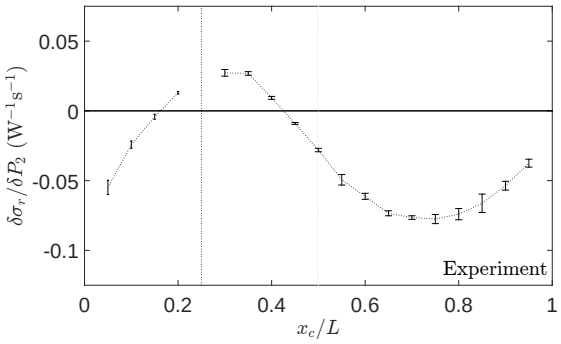

(a)

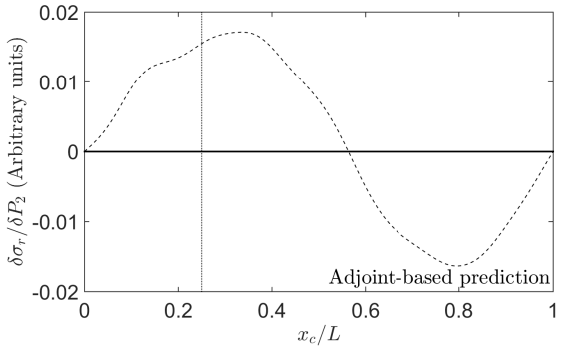

(b)

Fig. 5.11 (a) Shift in linear decay rate as a function of x_c/L. (b) Theoretical predictions of Magri and Juniper (2013c). All error bars are presented for a 95 % confidence interval.

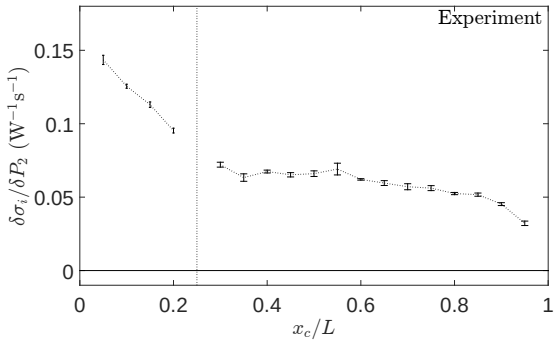

(a)

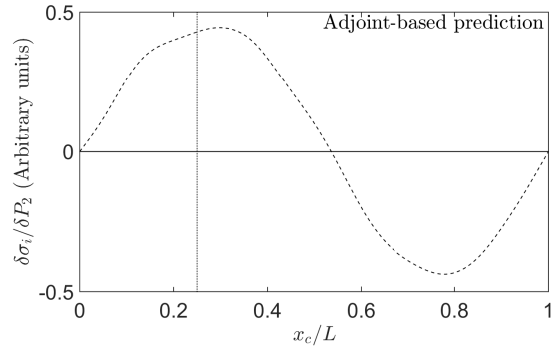

(b)

Fig. 5.12 (a) Shift in oscillation frequency during periods of linear decay as a function of x_c/L. (b) Theoretical predictions of Magri and Juniper (2013c). All error bars are presented for a 95 % confidence interval.

the mean flow temperature increases, the local speed of sound increases, resulting in an increase in oscillation frequency that will always be positive.

Similar figures to figure 5.10a and 5.10b were acquired at $x_c/L = 0.05$ to 0.20 and 0.30 to 0.95 and the same process as discussed for the linear decay rates was applied. Figure 5.10c shows $\delta\sigma_i$ for $x_c/L = 0.30$, 0.40, 0.50, 0.60, 0.70, 0.80, and 0.90. Figure 5.10c demonstrates that as the secondary heat source was traversed through $x_c/L = 0.3$ to 0.90, the gradient decreased, but always remained positive.

The gradients obtained in figure 5.10c were plotted as a function of x_c/L to show the shift in oscillation frequency observed during periods of linear decay due to the introduction of a secondary heat source (figure 5.12a). Comparing the figures 5.12a and 5.12b it is clear that the shift in oscillation frequency predicted by Magri and Juniper (2013c) again does not agree with experimental results. As discussed in chapter 4, this result is not expected. One would expect that when both the primary heater and the secondary heat source are located in the upstream half of the tube, the mean heat release rate that occurs in the upstream half of the tube would be higher than the mean heat release rate when the secondary heat source is located in the downstream half of the tube. This would result in a result similar to figure 5.12b. Therefore, the reason for the physical observations seen in figure 5.12a are currently unknown. As discussed above in §5.3.2, the model approach must be revisited before a more meaningful quantitative comparison can be made. This is discussed in further detail in §8.2.

5.5 Control via a variable cross-sectional area outlet

This section details an experimental sensitivity analysis that was performed to ascertain the effect of a variable area outlet (VAO), physically implemented with a motorised iris, on the shift in linear decay rate and oscillation frequency during periods of linear decay. To complement this data, a discussion on the effect of the VAO on the flow and wall temperature is also presented in §5.5.3.

5.5.1 Methodology

The experimental method for this control case consisted of the following steps: (i) with the VAO completely open, the system was allowed to reach a steady-state with a P_1 of 170 W; (ii) with the VAO completely open, 150 acoustic pulses were given in 10 second intervals resulting in 150 baseline data points; (iii) the diameter, D_{iris}, of the VAO was set to 45 mm and 150 acoustic pulses were given in 10 second intervals resulting in 150 data points; (iv) step (iii) was repeated for D_{iris} = 40 mm, 35 mm, 30 mm, 25 mm, 20 mm, 15 mm, and 10 mm; (v) step (ii) was repeated resulting in a second set of 150 baseline data points. The final baseline was determined via the same process as discussed in §5.3.1.

5.5.2 Shift in linear decay rate and oscillation frequency

The linear decay rates were measured experimentally for a range of VAO diameters, D_{iris}. The experimental process used to measure the linear decay rate was given in §5.5.1, and was used for all data acquisition for this control case. The shift in linear decay rate and oscillation frequency was obtained experimentally

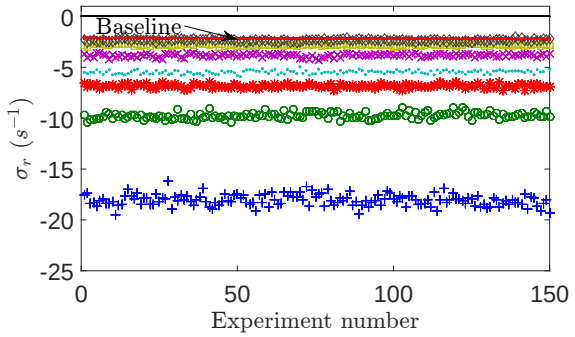

(a)

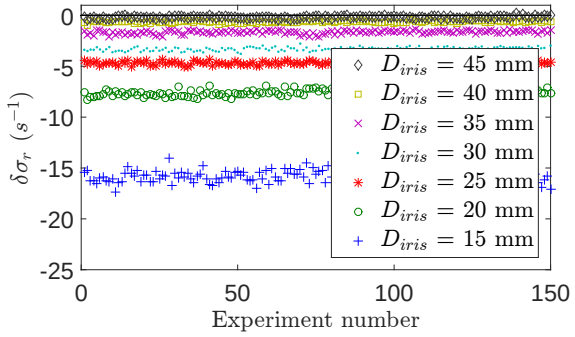

(b)

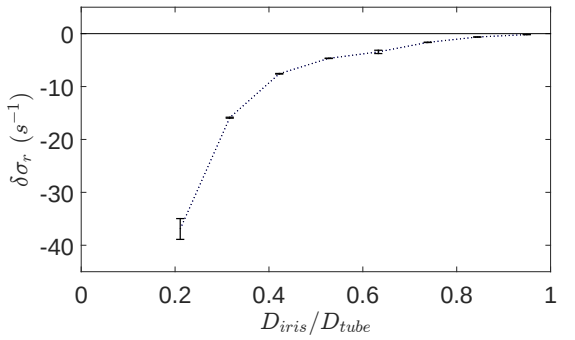

(c)

Fig. 5.13 (a) Linear decay rates measured with no control ($\sigma_{r,0}$), and with control ($\sigma_{r,c}$) for a range of D_{iris}. (b) The difference between the linear decay rates measured with no control ($\sigma_{r,0}$) and with control ($\sigma_{r,c}$). (c) The shift in linear decay rate as a function of D_{iris}/D_{tube}. The legend is identical for (a) and (b).

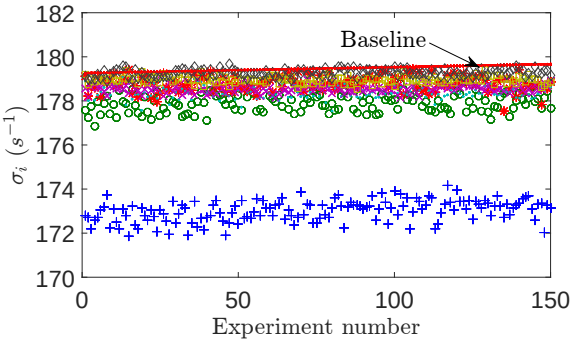

(a)

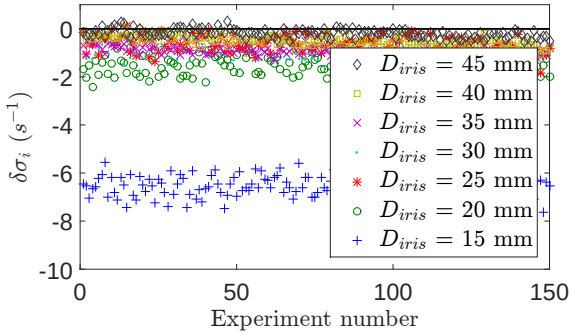

(b)

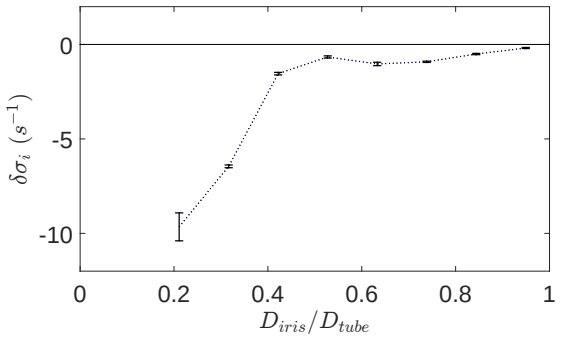

(c)

Fig. 5.14 (a) Oscillation frequency during periods of linear decay measured with no control ($\sigma_{i,0}$), and with control ($\sigma_{i,c}$) for a range of D_{iris}. (b) The difference between the oscillation frequency during periods of linear decay measured with no control ($\sigma_{i,0}$) and with control ($\sigma_{i,c}$). (c) The shift in oscillation frequency during periods of linear decay as a function of D_{iris}/D_{tube}. The legend is identical for (a) and (b).

as:

$$\delta\sigma_{r,i}(P_1, D_{iris}) = \sigma_{r,i,c}(P_1, D_{iris}) - \sigma_{r,i,0}(P_1) \tag{5.4}$$

where P_1 and D_{iris} have the same definition as in §5.5.1. Data was acquired for D_{iris} = 45 mm, 40 mm, 35 mm, 30 mm, 25 mm, 20 mm, 15 mm and 10 mm.

Figures 5.13a, 5.13b, 5.14a and 5.14b show the $\sigma_{r,i,0}$, $\sigma_{r,i,c}$, and $\delta\sigma_{r,i}$. Figure 5.13c and 5.14c show the shift in linear decay rate and shift in oscillation frequency observed during periods of linear decay, respectively, due to the VAO.

In figure 5.13c it can be seen that as the VAO was closed towards D_{iris}/D_{tube} = 0.2 the linear decay rate increased in magnitude. This was expected because by closing the VAO, the system was being transitioned from an open-open ended Rijke tube to a open-closed ended Rijke tube. For the fundamental acoustic mode: an open-open ended Rijke tube has a pressure node at either end and an antinode at the midpoint; and the acoustic velocity has a node at the midpoint and an antinode at either end. As the VAO is closed the mode shapes for pressure and acoustic velocity change, until the VAO is fully closed. At an open-closed ended state there is a pressure node located at the closed end and an antinode at the open end. The acoustic velocity has an antinode at the closed end and a node at the open end. This change in fundamental acoustic mode means that the system can no longer produce thermoacoustic oscillations as the Rijke tube instability mechanism (explained in §1.2.1) is no longer valid. Therefore, the increase in magnitude of the linear decay rate observed in figure 5.13c as the VAO is closed is entirely expected. A second point of interest was that as the VAO was closed towards D_{iris}/D_{tube} = 0.2, the variance in the obtained data increased. Because the closing of the VAO had such a stabilising effect on the system, the decay of oscillations was much faster when the aperture of the VAO was small. This fast decay meant that the linear decay rate was being calculated

from a fitting over fewer thermoacoustic oscillation cycles resulting in greater variance in the observed data. In figure 5.14c it can be seen that as the VAO diameter was reduced, the oscillation frequency continued to decrease until D_{iris} = 10 mm. This is probably because (figure 5.15a) the temperature of the gas in the tube drops as the iris is closed, for the reason described in the next section.

5.5.3 Effect of outlet diameter on flow and wall temperature

An array of type-K thermocouples were used throughout the experiment to record the effect that the VAO diameter had on the mean flow and wall temperature. This section examines: (i) the effect of the VAO on the inlet and outlet flow temperature for a range of D_{iris}; (ii) the effect of the VAO on the wall temperature at x/L = 0.05, 0.25, 0.50, 0.75, and 0.95 for a range of D_{iris}.

Reducing D_{iris}/D_{tube} restricts the flow and reduces the volumetric flow rate. Figure 5.15 shows (a) the mean outlet temperature measured at the centre of the iris aperture, (b) the mean inlet temperature, and (c) the mean wall temperatures, T_w, as a function of D_{iris}/D_{tube} at fixed heater power. These figures reveal two competing effects. On the one hand, reducing the volumetric flow rate at a fixed heater power increases the temperature jump across the heater. This effect is revealed in the monotonic increase of $T_w(x/L = 0.25)$ as D_{iris}/D_{tube} decreases in figure 5.15c. On the other hand, reducing the volumetric flow rate increases the residence time of the gas in the Rijke tube and thereby increases the temperature drop due to heat loss through the walls. This effect is revealed through the fact that T_w towards the top of the tube (x/L = 0.75 and 0.95) decreases rapidly when D_{iris}/D_{tube} is reduced below around 0.5, despite the fact that T_w towards the middle of the tube (x/L = 0.25 and 0.50) increases due to the first effect. This shows that heat loss through the walls of the tube must be modelled if an

iris is attached to the end of the Rijke tube. This effect is not currently modelled in the model of Magri and Juniper (2013c) as discussed in chapter 2. The need for an updated model is stressed throughout this thesis and in §8.2.

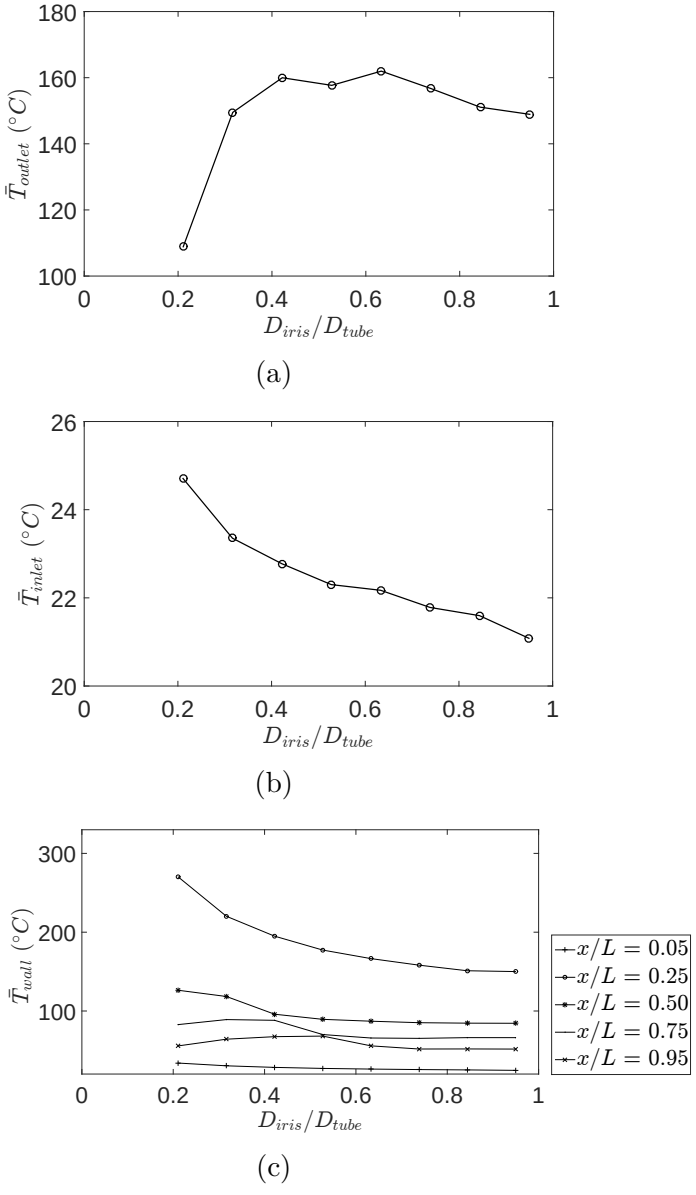

Fig. 5.15 (a) Mean outlet temperature measured at the centreline as a function of D_{iris}/D_{tube}. (b) Mean inlet temperature measured at the centreline as a function of D_{iris}/D_{tube}. (c) Mean wall temperature measured on outside of tube as a function of D_{iris}/D_{tube}. Note that all data points in (a), (b) and (c) are averaged over 150 experimental tests.

5.6 Concluding remarks

In this chapter, the work of chapters 3 and 4 was extended to develop a significantly more efficient method of experimental sensitivity analysis. We introduce an automated pulsed forcing technique that is suitable for collecting thousands of data points approximately 12 times faster than the results presented in chapters 3 and 4. In parallel with the extension of previous work we also provide a large amount of experimental data for future comparison with adjoint-based sensitivity analysis.

Chapter 6

The determination of zero growth rates via pulsed forcing and feedback control in thermoacoustic systems

This chapter was published as a part of a peer-reviewed paper in Jamieson and Juniper (2017a). All experiments and post-processing were completed by the author.

6.1 Introduction

The work presented in this chapter was the final set of experiments performed on the vertical, electrically-driven Rijke tube. This chapter builds on the work in chapters 3, 4 and 5 to show that both the pulsed forcing technique (see chapter 5) and feedback control predict similar regions of zero growth rate. This is an important result because it shows that either technique can be used for experimental sensitivity analysis in thermoacoustic systems without adding any systematic error.

With this in mind, the main aims of this chapter were to:

1. Determine the region of zero growth rate with both the pulsed forcing technique and the feedback control technique.

2. Assess the accuracy of both techniques at determining the region of zero growth rate and investigate whether any systematic discrepancies occur.

This chapter begins with a brief overview of the experimental set-up and data processing methods. The data processing methods are not discussed in depth as they are the same as outlined in chapter 5. The experimental methodology is then described before the presentation of experimental results.

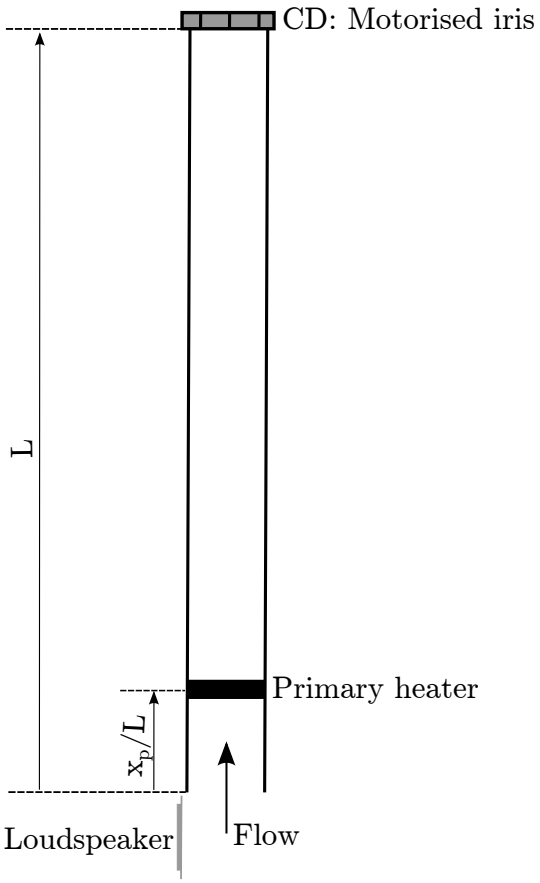

Fig. 6.1 Experimental apparatus. CD: Control Device.

6.2 Experimental set-up and data processing

6.2.1 Apparatus

Experiments were conducted on a 1 m long stainless steel Rijke tube with an internal diameter of 47.4 mm and a wall thickness of 1.7 mm (figure 6.1). For all experiments, the primary heater was held in place at $x_p/L = 0.25$, to ensure self-excitation of thermoacoustic oscillations (Saito, 1965). The primary heater was powered by a 640 Watt EA Elektro-Automatik EA-PSI 5080-20 A DC programmable power supply. An image of the primary heater is provided in appendix A. A G.R.A.S. 46AG 1/2" LEMO microphone with a sensitivity of 12 mV/Pa was used to measure the thermoacoustic oscillations. The microphone was angled at 45° towards the inlet of the Rijke tube and placed approximately 55

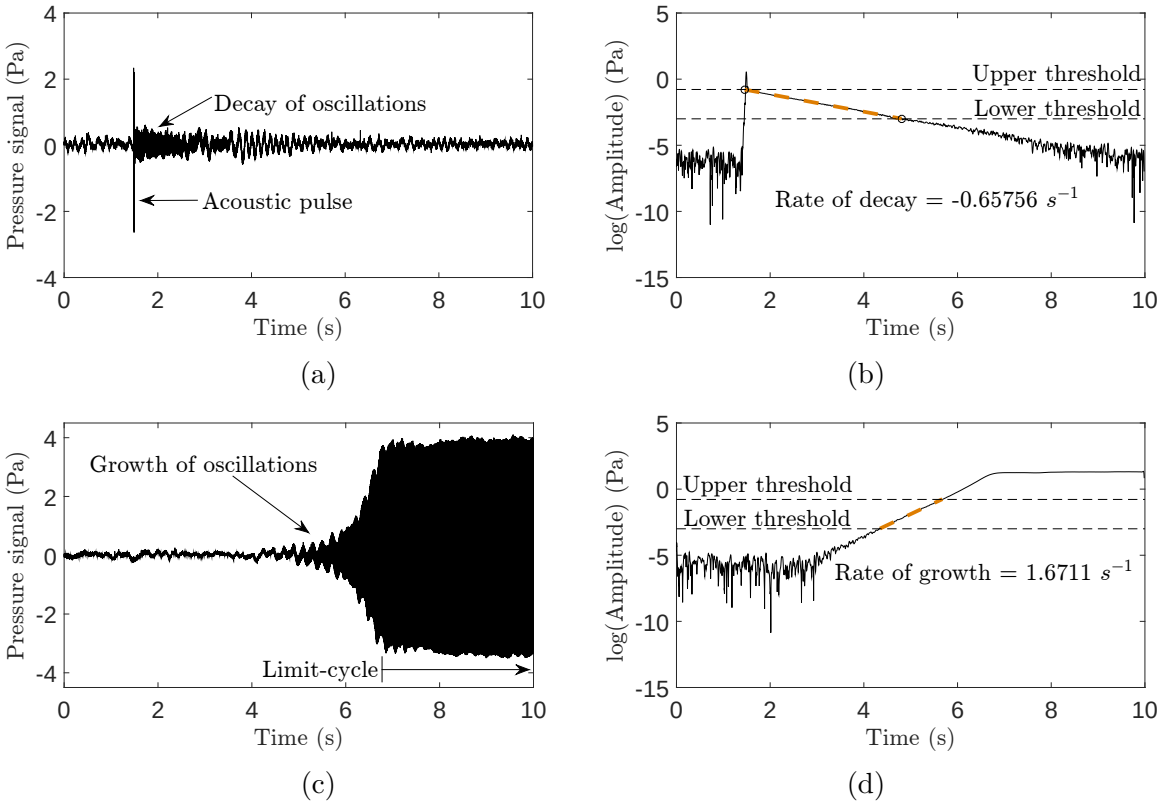

Fig. 6.2 (a) Raw pressure signal of a single data point obtained via the pulsed forcing technique. (b) Filtered analytical signal obtained using the Hilbert transform of the raw pressure signal shown in (a). (c) Raw pressure signal of a single data point obtained as the feedback controller is switched off. (d) Filtered analytical signal obtained using the Hilbert transform of the raw pressure signal shown in (c).

mm from the bottom of the tube. The raw pressure signal was sampled at 10 kHz, much higher than the anticipated frequencies of the thermoacoustic oscillations, 180 - 190 Hz. Type-K thermocouples were fixed at the center line of the outlet and inlet, as well as at $x/L = 0.05$, 0.25, 0.50, 0.75, and 0.95. Temperature data was sampled continuously at 1 Hz and logged with an Omega TC-08 DAQ. A Pro Signal 55-1205 loudspeaker was fixed at the base of the tube in parallel to the flow direction. The loudspeaker was connected to a STA-500 600 W Pro Power amplifier and provided an acoustic pulse controlled through National Instruments LabVIEW. All data was acquired through National Instruments BNC-2110 DAQ device using LabVIEW. A Standa 8MID60-4-H motorised iris with a maximum

aperture of 60 mm and a minimum aperture of 4 mm was mounted at the outlet of the Rijke tube and used for the experiments detailed in §6.2.2 and §6.3. The iris was controlled via a Standa 8SMC4-USB-B8-1 1-axis stepper motor and could withstand temperatures of approximately 400°C.

6.2.2 Data acquisition and processing

The acquisition of a single data point, containing a linear decay rate, is shown in figure 6.2a and 6.2b. The acquisition timing was 10 seconds, during which time the primary heater had a constant power output of 170 W. An acoustic pulse was delivered by the loudspeaker and was characterised by a sinusoidal wave of approximately 2.5 Pa amplitude, 0.05 seconds time duration, and 175 Hz frequency. These parameters were chosen to ensure that the system was never triggered. The acoustic pulse causes the system to become momentarily excited, before the oscillations decay as the system behaves like a damped harmonic oscillator, transitioning back to its steady-state (Mejia et al., 2016). For the results presented in §6.3, the primary heater power was not held constant and the amplitude of the acoustic pulse was approximately 2.75 Pa.

The linear growth rates measured in §6.3 were acquired by switching off a feedback controller at $t = 0$ shown in figure 6.2c. The theory and design of feedback controllers is out of the scope of this thesis. It was used simply as a black box that could be switched on and off as required. The controller used throughout §6.3 was an in-house built phase-shift amplifier, similar to the set-up used by Heckl (1988). The controller was set up to output a signal to the loudspeaker positioned at the base of the tube. As the system grows to a stable limit-cycle, the raw pressure signal is measured.

The data processing for both the linear growth and decay rates is identical to that described in chapter 5 and for brevity, are not discussed here.

For all experiments in §6.3, a simple proportional-integral controller was implemented to ensure that if the resistance of the heater changed over the course of many hours, the power output would remain constant, thus not introducing a systematic error into the baseline measurements.

6.3 Results

This section reports results from the pulsed forcing technique and feedback control technique on the prediction of zero growth rate. All uncertainty quantification is performed following the same procedure as outlined in appendix B and the error bars are presented with a 95% confidence interval. It is important that the experimental results obtained in both the oscillatory regime and non-oscillatory regime are compatible with one another and that the pulsed forcing technique and/or feedback control technique does not introduce bias or systematic error into the results. A simple way to perform this investigation is to measure the Hopf bifurcation point ($P_{1,Hopf}$) for a given iris diameter (D_i/D_t) and then (i) use feedback control to obtain growth rates for $P_1 > P_{1,Hopf}$, and (ii) use the pulsed forcing technique to obtain decay rates for $P_1 < P_{1,Hopf}$ (figure 6.3). With both these sets of data obtained, a linear fitting was applied to each set of data to see whether both techniques predict the same region of zero growth rate.

It is important to emphasise that the pulsed forcing technique measures linear decay rates and the feedback control technique measures linear growth rates. Neither technique measures both linear growth and decay rates. Therefore a convenient way to compare them is to extrapolate to the operating points with zero growth rate and check that these two points are sufficiently close. It is also important to note that (i) the physical positions of the microphone and the loudspeaker are the same for both set-ups (pulsed forcing and feedback control); and (ii) once the acoustic pulse or the active control has stopped, the system

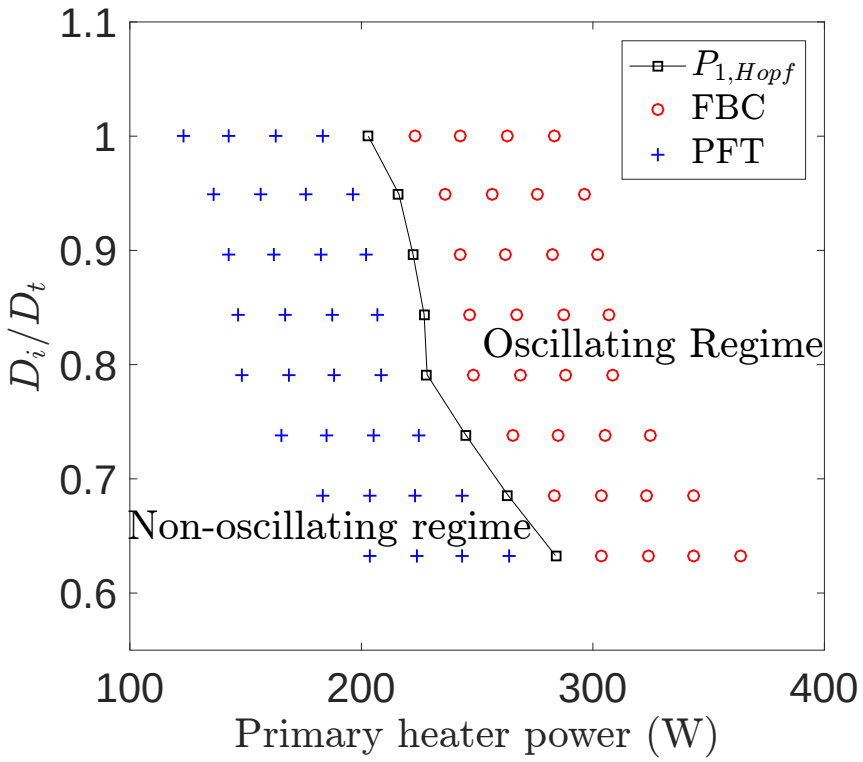

Fig. 6.3 Operating region for results presented in §6.3. $P_{1,Hopf}$ indicates the stability curve for a variety of iris diameters. FBC denotes points where data is taken via feedback control. PFT denotes points where data is taken via the pulsed forcing technique. Spacing between each red circle and each blue cross is 20 W.

receives no further input from the loudspeaker. Therefore, the measured linear growth and decay rates should not be affected by the set-up.

The experimental method for this investigation consisted of the following steps: (i) for a given D_i/D_t, obtain the $P_{1,Hopf}$; (ii) at $P_{1,Hopf}+20$ W the system was allowed to reach a steady-state and then the feedback controller was switched on and then off in 10 second intervals until 25 growth rates were obtained; (iii) step (ii) was repeated in 20 W increments up to $P_{1,Hopf}+80$ W; (iv) steps (i) - (iii) were repeated for $D_i/D_t = 1$, 0.95, 0.90, 0.84, 0.79, 0.74, 0.69, and 0.63; (v) at $P_{1,Hopf}-20$ W the system was allowed to reach a steady-state and an acoustic pulse was delivered in 10 second intervals until 25 decay rates were obtained; (vi) step (iv) was repeated in 20 W increments up to $P_{1,Hopf}-80$ W;

(vii) steps (v - vi) were repeated for the same range of D_i/D_t. Figure 6.3 shows the operating region used for the experiments in §6.3. It can be seen that as the iris is closed from $D_i/D_t = 1$ to 0.63, the primary power input required to transition the system to an oscillatory state increases, the reason for which is discussed in chapter §5.5.2.

The measured linear growth and decay rates for eight iris diameters are presented in figures 6.4a-h. The mean linear growth rate and linear decay rate was then obtained, and presented for each operating point in figure 6.5. It can be seen in figure 6.5 that the trend in both the mean linear growth rates and mean linear decay rates was almost linear. The fitting applied to the data points was a linear fit. By inspecting the fitting, it was evident that both the linear growth rates and linear decay rates predict similar regions of zero growth rate. Discrepancies in the prediction could be due to external noise and/or environmental changes between days of experiments. The Rijke tube operated at temperatures of approximately 100 - 380°C and ambient air temperature and humidity changed by approximately 8°C and 5%, respectively, over the course of a day.

These results show that both the pulsed forcing technique and the feedback control technique predict similar regions of zero growth rate and the use of one technique over the other does not seem to add any significant intrinsic bias or error to the predicted region of zero growth rate.

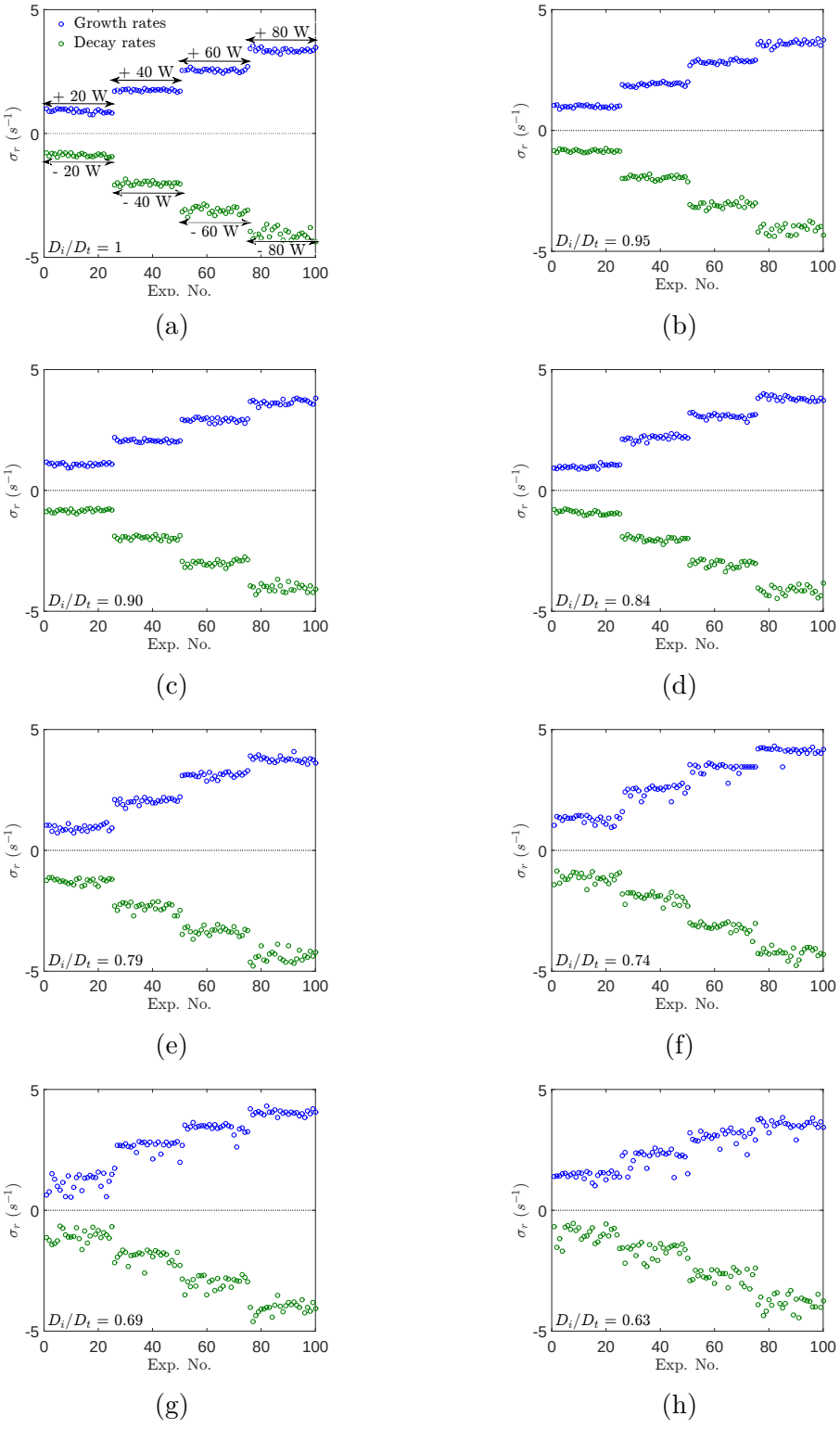

Fig. 6.4 Linear growth rates measured via feedback control and linear decay rates measured via pulsed forcing for a range of iris diameters.

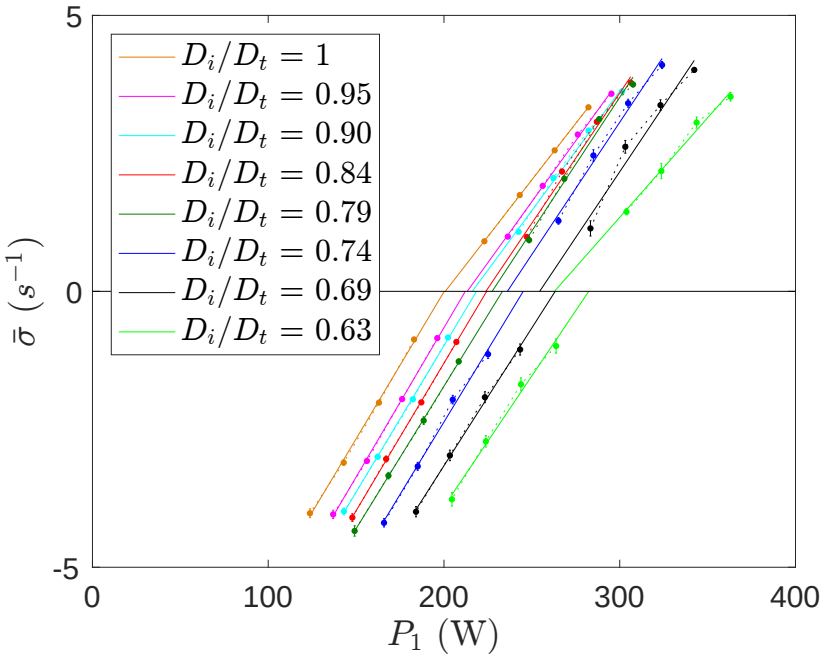

Fig. 6.5 Averaged linear growth and decay rates for a range of D_i/D_t. A linear fit is applied to each set of linear growth and decay rate data.

6.4 Concluding remarks

This chapter presented the final experiments conducted on the vertical, electrically-driven Rijke tube. The chapter built on chapters 3, 4, and 5 to show that both the pulsed forcing technique and feedback control predict the same region of zero growth rate. This is an important result for future work in experimental sensitivity analysis as applied to thermoacoustic systems as it means that we can measure linear growth and decay rates, and compare them with confidence, rather than just measuring one or the other.

Chapter 7

Sensitivity of a ducted premixed conical laminar flame to changes in convective time delay

All experimental work and data processing presented in this chapter was performed by the author. §7.4 detailing the Cantera calculations was performed by the author with assistance from Mr Anh Khoa Doan (Cambridge University Engineering Department). The base code is available from the Cantera website titled "adiabatic_flame.py". Modifications to this code to allow for the calculation of laminar flame speed was performed with Mr Doan.

7.1 Introduction

This chapter builds on the work of chapters 3, 4, 5, and 6 by taking the techniques developed on an electrically-driven Rijke tube and applying them to the study of a real combustion system: a ducted premixed conical laminar flame.

The work was then taken a step further by investigating the stability characteristics of this thermoacoustic system in the presence of a changing convective time delay, τ_c, and a varying fuel composition. An investigation of how τ_c effects the linear growth and decay of thermoacoustic oscillations is relevant as it is known to be one of the most sensitive parameters in a thermoacoustic system (Juniper and Sujith, 2018). With this in mind, the main aims of the work presented in this chapter were:

- To demonstrate that the techniques developed for an electrically-driven thermoacoustic system can be used on a combustion-driven thermoacoustic system.

- To determine the sensitivity of linear growth and decay rates to a change in τ_c.

- To determine the sensitivity of the frequency of oscillation observed during periods of linear growth and decay are to a change in τ_c.

- To determine the sensitivity of the unperturbed flame length, L_f, is to changes in fuel composition.

The chapter begins with a brief discussion of the open-source code Cantera, which has been used to calculate the laminar flame speed, S_l, of flames with varying concentrations of methane (CH_4), ethylene (C_2H_4) and air. Next, we show how τ_c of our system can be determined and compare experimental results

with those from empirical expressions based on the Cantera calculations. Finally, a sensitivity analysis was performed to achieve the aims that are listed above.

This chapter is the final results chapter presented in this thesis and provides a platform for the future work. The future direction of the research, for which this chapter lays the foundation for, is discussed in chapter 8.2.

7.2 Main assumptions

This section details the main assumptions of the analysis contained within this chapter. Particularly, the assumptions relating to the relationship between the heat release parameter and the convective time delay are discussed.

In this chapter the main assumption is that the heat release rate perturbations can be modelled as being proportional to the velocity perturbation some time earlier, with a single time delay, i.e. taking the form of an $n-\tau$ model where n is the mean heat release rate and τ is the time delay. While a velocity perturbation will, in reality, induce heat release rate perturbations at all subsequent times, to a first approximation, one can approximate this as a big pulse of heat release rate a single time later, as shown in Semlitsch et al. (2017). It was shown in Semlitsch et al. (2017) that a velocity ratio perturbation induces a heat release perturbation a time, τ_f, later over a large range of amplitudes. Particularly, in figure 7 of Semlitsch et al. (2017), the flame describing function behaviour can be interpreted by a single time delay.

In the study of Semlitsch et al. (2017), an M-type flame was investigated. This idea has also been explored for Bunsen type flame's similar to what was studied in this chapter. In chapter 4 of his PhD thesis, Kashinath (2013) studied the influence of the perturbation convection speed on a ducted premixed laminar flame. Kashinath (2013) showed via Direct Numerical Simulations (DNS) that a perturbation velocity could be simplified to a single travelling wave

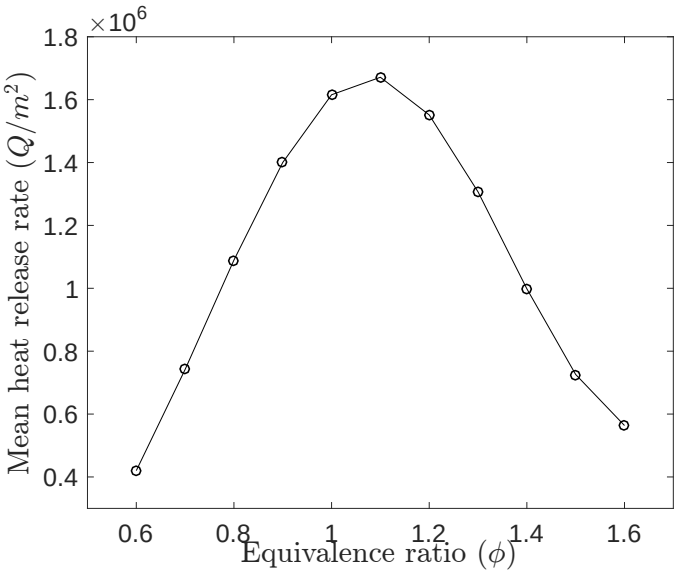

Fig. 7.1 Mean heat release rate as the equivalence ratio is changed for a 50 % methane/ 50 % ethylene mixture. All parameters used to generate this result were the same as discussed in §7.4 of this chapter.

with a frequency dependent phase speed, i.e. showing that heat release rate perturbations could be modelled as being proportional to a velocity perturbation some time earlier, with a single time delay.

Whilst the $n - \tau$ model is a good first approximation it is important to acknowledge the model's weaknesses. The main weakness of the $n - \tau$ model is that it does not model the fact that flames behave as low-pass filters. However, it is assumed in this work that at the low frequencies that were examined, this should not matter.

The other important point is that a change in mixture composition will change the mean heat release rate and whether this should be taken into account. This physical effect will change n in the $n - \tau$ model. Figure 7.1 quantifies how the mean heat release rate changes as the equivalence ratio of the mixture was varied. The Cantera code detailed in §7.4 was used to produce figure 7.1. It can be seen in figure 7.1 that maximum mean heat release rate corresponds to a fuel-air mixture with ϕ between 1 and 1.1 (stoichiometric), as expected. Whilst

this change in mean heat release rate will affect the n term in the $n-\tau$ model, it will not affect the time delay term, τ (Juniper and Sujith, 2018). The stability of the thermoacoustic system, i.e. whether or not the system is thermoacoustically oscillating, is primarily determined by τ in the $n-\tau$ model. Therefore, because the primary focus of this work was to show how sensitive the thermoacoustic system in question was to changes in time delay, τ, we assume that these changes in mean heat release rate are negligible in our analysis in the context of the $n-\tau$ model.

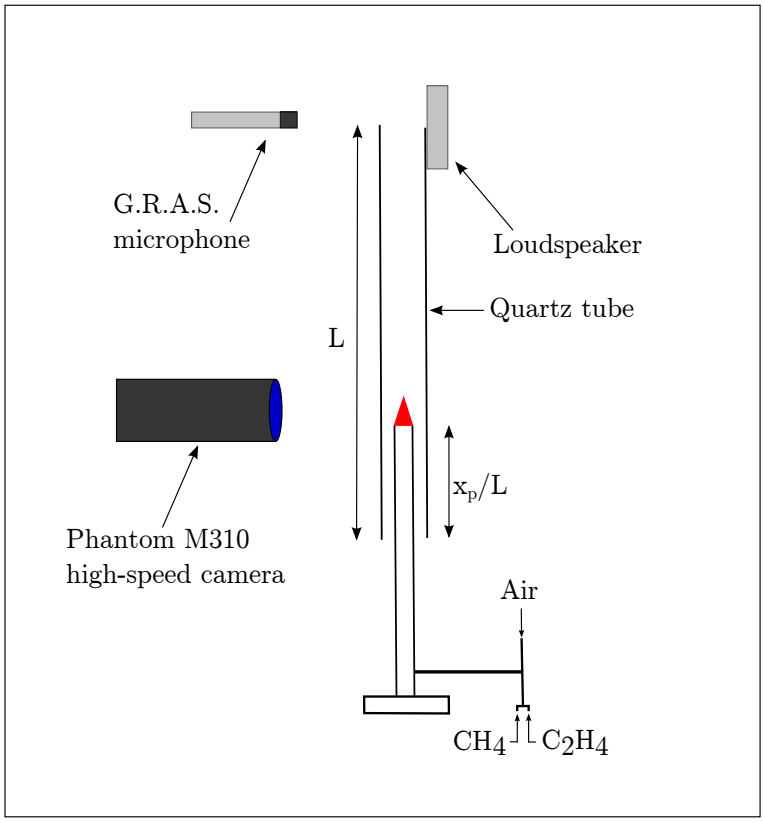

Fig. 7.2 Experimental set-up.

7.3 Experimental set-up and data processing

7.3.1 Apparatus

Experiments were conducted on a 750 mm long Philips Type PH300 Quartz vertical Rijke tube with an inner diameter of 25 mm and an outer diameter of 28 mm (figure 7.2). For all experiments, the burner was located at $x_p/L = 0.25$, the optimal location for the self-excitation of thermoacoustic oscillations (Saito, 1965). The burner was made from stainless steel with a length of 400 mm, an outer diameter of 14 mm and an inner diameter of 12 mm. The fuel mixture was comprised of methane (CH_4) and ethylene (C_2H_4). Ethylene was chosen as the additional fuel because it allowed for a larger operating range of S_l to be explored and its addition did not cause large changes in volumetric ratio because it required only a small amount more air than methane during combustion. The

methane, ethylene and air lines were controlled by three separate Bronkhorst EL-FLOW Select digital mass flow controllers[3] and controlled simultaneously through a Bronkhorst FLOW-BUS controller. Before the fuel-air mixture passed through the main burner tube, the mixture passed through a 1 m length of Swagelok piping with two 180° bends, to ensure that the mixture was fully premixed and that laminar flow had fully developed. A G.R.A.S. 46AG 1/2" LEMO microphone with a sensitivity of 12.99 mV/Pa was used to measure thermoacoustic oscillations. The microphone was located approximately 100 mm from the outlet of the tube. The raw pressure signal was sampled at 10 kHz, much higher than the anticipated frequencies of the thermoacoustic oscillations, approximately 300 Hz. A Visation Round Cabinet Speaker (RS Stock No. 431-8686) was fixed at the top of the tube. The loud speaker was attached to a bracket that traversed as the quartz tube was traversed. The traverse used was a digital height gauge with an accuracy of ±0.01 mm. The loud speaker was connected to an STA-500 600 W Pro Power amplifier and provided an acoustic pulse through National Instruments LabVIEW. A Phantom M310 high-speed camera was positioned in line with the flame, approximately 380 mm from the flame. The camera was controlled via Phantom Camera Control software and an external trigger was supplied via National Instruments LabVIEW when a recording was required.

7.3.2 Data acquisition and processing

The camera settings used throughout the experimental campaign are given in table 7.1.

[3]Methane: F-201CV-5KO-RAD-22-V 0 - 2 ln/min; Ethylene: F-201CV-2KO-RAD-22-V 0 - 1 ln/min; Air: F-201CV-20K-RAD-22-V 0 - 20 ln/min. All three mass flow controllers had a rated accuracy of ± 0.5 % Rd + 0.1 % FS.

Table 7.1 Phantom MIRO M310 settings

Specification	**Setting**
Image size (pixels)	512x512
Resolution	0.1538
Sample rate	3000 fps
Exposure time	330 μs
Frames obtained/run	201
Camera	Phantom MIRO M310
Lens	Nikon AF Nikkor 50 mm 1:1.4D

Whilst no image data of the oscillating flame was used in the final iteration of the experimental campaign, initially the plan had been to acquire data showing the flame oscillating over many thermoacoustic cycles. With this in mind it was important to make sure that the 201 frames that were captured contained sufficient information about the thermoacoustic oscillations. The frequency of the self-excited first mode was approximately 300 Hz. This gave a period of $1/300 \approx 3.3$ ms. If the image data was sampled at 3000 Hz, then 201 frames contained $(201/3000) \approx 67$ ms of data. This means that around 20 cycles could be obtained over 201 frames. Each set of 201 frames was stored as a multipage .TIFF image so that an image processing algorithm could be applied to each individual frame. A threshold filter was then applied to ensure only the conical section of the flame was visible. The methodology of the threshold filtering is discussed further in §7.5.1.

Throughout the flame experiments, the percentage (by volume) of methane and ethylene in the mixture was kept constant. The reasons for this were: (i) to be able to easily achieve an incremental increase in flame length; and (ii) to make sure that a range of data could be obtained in the self-excited regime. Initially,

it was difficult to achieve both a clear incremental increase in the flame length whilst also achieving a range of measurements in the self-excited regime.

Data was acquired in both the linearly stable regime and the self-excited regime for a total acquisition time of 10 seconds per data point. In the linearly stable regime, data was acquired with the pulsed forcing technique (figure 7.3). In the self-excited regime, data was acquired by turning on and off an in-house built phase-shift amplifier feedback controller (figure 7.4). The acquisition of a single data point, containing both a linear decay or growth rate and frequency observed during periods of linear decay, is shown in figures 7.3 and 7.4. For the data obtained in figure 7.3, an acoustic pulse was a sinusoidal wave of ≈ 2 Pa amplitude, 0.05 seconds time duration, and 300 Hz frequency. This stimulated the first mode for around 0.5 seconds, which is around 150 cycles. For the data obtained in figure 7.4, the feedback controller was turned off, allowing the thermoacoustic oscillations to grow. During this period of growth, the linear growth rate and frequency observed during the period of linear growth were obtained. The data acquisition and processing of the linear decay rates (figure 7.3), growth rates (figure 7.4) and frequencies observed during periods of linear growth and decay was identical to the methods explained in chapters 3 and 6.

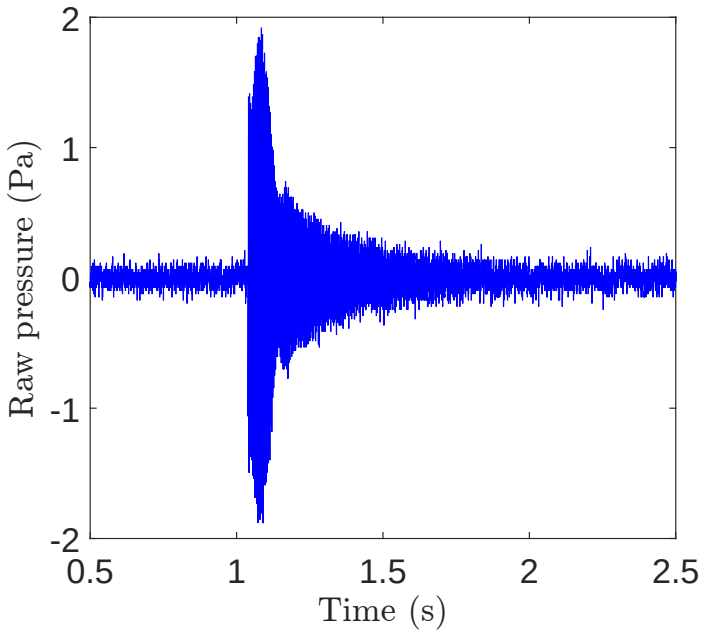

(a)

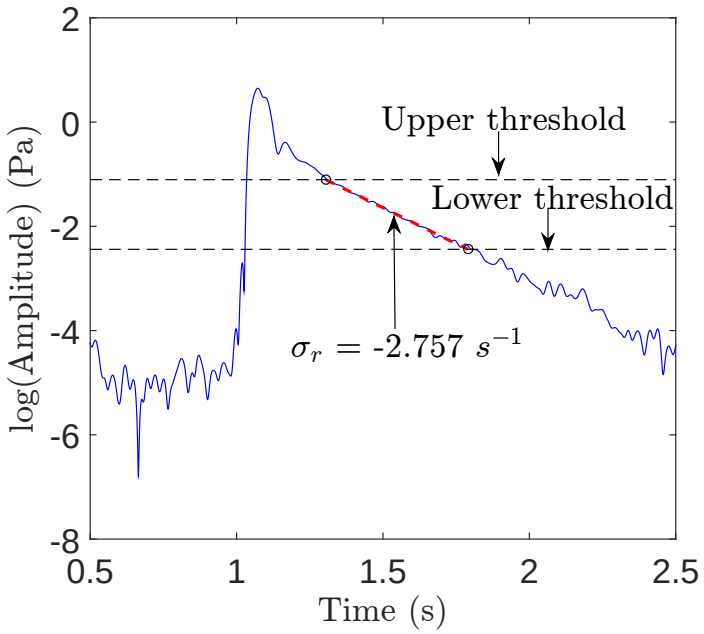

(b)

Fig. 7.3 (a) Raw pressure during one linear decay rate measurement after a pulse at t = 1 s. (b) Filtered analytical Hilbert transformed signal during one decay rate measurement, showing linear decay over approximately 1 s. The linear decay rate is measured between the dashed lines, over approximately 0.5 s, which is 150 cycles.

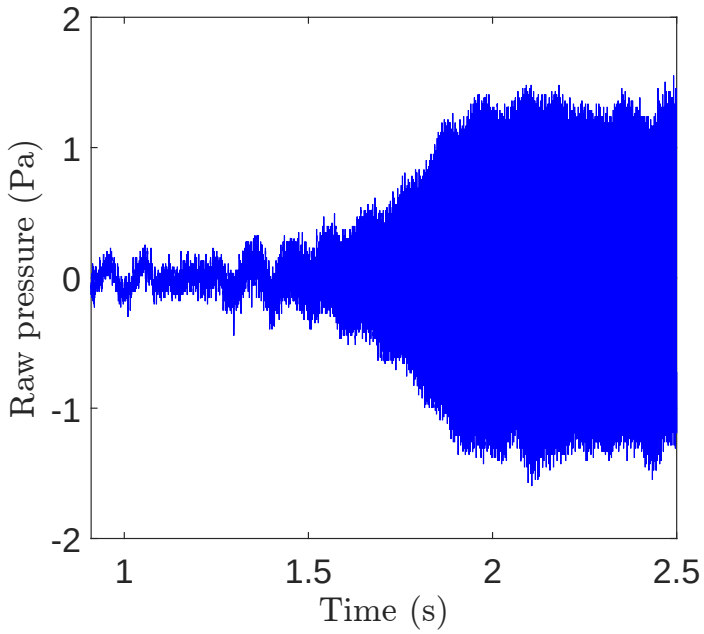

(a)

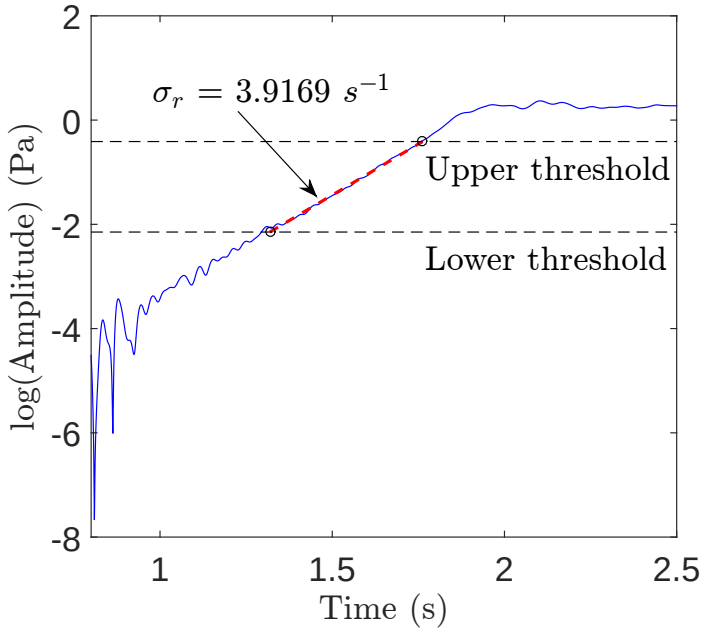

(b)

Fig. 7.4 (a) Raw pressure during one linear growth rate measurement after the feedback controller is turned off at approximately t = 1 s. (b) Filtered analytical Hilbert transformed signal during one linear growth rate measurement, showing linear growth over approximately 1 s. The growth rate is measured between the dashed lines, over approximately 0.5 s, which is 150 cycles.

7.4 Laminar flame speed changes due to fuel composition

The flame geometry of a premixed laminar conical flame can be altered by changing the fuel composition and/or the mass flow rate of the fuel and oxidiser. The aim of this section is to (i) show how S_l can be calculated with the open-source code Cantera, (ii) show how this code can be validated with experimental work from the literature, and (iii) to empirically calculate L_f, based on Cantera results and make a comparison with experimentally obtained values of L_f.

It should be noted that because the Cantera code is an *off-the-shelf* open-source code, a brief overview will be given, but the in-depth details of the numerical solver and machinery of the code will not be discussed, as it was outside the scope of how it was used in this work.

7.4.1 Cantera calculations

Cantera is an open-source code for use in problems involving combustion, chemical kinetics, thermodynamics and transport processes (Goodwin et al., 2017). In this work, Cantera was used to calculate the S_l of methane, ethylene and air combustion at a variety of equivalence ratios, ϕ. The code used for this work was built upon the "adiabatic_flame.py" example provided on the Cantera website.

The first parameters that had to be specified were the ambient temperature and ambient pressure. For all calculations these were specified as $T_a = 300$ K and $P_a = 1$ atm. Whilst the temperature and pressure varied slightly over the course of the experiments, the effect of this was neglected because for temperature, the calculation of S_l is dominated by the ignition temperature. The ignition temperature was so much greater than ambient temperature, that any small change in ambient temperature will have a negligible effect the S_l calculation.

For pressure, any change in pressure observed in the laboratory was less than 1 % of the reference atmospheric pressure and therefore deemed negligible to the calculation of S_l.

The second setting that had to be set was the reaction mechanism that was to be used in the calculation. A reduced mechanism for methane-ethylene-air mixtures called $c12\_red$ was used (Luo et al., 2011). It was based on USC Mech Version II (Wang et al., 2007) and GRI Mech 3.0 (Smith et al., 2017). It contained 269 reactions, 44 species and predicted the S_l of both pure methane and air combustion (figure 7.5a) as well as pure ethylene and air combustion (figure 7.5b) in a reasonable amount of time, roughly 40 minutes per equivalence ratio. This was the mechanism that was used for this work.

The final setting that had to be specified was the reactants to be used in the calculation. The reactant only portion of this equation was determined to be:

$$\Big[CH_4(1-\alpha)\phi + \alpha\phi C_2H_4\Big]_{fuel} + \left[(2+\alpha)\left(O_2 + \left(\frac{0.79}{0.21}\right)N_2\right)\right]_{oxidiser} \tag{7.1}$$

where α is the percentage of ethylene in the fuel mixture, and ϕ is the specified global fuel equivalence ratio.

The Cantera code was then run to calculate the S_l for a range of $\phi = 0.6$ to 1.6.

7.4.2 Validation of laminar flame speed predictions

Before any meaningful comparisons were made between the Cantera calculations and experimental observations, a validation of the laminar flame speed predictions was performed. Two sets of Cantera results were obtained: (i) S_l for pure methane/air combustion for $\phi = 0.6$ to 1.6 (figure 7.5a); and (ii) S_l for pure ethylene/air combustion for $\phi = 0.6$ to 1.6 (figure 7.5b).

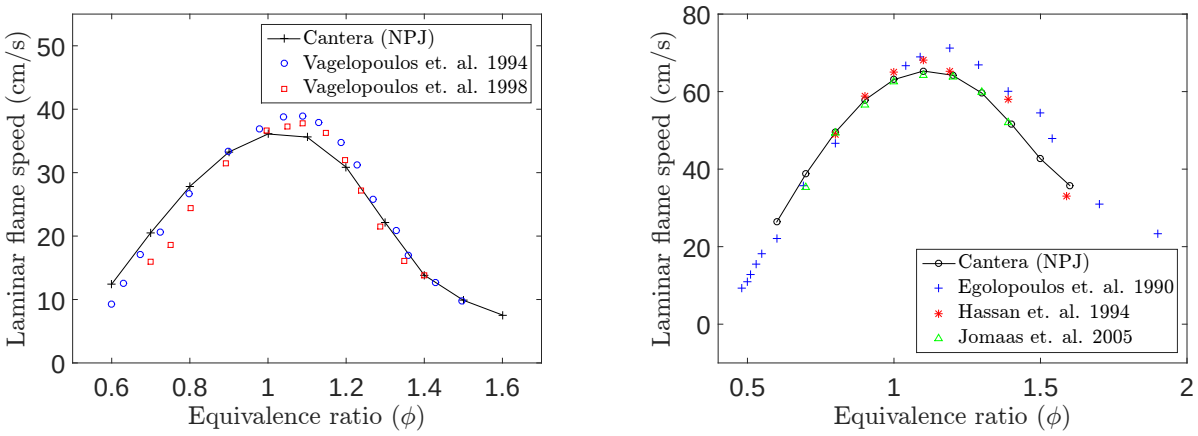

(a) (b)

Fig. 7.5 (a) S_l as a function of equivalence ratio for a pure methane-air flame. Cantera calculation validated against Vagelopoulos et al. (1994) and Vagelopoulos and Egolfopoulos (1998). (b) S_l as a function of equivalence ratio for a pure ethylene-air flame. Cantera calculation validated against Egolfopoulos et al. (1990), Hassan et al. (1998) and Jomaas et al. (2005).

Figure 7.5a shows the Cantera calculation overlayed with the experimental results of Vagelopoulos et al. (1994) and Vagelopoulos and Egolfopoulos (1998) for pure methane/air combustion. It can be seen that the experimental results of Vagelopoulos et al. (1994) and Vagelopoulos and Egolfopoulos (1998) compare well to the calculations obtained by using Cantera. Figure 7.5b shows the Cantera calculation overlayed with the experimental results of Egolfopoulos et al. (1990), Hassan et al. (1998), and Jomaas et al. (2005) for pure ethylene/air combustion. It can be seen that the experimental results of Egolfopoulos et al. (1990), Hassan et al. (1998) and Jomaas et al. (2005) compare well to the results obtained by using Cantera.

As the code was validated for the limit cases of pure methane/air combustion and pure ethylene/air combustion, it was assumed that it held for any intermittent case of varied ethylene percentage in the fuel mixture. It is possible for differential diffusion of the different fuels in the mixture to arise, which could effect the

intermittent results of the Cantera code. However, we assumed that this effect was minimal for a fully premixed system.

7.4.3 Results

This section presents two sets of results: (i) S_l of methane/ethylene/air flames as a function of equivalence ratio and fuel composition calculated with Cantera; and (ii) a comparison of experimental results and empirical results based on Cantera for the calculation of L_f.

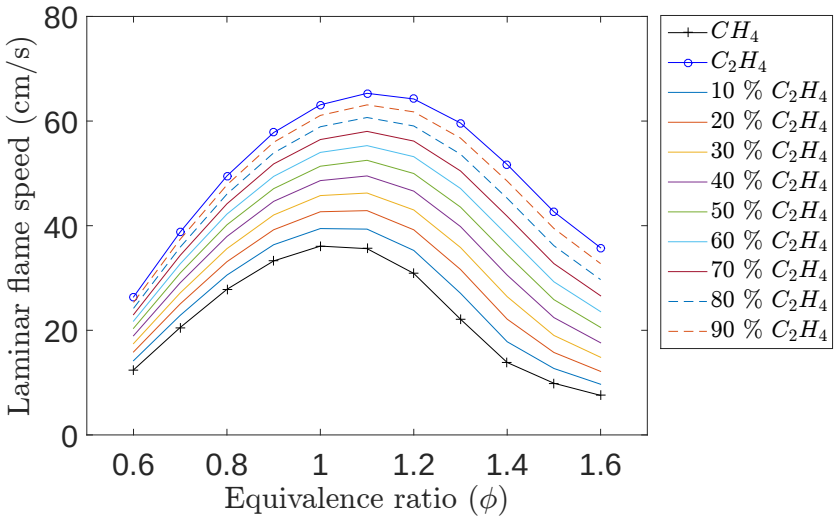

Fig. 7.6 Range of S_l achievable with methane, ethylene and air mixtures.

Figure 7.6 shows how the S_l changes as a function of equivalence ratio and fuel composition. After the two limit cases of pure methane/air and pure ethylene/air were validated, the percentage of ethylene in the calculation was varied from 10 - 90 %. This yielded a range in which the S_l could be predicted by Cantera. Initially, only a mixture of methane and air was to be used in this experimental campaign, however, as one of the aims of the investigation was to study how the stability of the system was effected by a changing time delay it was clear that the flame geometry had to be able to be varied considerably. One way to do this was to ensure a wide operating range of S_l could be achieved. It can be seen

in figure 7.6 that the S_l almost doubles from approximately 36.1 cm/s to 63.11 cm/s at $\phi = 1$, and almost increases five times from approximately 7.56 cm/s to 35.78 cm/s at $\phi = 1.6$.

Figure 7.7 shows a comparison between the experimentally measured L_f, and the L_f obtained empirically using Cantera. The experimental process for determining L_f is discussed in §7.5.1. The empirical formula that was used to determine L_f based on Cantera results was from bunsen theory (Turns, 2012):

$$L_f = R\left[\frac{u_b^2 - S_l^2}{S_l^2}\right]^{1/2} \tag{7.2}$$

where R is the radius of the burner measured from the centreline to the outside wall, the outer radius was used because the flame was anchored to the outside of the burner tube; u_b is the bulk flow velocity of the unburnt reactants; and S_l is the laminar flame speed. S_l was determined from the results presented in figure 7.6. To determine the correct S_l the the equivalence ratio of the experimental mixture was determined via the following method:

1. The following equation for a methane, ethylene and air combustion at stoichiometric conditions was established:

$$\begin{aligned} &\Big[CH_4(1-\alpha) + \alpha C_2H_4\Big]_{fuel} \; ... + \\ &\Big[(2+\alpha)\Big(O_2 + \Big(\frac{0.79}{0.21}\Big)N_2\Big)\Big]_{oxidiser} \; ... \\ &\rightarrow (1+\alpha)CO_2 + 2H_2O + (2+\alpha)\Big(\frac{0.79}{0.21}\Big)N_2 \end{aligned} \tag{7.3}$$

   where α is the percentage of ethylene in the fuel mixture.

2. The stoichiometric air-to-fuel ratio was then determined from equation (7.3) in terms of mole fractions as:

$$AFR_{st} = \frac{X_{air,st}}{X_{fuel,st}} = \frac{(2+\alpha) + (2+\alpha)\left(\frac{0.79}{0.21}\right)}{(1-\alpha)+\alpha} \tag{7.4}$$

3. Finally, the equivalence ratio of the mixture was then determined as:

$$\phi = \frac{AFR_{st}}{AFR} \tag{7.5}$$

where AFR is the actual air-to-fuel ratio.

Once the correct ϕ was determined, an interpolation was performed with the results shown in figure 7.6 to ascertain the corresponding S_l. This was the S_l that was used in the calculation of L_f via equation (7.2).

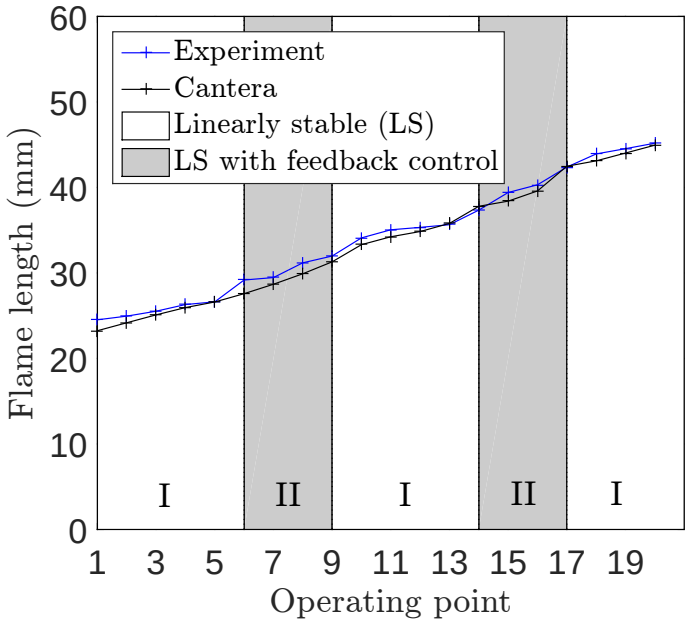

Fig. 7.7 L_f variations with operating point. A comparison is made with the results from the Cantera calculations. I = data obtained when the system was self-linearly stable; II = data obtained when the system was linearly stable in the presence of a feedback controller.

Figure 7.7 shows a comparison between the L_f determined directly from experimental data and the empirical L_f based on Cantera calculations (equation (7.2)). The operating points are shown in appendix C and were chosen to provide a linearly increasing range of L_f. In this work, only fuel-rich equivalence ratios were used, this was sufficient as we were only interested in ensuring varying L_f could be studied. We found that when the flame was operated in a lean regime, it was difficult to avoid blow-off on this particular system. The empirical results from Cantera are shown in black and it can be clearly seen that agree well with the experimental results.

This result is provided because it shows the range of L_f used for the experimental campaign and because it provided another test for the Cantera calculations to be compared against experimental data obtained directly from this work.

7.5 Determining the convective time delay

This section explains how τ_c was determined from experimental observations and presents findings on how τ_c was effected by L_f. In the context of this work, τ_c refers to the time it takes for a perturbation at the flame base to convect up the flame front and pinch off at the flame tip. The perturbations are manifested in the form of a travelling wave and the time delay in question is crucial to the understanding of the thermoacoustic mechanism. It is this time delay that allows the unsteady heat release rate to be correctly phased with the acoustic pressure, encouraging thermoacoustic oscillations (Crocco and Cheng, 1956).

In this work the L_f and bulk velocity, u_b, were essential to the calculation of τ_c. In the following sections, an explanation of how these properties were obtained is given.

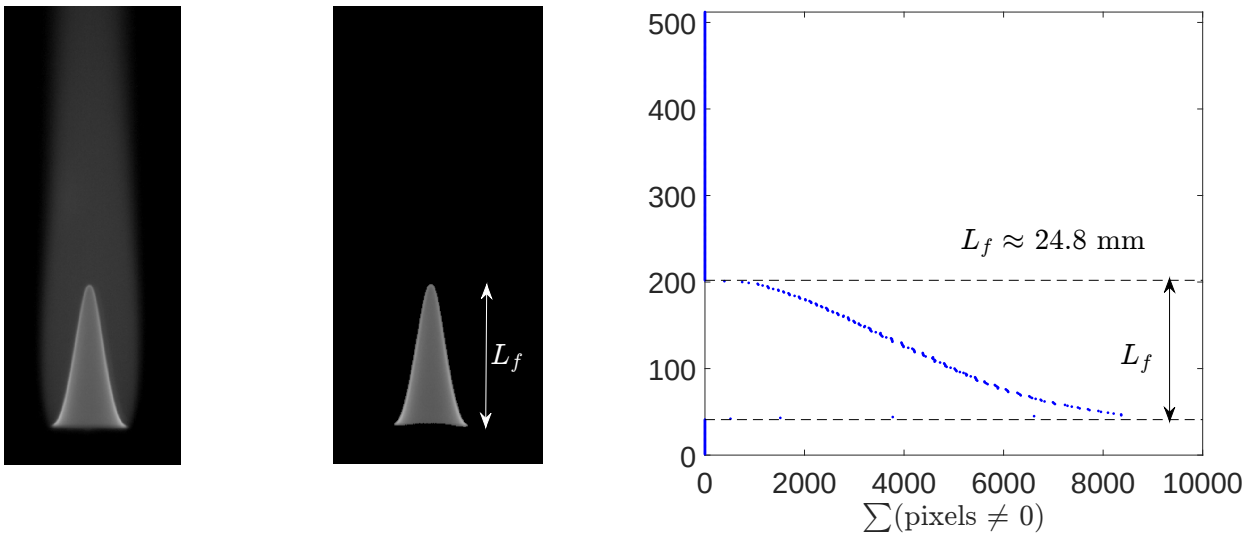

(a) (b) (c)

Fig. 7.8 (a) Unprocessed flame image (natural emission integrated over line of sight). (b) Filtered image of the flame (a threshold value, F_{th}, where $F_{th} > x$ was set to zero. x was modified on a trial and error basis determined by the flame geometry). (c) Horizontal axis shows the summation of non-zero pixels to determine L_f. Note: 1 pixel $\approx$ 0.1538 mm.

7.5.1 Determining the flame length

The L_f was determined from images obtained with the Phantom MIRO M310 high-speed camera under the settings shown in table 7.1. It was shown in §7.4.3 that across the operating points examined, the system demonstrated periods of linear stability and self-excitation. During the operating points at which the system was self-excited, the oscillations were suppressed with the feedback controller discussed in §7.3.2 so that images could be acquired of the flame in a non-oscillatory state.

Figure 7.8 shows the process of determining L_f. Figure 7.8a shows the unprocessed flame image as natural emission integrated over the line of sight. A threshold filter was then applied to isolate the conical flame area (figure 7.8b). The threshold filter was constructed by setting a condition that every pixel with a value < 80 was set to 0. This was done on a trial and error basis, however, it

was tested for a range of different flame configurations. It was found that for the range of flames investigated in this work that a threshold condition between 65 and 85 always allowed the conical flame structure to be captured. Once the threshold filtered image was obtained, a summation of the pixel values in the horizontal direction was performed on every row of the image matrix. This resulted in figure 7.8c and clearly shows that the non-zero values on the vertical axis make up L_f. The distance, in pixels, between the dashed lines in figure 7.8c was then obtained and multiplied by a the resolution to obtain L_f in mm. The resolution was ≈ 0.1538 mm per pixel. This process was repeated for each of the 201 frames of the image and then the mean was obtained. For the case shown in figure 7.8, the mean flame length was approximately 24.8 mm with a standard deviation of approximately 0.14 mm. The mean L_f is reported in this work.

7.5.2 Determining the convective time delay

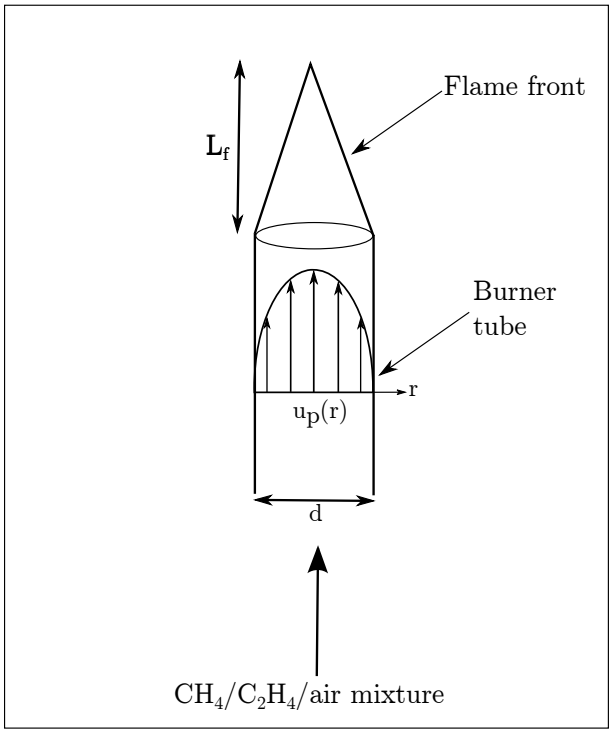

Fig. 7.9 Schematic of flame-burner configuration for the calculation of τ_c. L_f is the unperturbed flame length, $u_p(r)$ is the Poiseuille velocity profile as a function of the burner radius, r, and d is the burner diameter.

Figure 7.9 is a schematic of the flame-burner configuration for the calculation of τ_c. In figure 7.9, L_f has the same definition as defined in §7.1, $u_p(r)$ is the velocity as a function of the burner radius, assuming a Poiseuille velocity profile. This assumption is valid because the flow is laminar (Re = $\rho_{mix} u D/\mu_{mix} \approx$ 600 - 700)[4]. Once L_f was determined for each operating point, τ_c could be calculated from:

$$\tau_c = \frac{L_f}{u_{avg}} \tag{7.6}$$

[4]Calculated using the density and dynamic viscosity of the mixture. The volumetric flow rate of methane, ethylene and air was calculated as a percentage of the total volumetric flow rate. The density and dynamic viscosity was multiplied by this percentage. The values for each gas was then added together, i.e. $\rho_{mix} = \rho_{CH_4} * (V_{CH_4}/V_{Total}) + \rho_{C_2H_4} * (V_{C_2H_4}/V_{Total}) + \rho_{Air} * (V_{Air}/V_{Total})$. The same was performed for calculating μ_{mix}

where τ_c and L_f have the same definition as above, and u_{avg} is the average flow velocity, $u_{avg} = 0.5u_{max}$ which is true if the flow has a Poiseuille velocity profile.

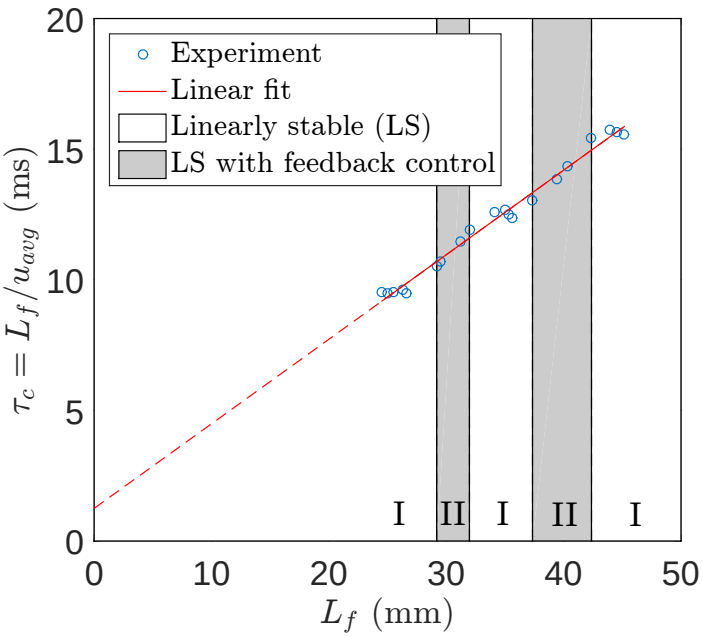

Fig. 7.10 (a) τ_c as a function of L_f. I = data obtained when the system was self-linearly stable; II = data obtained when the system was linearly stable in the presence of a feedback controller.

7.5.3 Results

Figure 7.10 shows how τ_c changes as L_f is varied. It can be seen in figure 7.10 that the experimental results do not pass through zero. It can be seen that the data obtained both when the system is linearly stable and linearly stable in the presence of feedback control follows a linear trend. Even though the data does not pass through zero, we decided to keep the linear fit, because it is the best fit line to the experimental data and we will interpolate within this data range rather than extrapolate from it.

7.6 Sensitivity analysis

This section details the sensitivity analysis that was performed to determine: (i) how sensitive the linear growth and decay rates were to changes in τ_c, (ii) how sensitivity the frequencies observed during periods of growth and decay were to changes in τ_c, and (iii) how sensitive L_f was to changes in fuel composition.

7.6.1 Sensitivity of linear growth and decay rates to changes in convective time delay

The linear growth and decay rates, σ_r, were measured experimentally for the range of operating conditions outlined in appendix C. Each operating point corresponded to a different L_f and thus a different τ_c. At each of the 20 operating points, 40 linear growth or decay rates were measured using the methods outlined in §7.3.2 so that a detailed uncertainty analysis could be performed to minimise random error (see appendix B). Operating points 1 to 5, 10 to 13, and 18 to 20 were obtained in the linearly stable regime via the pulsed forcing method. Operating points 6 to 9 and 14 to 17 were obtained in the self-excited regime with the use of feedback control.

Figure 7.11a shows the linear growth and decay rates measured over the experimental campaign for each operating point. Once this data was acquired, the mean, $\bar{\sigma}_r$, was obtained and plotted against the corresponding τ_c (figure 7.11b). It can be seen in figure 7.11b that as the τ_c was increased, $\bar{\sigma}_r$ was cyclic, with the difference in τ_c between linearly stable regions approximately equal to the period of oscillation (T = 1/300 $\approx$ 3.3 ms), as expected (Crocco and Cheng, 1956; McManus et al., 1993). This sensitivity of the linear growth and decay rate to changes in τ_c was the a subject of a recent review paper by Juniper and Sujith (2018) and arises when τ_c is not small relative to the thermoacoustic oscillation period, T, of an acoustic mode. If this is the case, then small changes in τ_c can

lead to large changes in the thermoacoustic mechanism for a given system. It can be clearly seen in figure 7.11b that the measured τ_c were larger than the thermoacoustic oscillation period given above. Therefore, in accordance with the review by Juniper and Sujith (2018), it was observed that small changes in τ_c did in fact cause large changes to the stability regions of the system.

This result was analytically shown in McManus et al. (1993), where a stability criterion was derived based on the Rayleigh criterion, the frequency of the thermoacoustic oscillations, ω, and τ_c. McManus et al. (1993) showed that an open-ended flame driven Rijke tube system could be approximated to be self-excited if $\sin(\omega\tau_c) > 0$. Conversely, if $\sin(\omega\tau_c) < 0$ the system could be approximated to be linearly stable. Figure 7.12 gives the plotted expression of McManus et al. (1993) for the range of τ_c observed in figure 7.11b. Comparing figure 7.11b and 7.12, it is clear that the theoretical prediction that small changes in τ_c lead to large changes in the stability of the system is physically observed in experiments. The main difference between figure 7.11b and 7.12 is that the analytical results in figure 7.12 are sinusoidal, whereas the experimental results in figure 7.11b are cyclic but not perfectly sinusoidal. It would be expected that the stability of the system as a function of τ_c would be sinusoidal. In the context of this expectation, the reasons for why the experimental results are not perfectly sinusoidal are presently unknown.

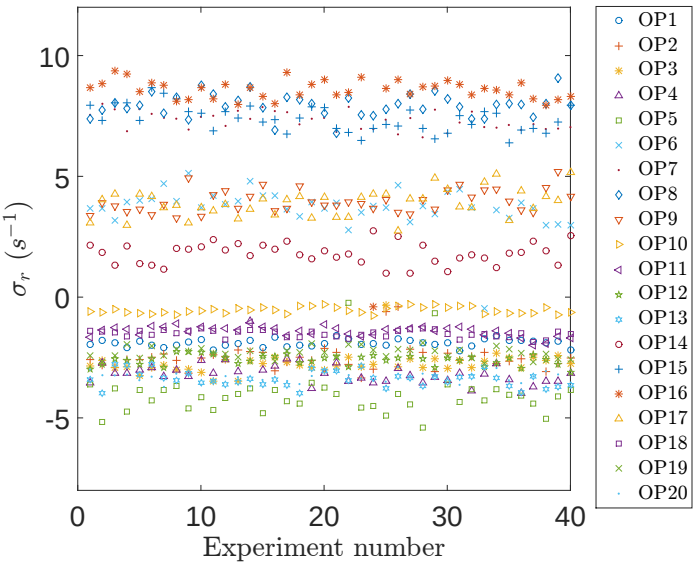

(a)

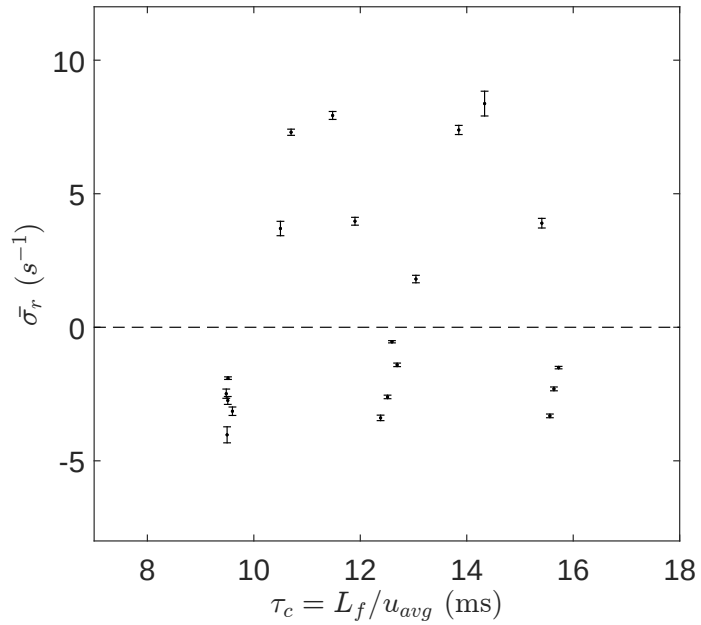

(b)

Fig. 7.11 (a) Linear growth and decay rates obtained for different operating points. (b) Linear growth and decay rate as a function of τ_c.

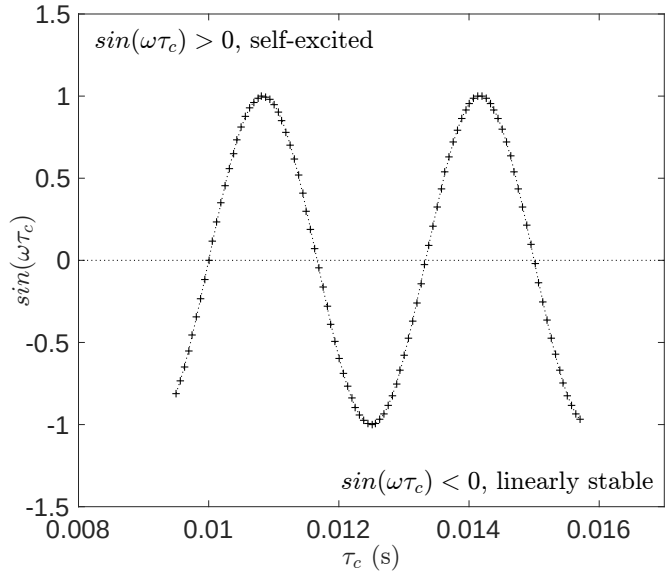

Fig. 7.12 The stability regions of an open-ended Rijke tube as a function of τ_c (McManus et al., 1993).

7.6.2 Sensitivity of frequencies during periods of linear decay to changes in convective time delay

The frequencies observed during periods of linear growth and decay, σ_i, were measured experimentally for the operating conditions outlined in appendix C. Similarly to §7.6.1, each operating point corresponded to a different L_f and τ_c. At each of the operating points, 40 frequency data points were measured using the methods outlined in §7.3.2 so that a detailed uncertainty analysis could be performed to minimise random error (see appendix B). Operating points 1 to 5, 10 to 13, and 18 to 20 were obtained in the linearly stable regime via the pulsed forcing method. Operating points 6 to 9 and 14 to 17 were obtained in the self-excited regime with the use of feedback control.

Figure 7.13a shows the frequencies observed during periods of linear growth and decay for the entire range of operating points. Once this data was acquired, the mean, $\bar{\sigma_i}$, was obtained and plotted against the corresponding τ_c (figure

7.13b). It can be seen in figure 7.13b that as τ_c was increased, $\bar{\sigma}_i$ exhibited a cyclic trend with $\bar{\sigma}_i$ values between 306 and 310 Hz.

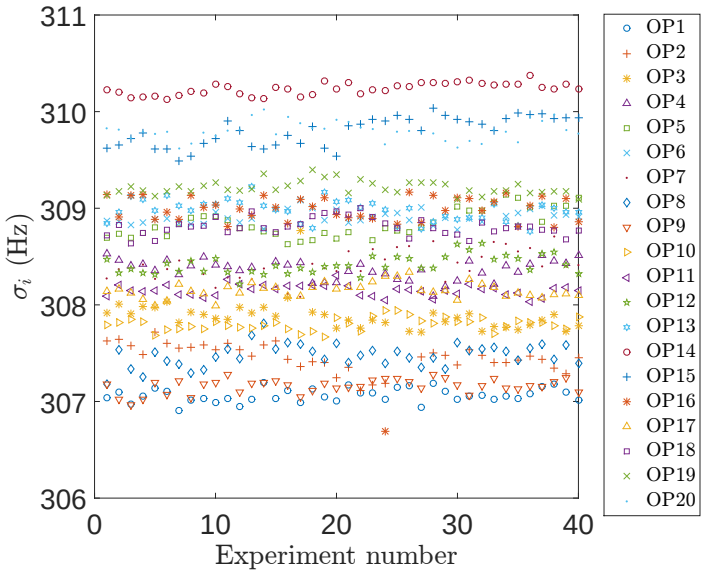

(a)

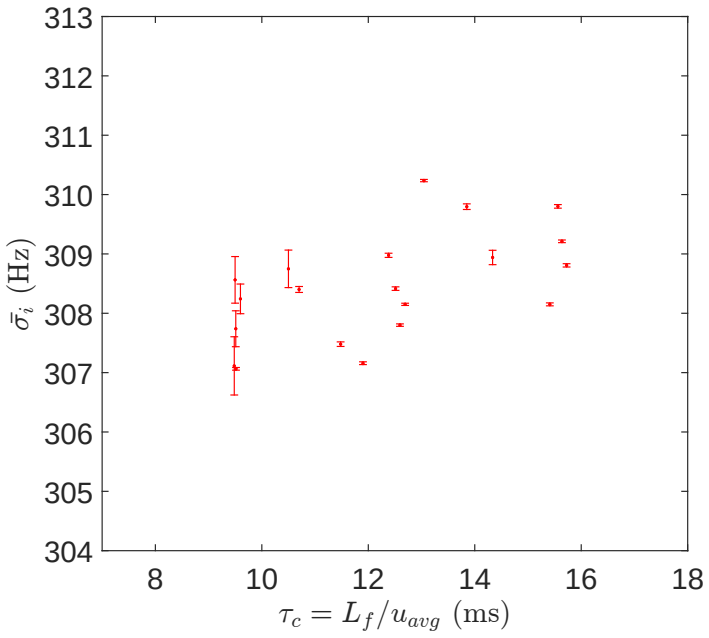

(b)

Fig. 7.13 (a) Oscillation frequency observed during periods of linear growth and decay obtained for different operating points. (b) Oscillation frequency observed during periods of linear growth and decay as a function of τ_c.

7.6.3 Sensitivity of flame length to changes in fuel composition

In this section L_f was measured experimentally for $\phi = 1.25$ and $\phi = 1.35$ over a range of fuel compositions. The same process as outlined in §7.4.3 was used to determine L_f based on Cantera results and provide a comparison for the experimental results.

Figure 7.14 shows the results of the investigation into how sensitive L_f was to changes in fuel composition. Two cases were studied: (i) $\phi = 1.25$ and (ii) $\phi = 1.35$. For both cases, ϕ was calculated via the same method as described in §7.4.3. The ethylene component of the fuel mixture was varied from 20 to 70 % for $\phi = 1.35$ and from 20 to 50 % for $\phi = 1.25$. The reason that the percentage of ethylene was not increased past 70 % for $\phi = 1.35$ and 50 % for $\phi = 1.25$ was because at these conditions flash-back occurred.

It can be seen in figure 7.14 that for both cases examined, L_f slowly decreases with an increasing percentage of ethylene in the mixture. This is expected as by increasing the amount of ethylene in the fuel mixture, S_l is also increased (figure 7.6). With an increased S_l there becomes a new point of equilibrium between u_b and S_l, resulting in a shorter L_f. This can be explained mathematically via the following equation (Seitzman and Wilde, 2014):

$$S_l = \frac{\dot{m}_{exit}}{\rho_u A_{flame}} \tag{7.7}$$

where $\dot{m}_{exit}$ is the mass flow rate through the exit of the burner tube, ρ_u is the density of the unburnt reactants, and A_{flame} is the flame area, which is directly proportional to L_f. It can be seen in equation (7.7) that as S_l increases, A_{flame} and thus L_f will decrease.

In comparing the experimental results for both cases to the results determined empirically from Cantera, it is clear that the agreement between the two is good. This comparison serves as a useful addition of evidence that the Cantera code described in §7.4 is reliable for the purposes of this work.

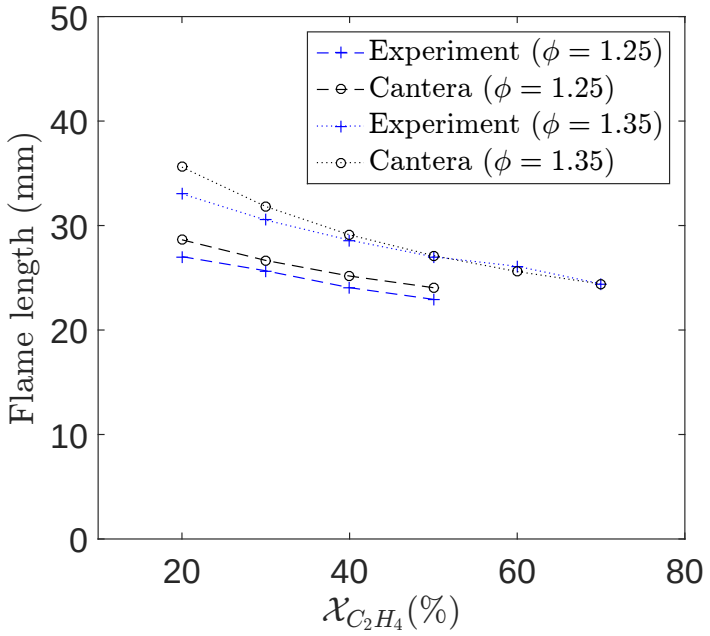

Fig. 7.14 L_f as a function of the percentage of ethylene in the fuel mixture. Cantera results are compared with experimental results to validate the S_l calculation code.

7.7 Concluding remarks

This chapter has demonstrated that the techniques developed in chapters 3, 4, 5, and 5 can be applied to a real combustion system. These techniques were used and taken a step further to investigate the sensitivity of linear growth and decay rates and frequencies observed during periods of linear growth and decay are to changes in τ_c. How this work ties in with the ongoing research by the group will be discussed in chapter 8.2.

Chapter 8

Conclusions

Thermoacoustic instability remains a significant problem faced in the design and development of many combustion systems. The primary aim of designers is to design linearly stable thermoacoustic systems in which these dangerous oscillations do not arise. In thermoacoustics, adjoint-based sensitivity analysis has shown promise at predicting the parameters which have the most influence on the linear growth and decay rates and oscillation frequency of a system. Therefore, adjoint-based methods could prove to be a valuable tool for developing optimal passive control solutions (Magri and Juniper, 2013c). In this thesis, reliable and automated experimental techniques have been developed to perform experimental sensitivity analysis of the linear growth and decay rates and oscillation frequency observed during periods of growth and decay. A first experimental comparison with adjoint-based methods in thermoacoustics is performed which highlights areas of good agreement as well as providing direction for the further development of adjoint-based sensitivity analysis in thermoacoustic systems.

8.1 Summary of main findings

The objective of chapter 3 was to investigate the effect of a passive drag device on the shift in linear growth rate and oscillation frequency observed during periods of linear growth. A novel, automated experimental procedure was used to obtain the data and then experimental results were compared to the theoretical predictions of adjoint-based sensitivity analysis (Magri and Juniper, 2013c). The shift in linear growth rate agreed qualitatively well with theoretical predictions, however, the oscillation frequency did not agree. This was because the highly simplified physical model used by Magri and Juniper (2013c) and discussed in chapter 2 did not account for mean flow changes in the system. Specifically, the temperature changes that occur due to the introduction of a passive drag device were not accounted for.

In chapter 4, a secondary heat source was used as a control device and the shift in linear growth and decay rate and oscillation frequency observed during periods of linear growth and decay was investigated. A novel, automated experimental procedure was used to obtain the data and then experimental results are compared with the theoretical predictions of adjoint-based sensitivity analysis (Magri and Juniper, 2013c). Similarly to chapter 3, the shift in linear growth rate agreed qualitatively well with the theoretical predictions, while the shift in observed frequency was not well predicted. The reason for the discrepancy is mentioned above and discussed in detail in chapter 4. Both chapters 3 and 4 act as the first experimental comparison to adjoint-based sensitivity analysis in thermoacoustics.

The tools developed in chapters 3 and 4 are improved upon in chapter 5 and applied to three control devices: (i) a passive drag device, (ii) a secondary heat source, and (iii) a variable area outlet in the form of a mechanical iris located at the downstream end of the tube. Chapter 5 shows the development of a pulsed

forcing techqnique, inspired by Mejia et al. (2016), which is approximately 12 times faster than the methods presented in chapters 3 and 4. By using this technique, we could obtain thousands of data points in a matter of hours. This amount of data collection is unprecedented in thermoacoustics due to the cost and time of experiments. In chapter 5, the shift in linear decay rate and oscillation frequency during periods of linear decay was investigated due to the introduction of the three control devices. Similarly to chapter 3 and 4, the shift in linear growth rate due to the passive drag device and secondary heat source exhibit the same qualitative features when compared with the adjoint-based sensitivity analysis of Magri and Juniper (2013c). The shift in frequency is again a point of discrepancy for the reasons mentioned above and discussed in chapter 5. The shift in growth rate due to the variable area outlet behaves as would be expected and is physically explained in chapter 5.

Chapter 6 investigates the point of zero growth rate predicted by both the pulsed forcing technique and feedback control technique. The experimental techniques are used in the presence of a variable area outlet in the form of a mechanical iris located at the outlet of the tube. It is important to note that the pulsed forcing technique measures linear decay rates and the feedback control technique measures linear growth rates. Neither technique measures both linear growth and decay rates. Therefore, a convenient way to compare them is to extrapolate to the operating points with zero growth rate and check that these points are sufficiently close. The investigation found that both methods predicted very similar regions of zero growth rate which indicated that: (i) either method is suitable for use in thermoacoustic systems, and (ii) that neither method introduces any systematic bias into the experimental results.

The final results chapter of this thesis, chapter 7, presents an experimental sensitivity analysis performed on a flame-driven Rijke tube. The flame used in this set-up was a ducted premixed conical laminar flame with methane and

ethylene as the fuel and air as the oxidiser. There were three achievements of this chapter: (i) it was successfully shown that the experimental techniques developed in the preceding chapters are applicable to a real combustion system; (ii) it provided results showing the sensitivity of linear growth and decay rates and oscillation frequency observed during periods of linear growth and decay to changes in the flames convective time-delay, one of the most sensitive parameters in any thermoacoustic system; and (iii) it also confirms that the flame time delay is the crucial factor and that we can change this quite easily by changing the fuel composition. A detailed section on the main assumptions of this analysis was added to aid in the interpretation and understanding of the results.

8.2 Future work

The future work for this project can be assigned to two categories: (i) short-medium term future work, and (ii) long term future work.

(i) Short-medium term future work

1. The results from the first comparison between experimental sensitivity analysis and adjoint-based sensitivity analysis (chapters 3 and 4) show that it is imperative to further develop the physical model upon which the adjoint-based analysis is performed. The tens of thousands of experimental data will be used to infer the unknown parameters of a physical model of the experiment. This will be applied first on the vertical electrically-driven Rijke tube. One key benefit of this technique is that if an accurate model of the system can be obtained with experimental data points for a few parameters, it could be possible to use similar techniques to model larger combustion systems where it is difficult to make experimental measurements close to the point of combustion.

2. Once the underlying model is updated and a better comparison between theoretical and experimental sensitivity analysis is achieved, particularly for the oscillation frequency, it would be interesting to perform real-time tuned passive control of thermoacoustic oscillations. By combining both the automated experimental methods, presented in this thesis, and adjoint-based sensitivity analysis one could update the physical parameters of the adjoint-based model with the real-time experimental measurements and then use this model to predict the changes that will stabilize the experimental system. A good starting point would be to set up the variable area outlet (discussed in chapters 5 and 6) on the vertical electrically-driven Rijke tube and see whether the systems growth rate could be minimised (or maximised) in real time by changing the iris diameter based on measured parameters.

3. These techniques could then be extended to a real combustion system, a ducted premixed conical laminar flame (chapter 7). A model based on a simple $n - \tau$ model, where n is the gain of the system and τ is the convective time delay, is being developed by the group. The objective is to use experimental measurements of linear growth and decay rates to infer the parameters of n and τ. This is particularly useful as thermoacoustic systems are typically very sensitive to small changes in τ (Juniper and Sujith, 2018). If parameters for τ can be inferred from experimental data, then accurate and readily up-datable models can be developed of the thermoacoustic system.

4. Other short-medium term work could focus on developing adjoint-based models for the variable area outlet so as to try and predict the behaviour observed in chapter 5. This could serve as yet another comparison for

adjoint-based methods in thermoacoustic, further demonstrating their suitability.

(ii) Long term future work

1. Following on from the future work discussed in the "short-medium term future work", both these new modelling techniques and the experimental sensitivity analysis techniques contained in this thesis can be scaled up and their applicability to larger combustion systems investigated. For example we could apply it to Rama Balachandran's experimental rig (Balachandran, 2005).

2. The eventual goal would be to apply an updated version of the experimental sensitivity analysis techniques developed in this thesis in parallel with the group's improved modelling capabilities to perform both experimental sensitivity analysis and adjoint-based sensitivity analysis on the Cambridge University Annular Combustor Rig. This rig is representative of a gas turbine engine and favourable results would show real promise for the application of adjoint-based sensitivity analysis to industrial combustion systems. The experimental rigs utilised throughout this thesis are bench-top level experiments with low-noise, and therefore, the methods of experimental sensitivity analysis presented in this thesis would have to be revised. Although one could not place a loudspeaker at the outlet of the annular rig, one could perhaps use other forms of excitation such as pulsing the fuel lines to generate equivalence ratio fluctuations.

References

Aguilar, J. G., Magri, L., and Juniper, M. P. (2017). Adjoint-based sensitivity analysis of low-order thermoacoustic networks using a wave-based approach. *Journal of Computational Physics*, 341:163 – 181.

Annaswamy, A. M., Fleifil, M., Rumsey, J. W., Prasanth, R., Hathout, J. P., and Ghoniem, A. F. (2000). Thermoacoustic instability: model-based optimal control designs and experimental validation. *IEEE Transactions on Control Systems Technology*, 8(6):905–918.

Annaswamy, A. M. and Ghoniem, A. F. (2002). Active control of combustion instability: theory and practice. *Control Systems, IEEE*, 22:37–54.

Balachandran, R. (2005). *Experimental investigation of the response of turbulent premixed flames to acoustic oscillations*. PhD Thesis, University of Cambridge.

Balasubramanian, K. and Sujith, R. I. (2008). Thermoacoustic instability in a Rijke tube: Non-normality and nonlinearity. *Physics of Fluids*, 20(4):044103.

Basok, B. I. and Gotsulenko, V. V. (2014). Self-oscillations in a Rijke tube with receiver positioning at its entrance. *Thermophysics and Aeromechanics*, 21(4):469–478.

Bayly, B. J. (1985). Onset and equilibration of oscillations in general Rijke devices. *Journal of the Acoustical Society of America*, 79(3):846–851.

Bellucci, V., Flohr, P., Paschereit, C. O., and Magni, F. (2004). On the use of Helmholtz resonators for damping acoustic pulsations in industrial gas turbines. *Journal of Engineering for Gas Turbines and Power*, 126:271–275.

Bittanti, S., De Marco, A., Poncia, G., and Prandoni, W. (2002). Identification of a model for thermoacoustic instabilities in a Rijke tube. *IEEE Transactions on Control Systems Technology*, 10(4):490–502.

Blonbou, R. and Laverdant, A. (2000). Active control of combustion instabilities on a Rijke tube using neural networks. *Proceedings of the Combustion Institute*, 28:747–755.

Bottaro, A., Corbett, P., and Luchini, P. (2003). The effect of base flow variation on flow stability. *Journal of Fluid Mechanics*, 476:293–302.

Candel, S. M. (1992). Combustion instabilities coupled by pressure waves and their active control. *Symposium (International) on Combustion*, 24:1277–1296.

Candel, S. M. (2002). Combustion dynamics and control: Progress and challenges. *Proceedings of the Combustion Institute*, 29:1–28.

Carrier, G. F. (1954). The mechanics of the Rijke tube. *Quarterly Applied Mathematics*, 12:383–395.

Carvalho, J. A., Ferreira, M. A., Bressan, C., and Ferreira, J. L. G. (1989). Definition of heater location to drive maximum amplitude acoustic oscillations in a Rijke tube. *Combustion and Flame*, 76(1):17–27.

Chomaz, J. M. (1993). Linear and non-linear, local and global stability analysis of open flows. In *Turbulence in spatially extended systems*, pages 245–257.

Chomaz, J. M. (2005). Global instabilities in spatially developing flows: Non-normality and nonlinearity. *Annual Review of Fluid Mechanics*, 37(1):357–392.

Chu, B. (1965). On the energy transfer to small disturbances in fluid flow (Part I). *Acta Mechanica*, 1(Part I):215–234.

Collyer, A. A. and Ayres, D. J. (1972). The generation of sound in a Rijke tube using two heating coils. *Journal of Physics D: Applied Physics*, 5:73–75.

Correa, S. M. (1998). Power generation and aeropropulsion gas turbines: From combustion science to combustion technology. In *27th Symposium (International) on Combustion*, volume 27, pages 1793–1807. The Combustion Institute.

Crocco, L. and Cheng, S. (1956). Theory of combustion instability in liquid propellant rocket motors. Technical report, Technical Report No. 0429886, Princeton University,.

Crocco, L., Mitchell, C. E., and Sirignano, W. A. (1969). Nonlinear longitudinal instability in rocket motors with concentrated combustion. *Combustion Science and Technology*, 1:33–64.

Culick, F. E. C. (1988). Combustion instabilities in liquid-fueled propulsion systems - An overview. *AGARD Conference on Combustion Instabilities in Liquid-Fueled Propulsion Systems*, 450:1–74.

Culick, F. E. C. (2006). *Unsteady motions in combustion chambers for propulsion systems*, volume 323. North Atlantic Treaty Organisation (NATO).

Dowling, A. P. (1995). The calculation of thermoacoustic oscillations. *Journal of Sound and Vibration*, 180:557–581.

Dowling, A. P. and Morgans, A. S. (2005). Feedback control of combustion Ooscillations. *Annual Review of Fluid Mechanics*, 37(1):151–182.

Egolfopoulos, F. N., Zhu, D. L., and Law, C. K. (1990). Experimental and numerical determination of laminar flame speeds: mixtures of C2-hydrocarbons with oxygen and nitrogen. *Proceedings of the Combustion Institute*, pages 471–478.

Eldredge, J. D. and Dowling, A. P. (2003). The absorption of axial acoustic waves by a perforated liner with bias flow. *Journal of Fluid Mechanics*, 485:307–335.

Feldman, K. T. (1968). Review of the literature on Rijke thermoacoustic phenomena. *Journal of Sound and Vibration*, 7(1):83–89.

Giannetti, F., Camarri, S., and Luchini, P. (2010). Structural sensitivity of the secondary instability in the wake of a circular cylinder. *Journal of Fluid Mechanics*, 651:319.

Giannetti, F. and Luchini, P. (2007). Structural sensitivity of the first instability of the cylinder wake. *Journal of Fluid Mechanics*, 581:167–197.

Goodwin, D. G., Moffat, H. K., and Speth, R. L. (2017). Cantera: An object-oriented software toolkit for chemical kinetics, thermodynamics, and transport processes. Available at http://www.cantera.org, Version 2.3.0.

Gopalakrishnan, E. A. and Sujith, R. I. (2014). Influence of system parameters on the hysteresis characteristics of a horizontal Rijke tube. *International Journal of Spray and Combustion Dynamics*, 6(3):293–316.

Gysling, D. L., Copeland, G. S., McCormick, D. C., and Proscia, W. M. (2000). Combustion system damping augmentation with Helmholtz resonators. *Journal of Engineering for Gas Turbines and Power*, 122:269–274.

Hantschk, C. C. and Vortmeyer, D. (1999). Numerical simulation of self-excited thermoacoustic instabilities in a Rijke tube. *Journal of Sound and Vibration*, 277(3):511–522.

Harrje, D. T. and Reardon, F. H. (1972). Liquid propellant rocket combustion instability. Technical report, NASA.

Hassan, M. I., Aung, K. T., Kwon, O. C., and Faeth, G. M. (1998). Properties of laminar premixed hydrocarbon/air flames at various pressures. *Journal of Propulsion and Power*, 14(4):479–488.

Heckl, M. A. (1988). Active control of the noise from a rijke tube. *Journal of Sound and Vibration*, 124(1):117–133.

Higgins, B. (1802). On the sound produced by a current of hydrogen gas passing through a tube. *Journal of Natural Philosophy, Chemistry and the Arts*, pages 1:129–131.

Hill, D. C. (1992). A theoretical approach for analyzing the restabilization of wakes. Technical report, NASA Ames Research Center.

Hill, D. C. (1995). Adjoint systems and their role in the receptivity problem for boundary layers. *Journal of Fluid Mechanics*, 292:183–204.

Huerre, P. and Monkewitz, P. A. (1990). Local and global instabilities in spatially developing flows. *Annual Review of Fluid Mechanics*, 22:473–537.

Hummel, T., Berger, F., Stadlmair, N., Schuermans, B., and Sattelmayer, T. (2017). Extraction of linear growth and damping rates of high-frequency thermoacoustic oscillations from time domain data. In *Proceedings of the ASME Turbo Expo 2017*, pages 1–13, Charlotte, NC, USA. American Society of Mechanical Engineers.

Jamieson, N. P. and Juniper, M. P. (2017a). Experimental sensitivity analysis and the equivalence of pulsed forcing and feedback control in thermoacoustic systems. In *Proceedings of the ASME Turbo Expo 2017*, pages 1–11, Charlotte, NC, USA. American Society of Mechanical Engineers.

Jamieson, N. P. and Juniper, M. P. (2017b). Experimental sensitivity analysis of a linearly stable thermoacoustic system via a pulsed forcing technique. *Experiments in Fluids*, 58(123):1–18.

Jamieson, N. P., Rigas, G., and Juniper, M. P. (2016). Experimental sensitivity analysis via a secondary heat source in an oscillating thermoacoustic system. *International Journal of Spray and Combustion Dynamics*, Special Edition:1–10.

Jomaas, G., Zheng, X. L., Zhu, D. L., and Law, C. K. (2005). Experimental determination of counterflow ignition temperatures and laminar flame speeds of C2-C4 hydrocarbons at atmospheric and elevated pressures. *Proceedings of the Combustion Institute*, 30:193–200.

Juniper, M. P. (2011a). Transient growth and triggering in the horizontal Rijke tube. *International Journal of Spray and Combustion Dynamics*, 3(3):209–223.

Juniper, M. P. (2011b). Triggering in the horizontal Rijke tube: non-normality, transient growth and bypass transition. *Journal of Fluid Mechanics*, 667:272–308.

Juniper, M. P. (2012). Triggering in thermoacoustics. *International Journal of Spray and Combustion Dynamics*, 4(3):217–238.

Juniper, M. P. and Magri, L. (2014). Application of receptivity and sensitivity analysis to thermoacoustic instability. In *Von Karman Institute of Fluid Dynamics*, pages 1–25.

Juniper, M. P., Magri, L., Bauerheim, M., and Nicoud, F. (2014). Sensitivity analysis of thermo-acoustic eigenproblems with adjoint methods. In *Center for Turbulence Research, Proceedings of the Summer Program*, pages 1–10.

Juniper, M. P. and Sujith, R. I. (2018). Sensitivity and nonlinearty of thermoacoustic oscillations. *Annual Reviews of Fluid Mechanics*, 50:661–689.

Juniper, M. P. and Waugh, I. (2010). Bypass transition to sustained thermoacoustic oscillations in a linearly stable Rijke tube. *16th AIAA/CEAS Aeroacoustics Conference*, pages 1–10.

Kashinath, K. (2013). *Nonlinear Thermoacoustic Oscillations of a Ducted Laminar Premixed Flame*. Phd thesis, University of Cambridge.

Katto, Y. and Sajiki, A. (1977). Onset of oscillation of a gas-column in a tube due to the existence of heat conduction field. *Bulletin of the JSME*, 20:1161–1168.

Kendrick, D. W., Anderson, T. J., Sowa, W., and Snyder, T. S. (1999). Acoustic sensitivities of lean-premixed fuel injectors in a single nozzle rig. *Journal of Engineering for Gas Turbines and Power*, 121:429–436.

Kwon, Y. and Lee, B. (1985). Stability of the Rijke thermoacoustic oscillation. *Journal of the Acoustical Society of America*, 78(4):1414–1420.

Langhorne, P. J. (1988). Reheat buzz: An acoustically coupled combustion instability. Part 1. Experiment. *Journal of Fluid Mechanics*, 193:417–443.

Lefebvre, A. H. (1980). Airblast atomization. *Progress in Energy and Combustion Science*, 6:233–261.

Li, S., Zhao, D., Ji, C., and Li, J. (2014). Combustion instabilities in a bifurcating tube: Open- and closed-loop measurements. *AIAA Journal*, 52(11):2513–2523.

Lieuwen, T. C. (2012). *Unsteady combustor physics.* Cambridge University Press.

Lieuwen, T. C. and Lu, F. K. (2005). *Combustion instabilities in gas turbine engines: Operational experience, fundamental mechanisms, and modeling.* American Institute of Aeronautics and Astronautics.

Lieuwen, T. C., Torres, H., Johnson, C., and Zinn, B. T. (2001). A mechanism of combustion instability in lean premixed gas turbine combustors. *Transactions of the ASME*, 123:182–189.

Lieuwen, T. C. and Zinn, B. T. (1998). The role of equivalence ratio oscillations in driving combustion instabilities in low NOx gas turbines. *Symposium (International) on Combustion*, 27:1809–1816.

Lighthill, M. J. (1954). The response of laminar skin friction and heat transfer to fluctuations in the stream velocity. *Proceedings of the Royal Society of London. Series A, Mathematical and Physical Sciences*, 224(1156):1–23.

Luchini, P. and Bottaro, A. (2014). Adjoint equations in stability analysis. *Annual Review of Fluid Mechanics*, 46(1):493–517.

Luo, Z., Lu, T., and Liu, J. (2011). A reduced mechanism for ethylene/methane mixtures with excessive NO enrichment. *Combustion and Flame*, 158(7):1245–1254.

Macquisten, M. A. and Dowling, A. P. (1995). Combustion oscillations in a twin-stream afterburner. *Journal of Sound and Vibration*, 188(4):545–560.

Madrame, H. (1983). Thermally induced acoustic oscillations in a pipe. *Bulletin of the JSME*, 26(214):603–610.

Magri, L. and Juniper, M. P. (2013a). A novel theoretical approach to passive control of thermo-acoustic oscillations: Application to Ducted Heat Sources. In *Proceedings of ASME Turbo Expo 2013*, pages 1–11, San Antonio, Texas.

Magri, L. and Juniper, M. P. (2013b). A theoretical approach for passive control of thermoacoustic oscillations: Application to Ducted Flames. *Journal of Engineering for Gas Turbines and Power*, 135(9):1–9.

Magri, L. and Juniper, M. P. (2013c). Sensitivity analysis of a time-delayed thermo-acoustic system via an adjoint-based approach. *Journal of Fluid Mechanics*, 719:183–202.

Magri, L. and Juniper, M. P. (2014a). Adjoint-based linear analysis in reduced-order thermo-acoustic models. *International Journal of Spray and Combustion Dynamics*, 6(3):225–246.

Magri, L. and Juniper, M. P. (2014b). Global modes, receptivity, and sensitivity analysis of diffusion flames coupled with duct acoustics. *Journal of Fluid Mechanics*, 752:237–265.

Maling, G. C. (1963). Simplified analysis of the Rijke phenomenon. *The Journal of the Acoustical Society of America*, pages 1058–1060.

Margolin, A. (1999). Early investigations of instability in Russia. *Journal of Propulsion and Power*, 15(6):922–925.

Mariappan, S. (2011). *Theoretical and Experimental Investigation of the Non-Normal Nature of Thermoacoustic Interactions*. PhD thesis, Indian Institute of Technology, Madras.

Mariappan, S. and Sujith, R. I. (2011). Modelling nonlinear thermoacoustic instability in an electrically heated Rijke tube. *Journal of Fluid Mechanics*, 680:511–533.

Marino, L. and Luchini, P. (2009). Adjoint analysis of the flow over a forward-facing step. *Theoretical and Computational Fluid Dynamics*, 23:37–54.

Marquet, O., Sipp, D., and Jacquin, L. (2008). Sensitivity analysis and passive control of cylinder flow. *Journal of Fluid Mechanics*, 615:221–252.

Matveev, K. (2003). *Thermoacoustic instabilities in the Rijke tube: experiments and modeling*. PhD Thesis, California Institute of Technology.

Matveev, K. I. and Culick, F. E. C. (2003). Limit-cycle properties of a Rijke tube. *Technical Acoustics*, 12:1–13.

McIntosh, C. A. and Rylands, S. (1996). A model of heat transfer in Rijke tube burners. *Combustion Science and Technology*, 113(1):273–289.

McManus, K. R., Poinsot, T., and Candel, S. M. (1993). A review of active control of combustion instabilities. *Progress in Energy and Combustion Science*, 19:1–29.

Mcquay, M. Q., Dubey, R. K., and Carvalho Jr, J. A. (2000). The effect of acoustic mode on time-resolved temperature measurements in a Rijke-tube pulse combustor. *Fuel*, 79:1645–1655.

Mejia, D., Miguel-Brebion, M., and Selle, L. (2016). On the experimental determination of growth and damping rates for combustion instabilities. *Combustion and Flame*, 169:287–296.

Merk, H. J. (1957). Analysis of heat-driven oscillations of gas flows. *Applied Scientific Research, Section A*, 6(5-6):402–420.

Mohammadi, B. and Pironneau, O. (2004). Shape optimization in fluid mechanics. *Annual Review of Fluid Mechanics*, 36:255–279.

Neumeier, Y. and Zinn, B. T. (1996). Experimental demonstration of active control of combustion instabilities using real-time modes observation and secondary fuel injection. *Symposium (International) on Combustion*, 26:2811–2818.

Neuringer, J. L. and Hudson, G. E. (1952). An investigation of sound vibrations in a tube containing a heat source. *The Journal of the Acoustical Society of America*, 24(6):231–234.

Nicoli, C. and Pelcé, P. (1989). One-dimensional model for the Rijke tube. *Journal of Fluid Mechanics*, 202:83–96.

Noble, A. C., King, G. B., Laurendeau, N. M., Gord, J. R., and Roy, S. (2012). Nonlinear thermoacoustic instability dynamics in a Rijke tube. *Combustion Science and Technology*, 184(3):293–322.

Noiray, N., Durox, D., Schuller, T., and Candel, S. M. (2007). Passive control of combustion instabilities involving premixed flames anchored on perforated plates. *Proceedings of the Combustion Institute*, 31 I:1283–1290.

Noiray, N. and Schuermans, B. (2013). Deterministic quantities characterizing noise driven Hopf bifurcations in gas turbine combustors. *International Journal of Nonlinear Mechanics*, 50:152–163.

Oefelein, J. C. and Yang, V. (1993). Comprehensive review of liquid-propellant combustion instabilities in F-l engines. *Journal of Propulsion and Power*, 9(5):657–677.

OMEGA Engineering Inc (Accessed May 2017). Transactions in Measurement and Control: Volume 1, Second Edition, Non-Contact Temperature Measurement. https://www.omega.com/literature/transactions/transactions_Vol_I.pdf.

Pikovsky, A., Rosenblum, M., and Kurths, J. (2003). *Synchronization: A universal concept in nonlinear sciences*. Cambridge Nonlinear Science Series. Cambridge University Press.

Provansal, M., Mathis, C., and Boyer, L. (1987). Bénard-von Kármán instability: transient and forced regimes. *Journal of Fluid Mechanics*, 182:1–22.

Putnam, A. A. and Dennis, W. R. (1954). Burner oscillations of the gauze-tone type. *The Journal of the Acoustical Society of America*, 26(5):716–726.

Raun, R. L. and Beckstead, M. W. (1993). A numerical model for temperature gradient and particle effects on Rijke burner oscillations. *Combustion and Flame*, 94:1–24.

Raun, R. L., Beckstead, M. W., Finlinson, J. C., and Brooks, K. P. (1993). A review of Rijke tubes, Rijke burners and related devices. *Progress in Energy Combustion Sciences*, 19:313–364.

Rayleigh, J. W. S. (1878). The explanation of certain acoustical phenomena. *Nature (London)*, 18:319–321.

Renard, P. H., Thévenin, D., Rolon, J. C., and Candel, S. M. (2000). Dynamics of flame/vortex interactions. *Progress in Energy and Combustion Science*, 26:225–282.

Richards, G. A. and Janus, M. C. (1997). Characterization of oscillations during premix gas turbine combustion. In *International Gas Turbine & Aeroengine Congress & Exhibition*, pages 1–15, Orlando, Florida. ASME.

Richards, G. A., Straub, D. L., and Robey, E. H. (2003). Passive control of combustion dynamics in stationary gas turbines. *Journal of Propulsion and Power*, 19(5):795–810.

Rienstra, S. W. and Hirschberg, A. (2006). An introduction to acoustics.

Rigas, G., Jamieson, N. P., Li, L. K. B., and Juniper, M. P. (2015). Experimental sensitivity analysis and control of thermoacoustic systems. *Journal of Fluid Mechanics*, 787, R1:1–10.

Rijke, P. L. (1859). On the vibration of the air in a tube open at both ends. *Philosophical Magazine*, 17:419–422.

Saito, T. (1965). Vibrations of air-columns excited by heat supply. *The Japan Society of Mechanical Engineers*, 8(32).

Sattinger, S. S., Neumeier, Y., Nabi, A., Zinn, B. T., Amos, D. J., and Darling, D. D. (2000). Sub-scale demonstration of the active feedback control of gas-turbine combustion Instabilities. *Journal of Engineering for Gas Turbines and Power*, 122(April 2000):262.

Sayadi, T., Le Chenadec, V., Schmid, P. J., Richecoeur, F., and Massot, M. (2014). Thermoacoustic instability – a dynamical system and time domain analysis. *Journal of Fluid Mechanics*, 753:448–471.

Schadow, K. C. and Gutmark, E. (1992). Combustion instability related to vortex shedding in dump combustors and their passive control. *Progress in Energy and Combustion Science*, 18:117–132.

Schmid, P. J. and Brandt, L. (2014). Analysis of fluid systems: Stability, receptivity, sensitivity. *Applied Mechanics Reviews*, 66(2):1–21.

Schumm, M., Berger, E., and Monkewitz, P. A. (1994). Self-excited oscillations in the wake of two-dimensional bluff bodies and their control. *Journal of Fluid Mechanics*, 271:17–53.

Seitzman, J. M. and Wilde, B. (2014). Lecture notes on premixed flames: Flame stretch and flame speed measurements (AE/ME 6766 Combustion).

Semlitsch, B., Orchini, A., Dowling, A., and Juniper, M. (2017). G-equation modelling of thermoacoustic oscillations of partially premixed flames. *International Journal of Spray and Combustion Dynamics*, 9(4):260–276.

Sipp, D., Marquet, O., Meliga, P., and Barbagallo, A. (2010). Dynamics and control of global instabilities in open-flows: A linearized approach. *Applied Mechanics Reviews*, 63:030801.

Smith, G. P., Golden, D. M., Frenklach, M., Moriarty, N. W., Eiteneer, B., Goldenberg, M., Bowman, C. T., Hanson, R. K., Song, S., Gardiner, W. C., Jr., V. V. L., and Qin, Z. (2017). GRI Mech 3.0. http://www.me.berkeley.edu/gri_mech/.

Sreenivasan, K. R., Raghu, S., and Chu, B. (1985). The control of pressure oscillations in combustion and fluid dynamical systems. In *1985 AIAA Shear Flow Control Conference*, pages 1–10, Boulder, Colorado. American Institute of Aeronautics and Astronautics.

Stadlmair, N. V., Hummel, T., and Sattelmayer, T. (2017). Thermoacoustic damping rate determination from combustion noise using bayesian statistics. In *Proceedings of the ASME Turbo Expo 2017*, pages 1–11, Charlotte, NC, USA. American Society of Mechanical Engineers.

Steele, R. C., Cowell, L. H., Cannon, S. M., and Smith, C. E. (2000). Passive control of combustion instability in lean premixed combustors. *Journal of Engineering for Gas Turbines and Power*, 122:412.

Strogatz, S. H. (1994). *Nonlinear dynamics and chaos: With applications to physics, biology, chemistry, and Engineering.* Perseus Books Publishing, LLC.

Strykowski, P. J. and Sreenivasan, K. R. (1990). On the formation and suppression of vortex 'shedding' at low Reynolds numbers. *Journal of Fluid Mechanics*, 218:71–107.

Subramanian, P., Mariappan, S., Sujith, R. I., and Wahi, P. (2010). Bifurcation analysis of thermoacoustic instability in a horizontal Rijke tube. *International Journal of Spray and Combustion Dynamics*, 2(4):325–355.

Subramanian, P., Sujith, R. I., and Wahi, P. (2013). Subcritical bifurcation and bistability in thermoacoustic systems. *Journal of Fluid Mechanics*, 715:210–238.

Taylor, J. R. (1997). *An introduction to error analysis: The study of uncertainties in physical measurements (Second Edition).* University Science Books, Sausalito, California, USA.

Turns, S. (2012). *An introduction to combustion: concepts and applications.* Asia Higher Education Engineering/Computer Science Mechanical Engineering. McGraw-Hill, 3rd edition.

Vagelopoulos, C. M. and Egolfopoulos, F. N. (1998). Direct experimental determination of laminar flame speeds. *Proceedings of the Combustion Institute*, 27:513–519.

Vagelopoulos, C. M., Egolfopoulos, F. N., and Law, C. K. (1994). Further considerations on the determination of laminar flame speeds with the counterflow twin-flame technique. *Proceedings of the Combustion Institute*, 25(1):1341–1347.

Wang, H., You, X., Joshi, A. V., Davis, S. G., A. Laskin, F. E., and Law, C. K. (2007). USC Mech Version ii. High-Temperature Combustion Reaction Model of H2/CO/C1-C4 Compounds. http://ignis.usc.edu/USC_Mech_II.htm.

Weng, F., Zhu, M., and Jing, L. (2014). Beat: a nonlinear thermoacoustic instability in Rijke burners. *International Journal of Spray and Combustion Dynamics*, 6(3):247–266.

Yoon, H., Peddieson Jr, J., and Purdy, K. R. (1998). Mathematical modeling of a generalized Rijke tube. *International Journal of Engineering Science*, 36:1235–1264.

Yoon, H., Peddieson Jr, J., and Purdy, K. R. (2001). Non-linear response of a generalized Rijke tube. *International Journal of Engineering Science*, 39(15):1707–1723.

Zhang, Z., Zhao, D., Han, N., Wang, S., and Li, J. (2015). Control of combustion instability with a tunable Helmholtz resonator. *Aerospace Science and Technology*, 41:55–62.

Zhao, D. (2012). Transient growth of flow disturbances in triggering a Rijke tube combustion instability. *Combustion and Flame*, 159(6):2126–2137.

Zhao, D., Ji, C., Li, X., and Li, S. (2015). Mitigation of premixed flame-sustained thermoacoustic oscillations using an electrical heater. *International Journal of Heat Mass Transfer*, 86:309–318.

Appendix A

Images of primary heater and passive control devices

Figure A.1c shows a CAD drawing of the MACOR ceramic disks used in the heat source and passive drag device. The wire used to construct the primary heater, passive drag device and secondary heat source was 80-20 Nickel Chrome Alloy. The wire had a thickness of 0.559 mm, an estimated flow facing length of 670 mm per disk, and theoretical emissivity of 0.87-0.89 (OMEGA Engineering Inc, 2017).

(a)

(b)

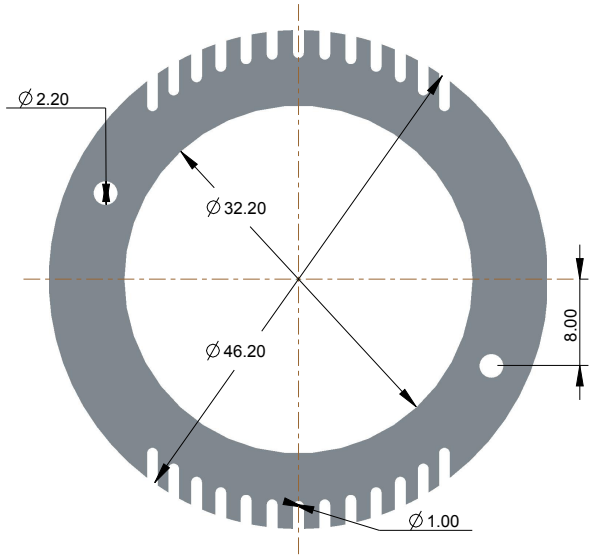

(c)

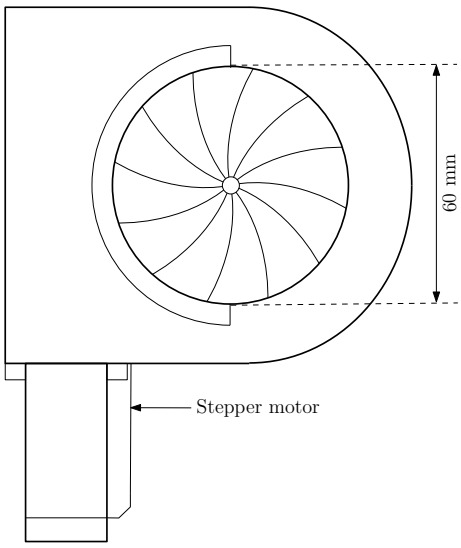

(d)

Fig. A.1 (a) Primary heater. (b) Passive drag device and secondary heat source. (c) Top disk of (a) and (b). (d) Diagram of the variable cross-sectional area outlet (mechanical iris).

Appendix B

Uncertainty Analysis

B.1 Uncertainties in $\delta\sigma$ measurement

This section presents the method used to determine the uncertainty in the experimental data presented in chapter 4, 5, and 7. The methodology used is based on Taylor (1997). We first calculate the sample standard deviation of each data point using:

$$\hat{\epsilon}_\sigma = \sqrt{\left(\frac{1}{N-1}\right)\sum_{ii=1}^{N}(\sigma_{ii} - \bar{\sigma})^2} \tag{B.1}$$

where N is the number of points obtained, σ_{ii} is the measured growth rate, decay rate, frequency during linear growth, or frequency during linear decay, and $\bar{\sigma}$ is the mean value of σ for a specific secondary heater power, P_2 (W), and a specific axial location, x_c/L, averaged over the five experimental repetitions. The standard error was then calculated as:

$$\hat{\epsilon}_{error} = \frac{\hat{\epsilon}_\sigma}{\sqrt{N}} \tag{B.2}$$

The uncertainty is presented as $2\hat{\epsilon}_{error}$ to allow for a 95% confidence interval. The error bars are plotted against the mean P_2 (W) and the mean σ.

B.2 Uncertainties in $\delta\sigma/\delta P_2$ measurement

This section presents the method used to determine the uncertainty in the experimental data presented in chapter 4 and 5. The methodology used is based on Taylor (1997). We calculate the uncertainty of the fitting of the $\delta\sigma$ data so that we can determine the uncertainty in the shift in growth and decay rates and the frequency shift during the growth and decay of oscillation. The fitting of the $\delta\sigma$ data is not forced to go through the origin, thus the line being fitted is of the form $\delta\sigma = BP_2 + A$. We first calculate the uncertainty in the measurements of

y:

$$\varepsilon_y = \sqrt{\left(\frac{1}{N-2}\right)\sum_{j=1}^{N}[\delta\sigma_j - A - BP_{2,j}]^2}, \tag{B.3}$$

where N is the number of points obtained, $\delta\sigma_j$ is the measured growth rate, decay rate, frequency during linear growth, or frequency during linear decay, A and B are constants obtained from the least-squares regression fitting for each axial location, x_c/L, and $P_{2,j}$ are the secondary heater powers examined. The least-squares regression fitting is between the first σ point and the final σ point which corresponds to a secondary heater power less than 50 W, i.e. $P_2 < 50$W. The above result is then used to determine the uncertainty in the measurement of the sensitivity, $\delta\sigma/\delta P_2$. This is calculated using:

$$\varepsilon_B = \varepsilon_y\sqrt{\frac{N}{\triangle}} \tag{B.4}$$

where

$$\triangle = N\sum_{j=1}^{N}[P_{2,j}]^2 - \left(\sum_{j=1}^{N}[P_{2,j}]\right)^2 \tag{B.5}$$

We are only interested in the uncertainty in the constant B. This is the gradient of the least-squares regression fitting. The uncertainty was presented with a 95% confidence interval, i.e. the uncertainty was presented as $2\varepsilon_B$ (Taylor, 1997).

Appendix C

Operating Points for Chapter 7

Table C.1 Operating points used in Chapter 7

Operating Point (OP)	CH_4 **(Ln/min)**	C_2H_4 **(Ln/min)**	**Air (Ln/min)**	L_f **(mm)**	u_0 **(m/s)**	ϕ	S_l **(cm/s)**	T_{unb} **(°C)**	P_{unb} **(mm Hg)**	Percentage (by volume) of CH_4 and C_2H_4	Linearly Stable (LS) or Self-Excited (SE)
1	0.42	0.42	7.30	24.5212	1.2886	1.3705	37.16	22.5	765.75	50 % CH_4, 50 % C_2H_4	LS
2	0.43	0.43	7.44	24.9514	1.3157	1.3767	36.59	22.9	765.75	50 % CH_4, 50 % C_2H_4	LS
3	0.44	0.44	7.58	25.5262	1.3420	1.3827	36.05	23.1	765.75	50 % CH_4, 50 % C_2H_4	LS
4	0.45	0.45	7.73	26.3046	1.3703	1.3867	35.69	23.4	765.75	50 % CH_4, 50 % C_2H_4	LS
5	0.46	0.46	7.90	26.6223	1.4015	1.3870	35.66	23.6	765.75	50 % CH_4, 50 % C_2H_4	LS
6	0.46	0.46	7.89	29.1764	1.3877	1.4040	34.14	22.9	762.75	50 % CH_4, 50 % C_2H_4	SE
7	0.46	0.46	7.70	29.46	1.374	1.422	32.58	23.4	762.75	50 % CH_4, 50 % C_2H_4	SE
8	0.46	0.46	7.60	31.1864	1.358	1.441	30.95	23.4	762.75	50 % CH_4, 50 % C_2H_4	SE
9	0.46	0.46	7.50	31.98	1.343	1.46	29.31	22.9	762.75	50 % CH_4, 50 % C_2H_4	SE
10	0.47	0.47	7.58	34.1018	1.3538	1.4770	27.84	23.6	765.75	50 % CH_4, 50 % C_2H_4	LS
11	0.48	0.48	7.73	35.0301	1.3808	1.4791	27.66	23.6	765.75	50 % CH_4, 50 % C_2H_4	LS
12	0.49	0.49	7.90	35.3310	1.4119	1.4774	27.81	23.8	765.75	50 % CH_4, 50 % C_2H_4	LS
13	0.50	0.50	8.05	35.6449	1.4395	1.4795	27.6271	23.9	765.75	50 % CH_4, 50 % C_2H_4	LS
14	0.50	0.50	7.95	37.35	1.432	1.4975	26.08	24.4	762.75	50 % CH_4, 50 % C_2H_4	SE
15	0.50	0.50	7.90	39.41	1.4213	1.5069	25.49	23.9	762.75	50 % CH_4, 50 % C_2H_4	SE
16	0.50	0.50	7.80	40.31	1.406	1.526	24.48	24.1	762.75	50 % CH_4, 50 % C_2H_4	SE
17	0.50	0.50	7.70	42.38	1.375	1.566	22.36	24.3	762.75	50 % CH_4, 50 % C_2H_4	SE
18	0.51	0.51	7.76	43.9204	1.3965	1.5655	22.38	23.9	765.75	50 % CH_4, 50 % C_2H_4	LS
19	0.52	0.52	7.91	44.5358	1.4240	1.5659	22.36	24.0	765.75	50 % CH_4, 50 % C_2H_4	LS
20	0.53	0.53	8.06	45.1780	1.4516	1.5663	22.34	24.1	765.75	50 % CH_4, 50 % C_2H_4	LS